FABRICATION OF CORE-SHELL BIO-NANOCOMPOSITES VIA BIOMIMETIC MINERALIZATION OF METAL ORGANIC FRAMEWORKS

by

Shaobo Li

APPROVED BY SUPERVISORY COMMITTEE:

_____

Jeremiah J. Gassensmith, Chair

_____

John P. Ferraris

_____

Ronald A. Smaldone

_____

Ray H. Baughman

To mom, dad, granny and grandpa.

FABRICATION OF CORE-SHELL BIO-NANOCOMPOSITES VIA BIOMIMETIC MINERALIZATION OF METAL ORGANIC FRAMEWORKS

by

SHAOBO LI, BS

DISSERTATION

Presented to the Faculty of

The University of Texas at Dallas

in Partial Fulfillment

of the Requirements

for the Degree of

DOCTOR OF PHILOSOPHY IN

CHEMISTRY

THE UNIVERSITY OF TEXAS AT DALLAS

August 2018

ACKNOWLEDGMENTS

I would like to thank my advisor Dr. Jeremiah Gassensmith for recruiting me to join his lab, even though my undergraduate research experiences did not match his research interests. I appreciate that he gave me freedom and encouraged me to conduct research independently. In addition, I feel very grateful for his trust and patience throughout my five years of study. I would like to also thank my graduate research committee members, Dr. John Ferraris, Dr. Ray Baughman and Dr. Ronald Smaldone, for their dedication to educate me for critical thinking and presentation skills to effectively communicate my research work with other scientists.

In addition, I would like to thank my lab members, Dr. Zhuo Chen, Dr. Na Li, Dr. Madushani Dharmarwardana, Anna Schlimme, Raymond Welch, Candace Benjamin, Hamilton Lee, Michael Luzuriaga, Olivia Brohlin and Arezoo Sharivakevishahi, for their great support throughout 5 years of my PhD study.

Special thanks to Dr. Yang Xi, Dr. Tao Zheng, Dr. Long Zhang, Dr. Hetao Chu, Dr. Na Li (from NanoTech), Luhua Wang, Dr. Roger Robins and Dr. Winston Layne for their generous help to teach me lab techniques and data analysis.

Finally, I would like to thank my FCBCD church family, my friends, my parents, grandparents and family for their unconditional love and support.

June 2018

FABRICATION OF CORE-SHELL BIO-NANOCOMPOSITES VIA BIOMIMETIC MINERALIZATION OF METAL ORGANIC FRAMEWORKS

Shaobo Li, PhD
The University of Texas at Dallas, 2018

Supervising Professor: Jeremiah J. Gassensmith

Biomineralization is one of the nature-owned masteries that the organisms have exploited for millions of years to produce organic-inorganic hybrid materials with highly customized compositions, microstructures, morphologies and functionalities. An emerging field called biomimetic mineralization arose from the idea of employing proteinaceous templates to fabricate novel biochemical composites that cannot be produced in nature. Among various biomimetic mineralization strategies, the core-shell fashioned fabrications are of great interest, due to mineralized shells serving as exoskeleton to protect inlaid biological specimens from external stresses. In addition, biomimetically mineralized shells are also functional materials that can be used for sensing, catalysis and drug delivery.

Metal organic frameworks (MOFs) are a family of porous coordination complexes that possess a high surface area and well-defined porosity. The broad variety of composition, synthetic methods, and physicochemical properties make MOFs to be versatile functional materials. This dissertation summarizes exploration of fabricating core-shell fashioned biology@MOF bio-nanocomposites using the tobacco mosaic virus (TMV) and *Escherichia coli* (*E. coli*) as model biological

templates. Zeolitic imidazolate framework-8 (ZIF-8), a widely studied MOF member that is featured in robust chemical and thermal stability, was chosen to compose the biomimetically mineralized shells. This dissertation will demonstrate i) success fabrication of TMV@ZIF-8 and *E. coli*@ZIF-8 core-shell bio-nanocomposites; ii) mechanistic understanding in regard to the impacts of synthetic conditions on morphology, crystallinity and stability of resultant products; iii) impact of synthetic conditions on cell viability.

TABLE OF CONTENTS

LIST OF FIGURES

LIST OF TABLES

CHAPTER 1

INTRODUCTION

1.1 Biomimetic Mineralization

Maybe from the very beginning of human history, we have never stopped learning from other living creatures around us. Not only that, we also benefit from just mimicking our neighbors— we made spears so that we also had sharpened teeth and claws to fight against beasts; we crafted ships so that we can sail on the rivers and seas like fish; we built aircraft so that we can fly freely like birds… Even in the steam-age, electronic-age, and now, we are merely capable of developing more advanced technologies to investigate biology on a micro, nano or molecular scale, yet still have to admire the delicacy and complexity that a living creature can produce, far beyond artificial inventions. With decades of endeavors, now we are able to fabricate materials on nanometer scale, which brings many revolutionary products to our lives; yet high cost, high energy consumption, and harmful wastes are significant drawbacks that limit their application. On the other hand, with just a glimpse of nature we can find infinite examples of biomaterials, ranging from nano to macroscale, that are produced with high accuracy and complexity. More importantly, these fabrication processes are performed under physiological conditions, with almost zero waste. Biomineralization is one of such masteries that organisms have practiced and optimized for millions of years to produce inorganic materials for body construction, protection, and navigation. It describes a mechanism of well-controlled accumulation and construction with metal cations and counter-anions to form amorphous/ crystalline materials on or within the organism. The biomineralized materials possess highly specified compositions, microstructures, morphologies, and functionalities to serve specific needs.[1-2] There are four main types of products generated from

natural biomineralization exercises, such as calcium carbonate, calcium phosphate, silica and iron oxides. Each was synthesized under well–designed strategy and mild conditions for species–specific functionality. For instance, calcium carbonates are well–known biominerals for structural and protective purposes that are produced by water and marine organisms. They can form into skeletons, spine and shells for either building up the overall structure of organisms or shielding the vulnerable soft tissues from attack. Another example is calcium phosphate, which is commonly found in vertebrate bones. The unique mechanical properties of bones are well–defined by the chemical composition and the hierarchical arrangement of functional components. This relies on the mineralization of calcium phosphate aligned harmoniously with collagen fibrils from nanoscale to macroscale.[3]

Undoubtedly, understanding and reapplying the mechanism of biomineralization will essentially enrich the methodologies for smart and efficient self–assembly of inorganic materials through nano to macroscales. One of significant accomplishments is the discovery of specific proteins that are responsible for the biomineralization processes. For example, silicatein was identified to directly catalyzes biomineralization of silica.[4] Later, more proteins have been identified and isolated for the purpose of understanding the biomineralization pathways. Interestingly, inspired by the discovery of biomineralization, an emerging filed called biomimetic mineralization[5-8] arose from the idea of adopting proteinaceous catalysts to fabricate novel biochemical composites that cannot be produced in nature. This novel synthetic strategy allows scientists to fabricate new family of functional composite materials showing great potentials in biomedical engineering. To date, a broad variety of biological templates have been investigated for biomimetic mineralization, ranging from peptides, enzymes, DNAs, viruses and bacteria.[6, 8-9] Despite the peptides and DNAs

that are widely used for modifying the size and shape of 1D and 2D nanoparticles (NPs), viruses, especially tubular and filamentous viruses, seem to be the most favored templates to prepare composite materials due to they possess nature-selected robustness, anisotropic morphology and polarized surfaces for mineralization.[10-12] The as-obtained viral composites usually display NP-grafted proteinaceous scaffolds or core-shell structures, which particle size (or shell thickness) and the particle arrangement can be mediated by the synthetic conditions. However, these studies mostly remain on the exploration of synthetic methodologies. In fact, the as-prepared composite materials have not shown readiness for any practical applications as the stability of biological templates remains the primary concern. Any changes in pH, temperature and solvent contents could result in the denaturation of biological templates unless they are well-encapsulated in the mineral crusts.

In the past few decades, a new family of synthetic micro/mesoporous crystals, which are now commonly known as metal organic frameworks (MOFs), emerged and drastically dominated a broad variety of materials research. Recently, a series of pioneering work in biomimetic mineralization of MOFs has quickly attracted attention from material scientists.

1.2 Metal Organic Frameworks (MOFs)

MOFs represent a family of porous coordination polymers (PCPs) that contain very high surface area and well-developed micro or mesoporous crystalline architectures.[13-14] In general, MOFs are constructed by rigid organic ligand “struts” coordinating with metal “nodes.” With rational selection of components and coordination chemistries, various ligands and metals have been adopted to prepare nearly infinite types of MOFs. Thus, these highly customizable porous

materials have attracted considerable attention from scientists who working in gas storage and separation, catalysis, energy, sensing, and biomedical engineering.[15-24]

One critical challenge of MOFs to fit in current or new generation of technologies is the lack of size and morphological control[25] of the as-synthesized MOFs. Preliminary studies primarily focused on revealing crystalline structures of MOF single crystals, whose size range from micrometers to millimeters have random size distributions. To fully utilize the versatile functionalities of MOFs, preparation strategies that allow precise control over size, shape and uniformity are highly desired. In general, the synthetic strategies of MOF NPs and thin films rely on the presence of metal-binding reagents such as ligands, surfactants, or polymers with chelating functional moieties.[26] These surface-active reagents could either favorably bind to specific crystal facets during crystal growth, or pre-deposite onto substrates or templates to direct the crystal formation.[27-30] Resent study also have shown a lay-by-layer growth of MOFs via self-templating method.[31] More interestingly, metal NPs or metal substrates can serve as sacrificial templates and allow *in situ* converion to MOFs when they were immersed in the ligand precursor solution containing oxidants.[32] In addition, the property of solvent, precursor concentration, molar ratio of ligand and metal precursors, and the counter ainion of the metal salts appear to draw non-negligible impacts to the size and morphology of the MOFs.[33] It worth noting that most of these syntheses are conducted in organic medium and sub-100 nm MOF NPs or thin films with well-defined morphology are always hard to prepare. Biomimetic mineralization could provide a “green” and cost-effective route for nanometer-sized MOFs, though may not be the ultimate solution for the whole MOF family, because many MOF members are ruled out due to their poor water-stability.

Zeolitic imidazolate frameworks (ZIFs) are an important and intensively studied MOF family.[34] They are composed of transition metals (Zn and Co) and imidazoles that could construct typical zeolite topologies with open pore structures (Figure 1.1). Beyond the structural similarities, they also demonstrate robust chemical and thermal stability, which had not been seen in earlier MOF families. One advantage of ZIFs is the ease of syntheses, which can be achieved in aqueous system.

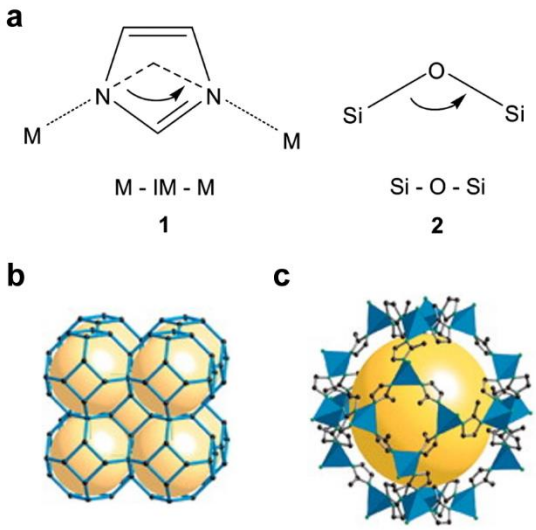

Figure 1.1. a) schematic illustration of imidazolate bridging angle in analog to Si-O-Si angle in zeolites; b) stick diagram of single crystal structure of ZIF-8 and c) structural diagram of a single cage of ZIF-8. Figure reproduced with permission from Ref. 34. Copyright 2006 National Academy of Sciences, U.S.A.

For example, Lai *et al.*[35] reported the fabrication of ZIF-8 NPs with concentrated aqueous precursor solutions. Later, Zhang *et al.*[33] illustrated a instructive summary of ZIF-8 crystalliztion in aqueous system by discussing the impact of counter anions of zinc salt, ligand-to-metal molar ratio, concentration of precursor solution and reaction time to the size, mophology, and crystallinity of the final products. All these studies paved the way for biomimetic mineralization of MOFs. In 2014, Ge *et al.*[36] reported ZIF-8 crystallization in the presence of Cyt enzymes that yielded enzyme@MOF composites. However, it may not be considered as biomemitc

mineralization as they used methanolic precurosrs, which can readily form ZIF-8 crystals spontaneously. Then Falcaro *et al.*[37] illustrated authentic biomimetic mineralization by incubating proteins, enzymes or DNAs in aqueous MOF precursors. They revealed the biological mateirals are well-encapsulated in the polyhedral MOF crystals. The outstanding enzyme@ZIF-8 composite has shown extraordinary thermal and chemical stability that allows the inlaid enzymes to retain their activity in various treatments under denaturing conditions.

1.3 Model Biological Templates

Tobacco Mosaic Virus (TMV)

TMV is the first characterized and most studied virus on the planet. It is a rod-shaped proteinaceous nanoparticle that is 300-nm long and 18-nm wide, with a 4-nm inner longitudinal channel (Figure 1.2).[38] The tubular viral particle is composed of 2130 coat proteins that self-assemble around a single strand of RNA. TMV possesses outstanding stability to a broad range of pH (2 to 10) and temperature (up to 60 °C).[10] The coat protein that composes the viral capsid has three chemically modifiable amino acid handles that spread either on the outer surface or on the inner channel of the tubular viral particle.[39] Specifically, a diazonium coupling reaction can be performed on the solvent-accessable tyrosine (Y139) on the exterior, whilst EDC coupling can address on glutamate residues (E97 and E106) on the interior.[40]

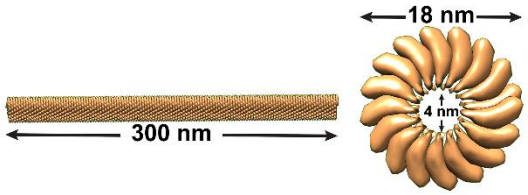

Figure 1.2. Model illustration of a TMV particle. Figure reproduced with permission from Ref. 38. Copyright 2018 American Chemical Society.

In addition, several amino acid residues are hypothesized to be responsible for inducing metalation in aqueous solutions.[10] For example, In early 2000s, TMV demonstrated its robustness and versatility as a template to synthesize 1D organic-inorganic nanocomposites. Shenton *et al.*[10] employed TMV as template to synthesize various metal nanoparticles. They successfully demonstrated a uniform coating of silicon dioxide, lead sulfide, cadmium sulfide and iron oxides on the outer surface of TMV at pHs of 2.5 to 9 (Figure 1.3). More interestingly, the silicification

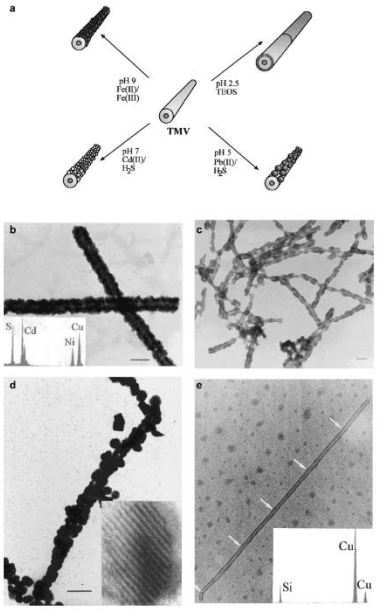

Figure 1.3. a) schematic illustration of metalation on TMV under various synthetic conditions; TEM micrographs of b) Cd-coated TMV; c) iron oxide-coated TMV; d) PbS-coated TMV and e) silica-coated TMV. Figure reproduced with permission from Ref. 10. Copyright 1999 John Wiley & Sons, Inc.

in the presence of TMV resulted in formation of long nanowires due to a head-to-tail style of self-assembly of TMV that was induced by attenuated repulsion between the ends of viral particles under acidic condition.

Furthermore, Dujardin *et al.*[11] illustrated that they were able to take advantage of both outer and inner surface of TMV to grow metal nanoparticles (Figure 1.4 and 1.5). This is achieved by

exploiting the pKas of surface–exposed amino acids on both the outer and inner surfaces and applying appropriate metal precursors. In particular, anionic metal complex accompanied with acidic environment leads to NP growth preferentially on the outer surface of virus particles, which possesses a positive charge whilst the inner surface is charge neutral. On the other hand, under neutral and slightly basic conditions, TMV tends to be positively charged on its exterior and negatively charged on interior. Cationic metal precursors are then selected to target the inner

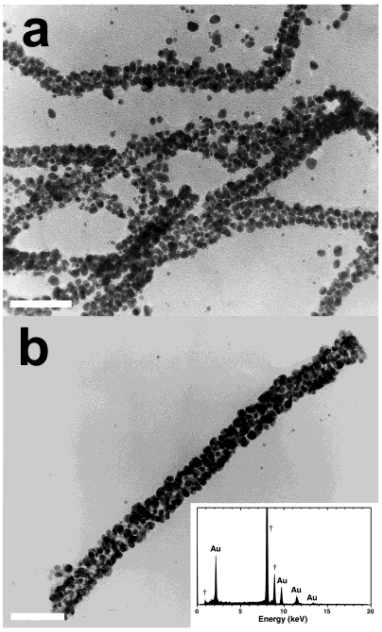

Figure 1.4. a) low magnification and b) high magnification TEM micrographs of Au NPs coated on the exterior of TMV. Figure reproduced with permission from Ref. 11. Copyright 2003 American Chemical Society.

channel and produce TMV–encapsulated nanoparticles. Inspired by these preliminary results, researchers have prepared metal/metal oxide coated TMV nanorods and applied them in device fabrications.[12, 41-43]

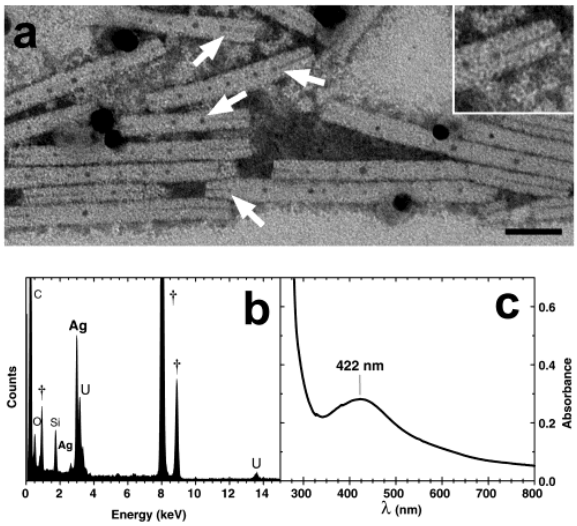

Figure 1.5. Characterizations of Ag NPs grown inside of TMV: a) TEM; b) EDS and c) UV-Vis spectroscopy. Figure reproduced with permission from Ref. 11. Copyright 2003 American Chemical Society.

Thus far, however, TMV-templated biomimetic mineralization only yielded solid NPs or impermeable thin crusts. MOFs are a promising material to be fabricated with TMV, if possible, owing to their various pore structures and diverse composition for a broad variety of applications.

Escherichia coli

Escherichia coli, or *E. coli*, which was first discovered 134 years ago by a German microbiologist, has now become the mostly studied model microorganism. Due to its fast growth rate, ease of handling, inexpensive cost, and flexibility for genetic engineering, *E. coli* is widely employed in food, pharmaceutical and biotechnological industries.[44-45] In fact, nearly 1/3 of agency-approved recombinant proteins in pharmaceutic industry are produced by *E. coli*.[46] It has also been used in industrial production of D-lactate.[47] The production of biohydrogen and value-added small molecules are investigated in lab-scale and more developments are undergoing to pave the way to massive production.

Microorganisms have long been recognized as factories of functional inorganic NPs. For example, magnetosomes were found to fabricate magnetic nanocrystals inside the cells.[48] Though *E. coli* does not produce biomineralized products innately, its cell wall contains reactive component (likely the negatively charged lipopolysaccharides) to induce deposition of NPs. Previous studies have shown that Au and CdS nanoparticles could be synthesized on the exterior of cell membrane of *E. coli*.[49-50] These findings paved the way for biomimetic mineralization of MOFs on *E. coli*.

It is intriguing to investigate the morphology of *E. coli*-templated MOF crystals as MOF growths always result in large crystals. Ideally, a continuous crystalline shell that covers the entire cell membrane to serve as a protective shield is preferred. Moreover, it is important to understand whether the applied syntheses of crystalline shell would impact the viability of the cell.

1.4 Potential Application for Biology@MOF

A New Preservation Strategy for Vaccine

There is a common agreement that storage and delivery of vaccines are still challenging, especially in the developing countries in tropical and subtropical areas. It is due to the protein-based drugs require constant refrigeration within a very narrow temperature range to keep them from denaturation.[51-52] Any lack of proper refrigeration during the manufacturing, shipping, delivering and administrating (it is also called the "cold chain") will lead to undermined or even loss of effect of vaccination, which induces high risks to the patients and, even worse, to the medical staffs who are fighting diseases in the high incidence areas. It is highly desirable that thermally stable vaccines could be invented to save nearly 80%[53] of the cost that is solely spent on the "cold chain", but more importantly, save almost half[54] of global vaccine production from inactivation. The encapsulation with a rigid shell can confine the conformation of proteins thus provide improved

stability of the protein-based drugs. Biomimetic mineralization of MOFs could be a promising strategy for this purpose, as researchers have already shown robust thermal stability of MOF-encapsulated enzymes up to 150 °C.[37]

Improved Cell Viability with MOF Coating

Compared to virus particles, cells are more vulnerable to changes in temperature, pH, nutrient level, and foreign organisms.[55] In contemporary industry, cells are widely used in production of high value chemicals foods, and pharmaceutical drugs,[44-47] thus their viability is crucial to maintain prosperity of manufacturing. Coating with a rigid material can form an exoskeleton to protect the cell against environmental stresses. Though inorganic and polymeric materials have been previously reported as protective shield for cells,[56-59] MOFs maintain certain advantages as being protective whilst permeable.[60-61] Ideally, the MOF shell can inhibit the access of toxic chemicals and cytotoxic enzymes while allowing the transportation of nutrients by the sieving effects of its pore aperture.

1.5 References

1. Nudelman, F.; Sommerdijk Nico, A. J. M. Biomineralization as an Inspiration for Materials Chemistry. *Angew. Chem., Int. Ed.* **2012,** *51*, 6582-6596.

2. Arakaki, A.; Shimizu, K.; Oda, M.; Sakamoto, T.; Nishimura, T.; Kato, T. Biomineralization-inspired synthesis of functional organic/inorganic hybrid materials: organic molecular control of self-organization of hybrids. *Org. Biomol. Chem.* **2015,** *13*, 974-989.

3. Fratzl, P.; Gupta, H. S.; Paschalis, E. P.; Roschger, P. Structure and mechanical quality of the collagen-mineral nano-composite in bone. *J. Mater. Chem.* **2004,** *14*, 2115-2123.

4. Shimizu, K.; Cha, J.; Stucky, G. D.; Morse, D. E. Silicatein α: Cathepsin L-like protein in sponge biosilica. *Proc. Natl. Acad. Sci. U. S. A.* **1998,** *95*, 6234-6238.

5. Crookes-Goodson, W. J.; Slocik, J. M.; Naik, R. R. Bio-directed synthesis and assembly of nanomaterials. *Chem. Soc. Rev.* **2008,** *37*, 2403-2412.

6. Libonati, F.; Buehler Markus, J. Advanced Structural Materials by Bioinspiration. *Adv. Eng. Mater.* **2017,** *19*, 1600787.

7. Yaraghi, N. A.; Kisailus, D. Biomimetic Structural Materials: Inspiration from Design and Assembly. *Annu. Rev. Phys. Chem.* **2015,** *69*, 23-57.

8. Xu, A.-W.; Ma, Y.; Colfen, H. Biomimetic mineralization. *J. Mater. Chem.* **2007,** *17*, 415-449.

9. Liu, B.; Cao, Y.; Huang, Z.; Duan, Y.; Che, S. Silica Biomineralization via the Self-Assembly of Helical Biomolecules. *Adv. Mater.* **2015,** *27*, 479-497.

10. Shenton, W.; Douglas, T.; Young, M.; Stubbs, G.; Mann, S. Inorganic–Organic Nanotube Composites from Template Mineralization of Tobacco Mosaic Virus. *Adv. Mater.* **1999,** *11*, 253-256.

11. Dujardin, E.; Peet, C.; Stubbs, G.; Culver, J. N.; Mann, S. Organization of Metallic Nanoparticles Using Tobacco Mosaic Virus Templates. *Nano Lett.* **2003,** *3*, 413-417.

12. Knez, M.; Sumser, M.; Bittner, A. M.; Wege, C.; Jeske, H.; Martin, T. P.; Kern, K. Spatially Selective Nucleation of Metal Clusters on the Tobacco Mosaic Virus. *Adv. Funct. Mater.* **2004,** *14*, 116-124.

13. Yaghi, O. M.; O'Keeffe, M.; Ockwig, N. W.; Chae, H. K.; Eddaoudi, M.; Kim, J. Reticular synthesis and the design of new materials. *Nature* **2003,** *423*, 705.

14. Furukawa, H.; Cordova, K. E.; O'Keeffe, M.; Yaghi, O. M. The Chemistry and Applications of Metal-Organic Frameworks. *Science* **2013,** *341*, 1230444.

15. Li, Q.; Zhang, W.; Miljanić, O. Š.; Sue, C.-H.; Zhao, Y.-L.; Liu, L.; Knobler, C. B.; Stoddart, J. F.; Yaghi, O. M. Docking in Metal-Organic Frameworks. *Science* **2009,** *325*, 855.

16. Karagiaridi, O.; Lalonde, M. B.; Bury, W.; Sarjeant, A. A.; Farha, O. K.; Hupp, J. T. Opening ZIF-8: A Catalytically Active Zeolitic Imidazolate Framework of Sodalite Topology with Unsubstituted Linkers. *J. Am. Chem. Soc.* **2012,** *134*, 18790-18796.

17. Lu, G.; Farha, O. K.; Zhang, W.; Huo, F.; Hupp, J. T. Engineering ZIF-8 Thin Films for Hybrid MOF-Based Devices. *Adv. Mat.* **2012,** *24*, 3970-3974.

18. Gándara, F.; Furukawa, H.; Lee, S.; Yaghi, O. M. High Methane Storage Capacity in Aluminum Metal–Organic Frameworks. *J. Am. Chem. Soc.* **2014,** *136*, 5271-5274.

19. He, C.; Lu, K.; Lin, W. Nanoscale Metal–Organic Frameworks for Real-Time Intracellular pH Sensing in Live Cells. *J. Am. Chem. Soc.* **2014,** *136*, 12253-12256.

20. Kornienko, N.; Zhao, Y.; Kley, C. S.; Zhu, C.; Kim, D.; Lin, S.; Chang, C. J.; Yaghi, O. M.; Yang, P. Metal–Organic Frameworks for Electrocatalytic Reduction of Carbon Dioxide. *J. Am. Chem. Soc.* **2015,** *137*, 14129-14135.

21. Marshall, R. J.; Griffin, S. L.; Wilson, C.; Forgan, R. S. Single-Crystal to Single-Crystal Mechanical Contraction of Metal–Organic Frameworks through Stereoselective Postsynthetic Bromination. *J. Am. Chem. Soc.* **2015,** *137*, 9527-9530.

22. McGuirk, C. M.; Katz, M. J.; Stern, C. L.; Sarjeant, A. A.; Hupp, J. T.; Farha, O. K.; Mirkin, C. A. Turning On Catalysis: Incorporation of a Hydrogen-Bond-Donating Squaramide Moiety into a Zr Metal–Organic Framework. *J. Am. Chem. Soc.* **2015,** *137*, 919-925.

23. Mondloch, J. E.; Katz, M. J.; Isley Iii, W. C.; Ghosh, P.; Liao, P.; Bury, W.; Wagner, G. W.; Hall, M. G.; DeCoste, J. B.; Peterson, G. W.; Snurr, R. Q.; Cramer, C. J.; Hupp, J. T.; Farha, O. K. Destruction of chemical warfare agents using metal–organic frameworks. *Nat. Mat.* **2015,** *14*, 512.

24. Lim, J.; Lee, E. J.; Choi, J. S.; Jeong, N. C. Diffusion Control in the in Situ Synthesis of Iconic Metal–Organic Frameworks within an Ionic Polymer Matrix. *ACS Appl. Mater. Interfaces* **2018,** *10*, 3793-3800.

25. Sindoro, M.; Yanai, N.; Jee, A.-Y.; Granick, S. Colloidal-Sized Metal–Organic Frameworks: Synthesis and Applications. *Acc. Chem. Res.* **2014,** *47*, 459-469.

26. Zhou, J.; Wang, P.; Wang, C.; Goh, Y. T.; Fang, Z.; Messersmith, P. B.; Duan, H. Versatile Core–Shell Nanoparticle@Metal–Organic Framework Nanohybrids: Exploiting Mussel-Inspired Polydopamine for Tailored Structural Integration. *ACS Nano* **2015,** *9*, 6951-6960.

27. Cho, W.; Lee, H. J.; Oh, M. Growth-Controlled Formation of Porous Coordination Polymer Particles. *J. Am. Chem. Soc.* **2008,** *130*, 16943-16946.

28. Tsuruoka, T.; Furukawa, S.; Takashima, Y.; Yoshida, K.; Isoda, S.; Kitagawa, S. Nanoporous Nanorods Fabricated by Coordination Modulation and Oriented Attachment Growth. *Angew. Chem., Int. Ed.* **2009,** *48*, 4739-4743.

29. Cravillon, J.; Nayuk, R.; Springer, S.; Feldhoff, A.; Huber, K.; Wiebcke, M. Controlling Zeolitic Imidazolate Framework Nano- and Microcrystal Formation: Insight into Crystal

Growth by Time-Resolved In Situ Static Light Scattering. *Chem. Mater.* **2011,** *23*, 2130-2141.

30. Umemura, A.; Diring, S.; Furukawa, S.; Uehara, H.; Tsuruoka, T.; Kitagawa, S. Morphology Design of Porous Coordination Polymer Crystals by Coordination Modulation. *J. Am. Chem. Soc.* **2011,** *133*, 15506-15513.

31. Zhang, J.; Zhang, T.; Xiao, K.; Cheng, S.; Qian, G.; Wang, Y.; Feng, Y. Novel and Facile Strategy for Controllable Synthesis of Multilayered Core–Shell Zeolitic Imidazolate Frameworks. *Cryst. Growth Des.* **2016,** *16*, 6494-6498.

32. Ji, H.; Hwang, S.; Kim, K.; Kim, C.; Jeong, N. C. Direct in Situ Conversion of Metals into Metal–Organic Frameworks: A Strategy for the Rapid Growth of MOF Films on Metal Substrates. *ACS Appl. Mater. Interfaces* **2016,** *8*, 32414-32420.

33. Jian, M.; Liu, B.; Liu, R.; Qu, J.; Wang, H.; Zhang, X. Water-based synthesis of zeolitic imidazolate framework-8 with high morphology level at room temperature. *RSC Adv.* **2015,** *5*, 48433-48441.

34. Park, K. S.; Ni, Z.; Côté, A. P.; Choi, J. Y.; Huang, R.; Uribe-Romo, F. J.; Chae, H. K.; O'Keeffe, M.; Yaghi, O. M. Exceptional chemical and thermal stability of zeolitic imidazolate frameworks. *Proc. Natl. Acad. Sci. U. S. A.* **2006,** *103*, 10186-10191.

35. Pan, Y.; Liu, Y.; Zeng, G.; Zhao, L.; Lai, Z. Rapid synthesis of zeolitic imidazolate framework-8 (ZIF-8) nanocrystals in an aqueous system. *Chem. Commun.* **2011,** *47*, 2071-2073.

36. Lyu, F.; Zhang, Y.; Zare, R. N.; Ge, J.; Liu, Z. One-Pot Synthesis of Protein-Embedded Metal–Organic Frameworks with Enhanced Biological Activities. *Nano Lett.* **2014,** *14*, 5761-5765.

37. Liang, K.; Ricco, R.; Doherty, C. M.; Styles, M. J.; Bell, S.; Kirby, N.; Mudie, S.; Haylock, D.; Hill, A. J.; Doonan, C. J.; Falcaro, P. Biomimetic mineralization of metal-organic frameworks as protective coatings for biomacromolecules. *Nat. Commun.* **2015,** *6*, 7240.

38. Li, S.; Dharmarwardana, M.; Welch, R. P.; Benjamin, C. E.; Shamir, A. M.; Nielsen, S. O.; Gassensmith, J. J. Investigation of Controlled Growth of Metal–Organic Frameworks on Anisotropic Virus Particles. *ACS Appl. Mater. Interfaces* **2018,** *10*, 18161-18169.

39. Schlick, T. L.; Ding, Z.; Kovacs, E. W.; Francis, M. B. Dual-Surface Modification of the Tobacco Mosaic Virus. *J. Am. Chem. Soc.* **2005,** *127*, 3718-3723.

40. Bruckman, M. A.; Steinmetz, N. F. Chemical Modification of the Inner and Outer Surfaces of Tobacco Mosaic Virus (TMV). In *Virus Hybrids as Nanomaterials: Methods and Protocols*, Lin, B.; Ratna, B., Eds. Humana Press: Totowa, NJ, 2014; pp 173-185.

41. Royston, E.; Ghosh, A.; Kofinas, P.; Harris, M. T.; Culver, J. N. Self-Assembly of Virus-Structured High Surface Area Nanomaterials and Their Application as Battery Electrodes. *Langmuir* **2008,** *24*, 906-912.

42. Gerasopoulos, K.; Pomerantseva, E.; McCarthy, M.; Brown, A.; Wang, C.; Culver, J.; Ghodssi, R. Hierarchical Three-Dimensional Microbattery Electrodes Combining Bottom-Up Self-Assembly and Top-Down Micromachining. *ACS Nano* **2012,** *6*, 6422-6432.

43. Gnerlich, M.; Ben-Yoav, H.; Culver, J. N.; Ketchum, D. R.; Ghodssi, R. Selective deposition of nanostructured ruthenium oxide using Tobacco mosaic virus for micro-supercapacitors in solid Nafion electrolyte. *J. Power Sources* **2015,** *293*, 649-656.

44. Overton, T. W. Recombinant protein production in bacterial hosts. *Drug Discov. Today* **2014,** *19*, 590-601.

45. Wendisch, V. F.; Brito, L. F.; Gil Lopez, M.; Hennig, G.; Pfeifenschneider, J.; Sgobba, E.; Veldmann, K. H. The flexible feedstock concept in Industrial Biotechnology: Metabolic engineering of Escherichia coli, Corynebacterium glutamicum, Pseudomonas, Bacillus and yeast strains for access to alternative carbon sources. *J. Biotechnol.* **2016,** *234*, 139-157.

46. Huang, C., Jr.; Lin, H.; Yang, X. Industrial production of recombinant therapeutics in Escherichia coli and its recent advancements. *J. Ind. Microbiol. Biotechnol.* **2012,** *39*, 383-399.

47. Zhou, L.; Cui, W.; Liu, Z.; Zhou, Z. Metabolic engineering strategies for D-lactate over production in Escherichia coli. *J. Chem. Technol. Biotechnol.* **2016,** *91*, 576-584.

48. Faivre, D.; Schüler, D. Magnetotactic Bacteria and Magnetosomes. *Chem. Rev.* **2008,** *108*, 4875-4898.

49. Du, L.; Jiang, H.; Liu, X.; Wang, E. Biosynthesis of gold nanoparticles assisted by Escherichia coli DH5α and its application on direct electrochemistry of hemoglobin. *Electrochem. Commun.* **2007,** *9*, 1165-1170.

50. Sweeney, R. Y.; Mao, C.; Gao, X.; Burt, J. L.; Belcher, A. M.; Georgiou, G.; Iverson, B. L. Bacterial Biosynthesis of Cadmium Sulfide Nanocrystals. *Chem. & Biol.* **2004,** *11*, 1553-1559.

51. Rexroad, J.; Wiethoff, C. M.; Jones, L. S.; Middaugh, C. R. Lyophilization and the Thermostability of Vaccines. *Cell Preserv. Technol.* **2002,** *1*, 91-104.

52. Hansen, L. J. J.; Daoussi, R.; Vervaet, C.; Remon, J. P.; De Beer, T. R. M. Freeze-drying of live virus vaccines: A review. *Vaccine* **2015,** *33*, 5507-5519.

53. Chen, X.; Fernando, G. J. P.; Crichton, M. L.; Flaim, C.; Yukiko, S. R.; Fairmaid, E. J.; Corbett, H. J.; Primiero, C. A.; Ansaldo, A. B.; Frazer, I. H.; Brown, L. E.; Kendall, M. A. F. Improving the reach of vaccines to low-resource regions, with a needle-free vaccine delivery device and long-term thermostabilization. *J. Controlled Release* **2011,** *152*, 349-355.

54. Zhang, J.; Pritchard, E.; Hu, X.; Valentin, T.; Panilaitis, B.; Omenetto, F. G.; Kaplan, D. L. Stabilization of vaccines and antibiotics in silk and eliminating the cold chain. *Proc. Natl. Acad. Sci. U. S. A.* **2012,** *109*, 11981.

55. Liu, J.; Wen, J.; Zhang, Z.; Liu, H.; Sun, Y. Voyage inside the cell: Microsystems and nanoengineering for intracellular measurement and manipulation. *Microsyst. Nanoeng.* **2015,** *1*, 15020.

56. Yang, S. H.; Kang, S. M.; Lee, K.-B.; Chung, T. D.; Lee, H.; Choi, I. S. Mussel-Inspired Encapsulation and Functionalization of Individual Yeast Cells. *J. Am. Chem. Soc.* **2011,** *133*, 2795-2797.

57. Kempaiah, R.; Salgado, S.; Chung, W. L.; Maheshwari, V. Graphene as membrane for encapsulation of yeast cells: protective and electrically conducting. *Chem. Commun.* **2011,** *47*, 11480-11482.

58. Kaehr, B.; Townson, J. L.; Kalinich, R. M.; Awad, Y. H.; Swartzentruber, B. S.; Dunphy, D. R.; Brinker, C. J. Cellular complexity captured in durable silica biocomposites. *Proc. Natl. Acad. Sci. U. S. A.* **2012,** *109*, 17336.

59. Baca, H. K.; Ashley, C.; Carnes, E.; Lopez, D.; Flemming, J.; Dunphy, D.; Singh, S.; Chen, Z.; Liu, N.; Fan, H.; López, G. P.; Brozik, S. M.; Werner-Washburne, M.; Brinker, C. J. Cell-Directed Assembly of Lipid-Silica Nanostructures Providing Extended Cell Viability. *Science* **2006,** *313*, 337.

60. Liang, K.; Richardson, J. J.; Cui, J.; Caruso, F.; Doonan, C. J.; Falcaro, P. Metal–Organic Framework Coatings as Cytoprotective Exoskeletons for Living Cells. *Adv. Mat.* **2016,** *28*, 7910-7914.

61. Liang, K.; Richardson, J. J.; Doonan, C. J.; Mulet, X.; Ju, Y.; Cui, J.; Caruso, F.; Falcaro, P. An Enzyme-Coated Metal–Organic Framework Shell for Synthetically Adaptive Cell Survival. *Angew. Chem., Int. Ed.* **2017,** *56*, 8510-8515.

CHAPTER 2

TEMPLATE DIRECTED SYNTHESIS OF POROUS AND PROTECTIVE CORE-SHELL BIONANOPARTICLES

Authors - Shaobo Li, Madushani Dharmarwardana, Raymond P. Welch, Yixin Ren, Christina M. Thompson, Ronald A. Smaldone, Jeremiah J. Gassensmith

The Department of Chemistry and Biochemistry, BE26

The University of Texas at Dallas

800 West Campbell Road

Richardson, Texas, 75080-3021

Reprinted with permission from Li, S.; Dharmarwardana, M.; Welch, R. P.; Ren, Y.; Thompson, C. M.; Smaldone, R. A.; Gassensmith, J. J. Template Directed Synthesis of Porous and Protective Core-Shell Bionanoparticles. *Angew. Chem., Int. Ed.* **2016,** *55*, 10691–10696.

2.1 Introduction

Metal organic frameworks (MOFs) represent a family of microporous crystalline materials with high specific surface areas and extended porosity and have attained a level of preeminence owing to their synthetic tunability. A MOF is constructed by coordinating rigid organic "struts" to a metal ion or cluster "node" to form a crystalline material with defined pore structure, pore size, and chemical composition.[1-2] This seemingly infinite combination of metal nodes and organic struts has enabled highly tunable design strategies for specific needs[3-7] like gas storage,[8-10] sensing,[11-12] catalysis,[13-16] energy,[17-19] and in bio-medical applications.[20-22] An issue arising in many of these applications, however, has been difficulty in controlling the crystallite morphology, which typically yields bulk MOF powders with relatively large crystal size, random shape, and poor monodispersity. There is an articulated[23] interest in controlling the morphology of MOF crystallites owing to the need for nanometer scale uniformity in biomedical and optoelectronics applications. The synthetic strategies so far employed to regulate the size and morphology of MOF crystals have generally been achieved by addition of metal-binding reagents such as ligands, surfactants, or polymers with chelating functional moieties.[24-28] Although these strategies afford regulation of size, the as-obtained MOF particles are typically several hundred nanometers in size. More recently, MOF core-shell nanoparticles in the 100 nm range with good monodispersity have emerged,[29-35] though control over shape is not always high, resulting in irregular spheres or cubes. Virus nanoparticles offer a level of control unavailable in synthetic systems as the surface chemistry can be altered by either chemical or genetic manipulation.[36-40] We selected tobacco mosaic virus (TMV), a tubular viral particle that contains 2,130 identical coat proteins self-assembled around a single strand of RNA. Being 300 nm long and only 18 nm wide, the anisotropy

of the virus has made it an attractive target for applications in photonics,[41] light harvesting solar arrays,[42-43] and MRI contrast agents.[44-45] TMV is also attractive as it can be isolated in gram quantities from a kilogram of tobacco leaves. Each coat protein possesses solvent-accessible amino acid residues—tyrosine on the exterior and glutamates on the interior—and these anionic residues have proven that they are available for chemical conjugation.[46] Furthermore, the robustness of TMV has allowed it to play a versatile role as a bio-template for fabrication of organic or inorganic materials[47-52] and we reasoned that these qualities would make it useful in the production of core-shell bionanoparticle (CSBN) MOF frameworks with tightly regulated shell thickness, width, and length. To obtain aqueous solution-stable CSBNs using MOFs, we turned to hydrolytically stable ZIF-8,[53] which is formed from the coordination of methyl imidazole ligands (HMIM) and Zn, and has recently been shown to nucleate and grow on enzymes (naked[54-58] or polymer-coated[59-60]) in aqueous solution. Unlike enzymes, viruses are comparatively massive and are formed from highly symmetric quaternary structure; thus, we hypothesized they would give rise to regular nanoscopic shapes (Figure 2.1).

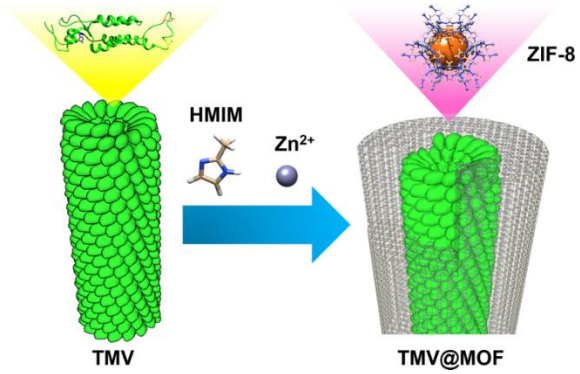

Figure 2.1. Schematic illustration of synthesis and formation of TMV@ZIF-8 rod-shaped nanocomposites.

In this communication we show that, using TMV as a template, the as–fabricated TMV@ZIF-8 retained the highly anisotropic rod shape of the parent virus. We were able to tune the thickness of the MOF shell by modifying the synthetic conditions. The as-obtained TMV@ZIF-8 composite demonstrates good stability in organic solvents and at high temperature. The surface exposed tyrosine groups of the TMV are still reactive while inside the MOF shell and coupling reactions performed through the MOF do not undermine the integrity of rod–shaped hybrids. Most incredibly, even after soaking the TMV@ZIF-8 in pure methanol overnight, we were able to remove the ZIF-8 shell and show the virus itself could be reclaimed without damage under these highly denaturing conditions.

2.2 Results & Discussion

For our initial experiments, a desalted virus solution was first mixed with an aqueous solution of HMIM. Upon addition of an aliquot of $Zn(OAc)_2$ the reaction mixture immediately became turbid followed by flocculate formation. After sitting on the bench for 16 hours, the centrifuged solid was washed with ultrapure water twice to obtain an off-white suspension in water. We were initially pleased to find the anticipated rod structures by SEM but frustrated to discover that the rods were very unstable—when removed from the mother liquor solution containing Zn and HMIM and placed in deionized (DI) water they collapsed into flaky cubes overnight (Figure 2.2). From powder X-ray diffraction (PXRD) analysis of the as-synthesized rods, we observed that the shells contained the expected ZIF-8 but also reflections corresponding to a significant amount of crystalline $Zn(OAc)_2$ (Figure 2.3). This led us to conduct an investigation into the optimization of our synthetic conditions to reduce unwanted $Zn(OAc)_2$ growth and improve the stability of our rod composites. As a result of this investigation, we not only found that we could greatly affect the

physical stability of the composites but also the shell thickness. A key observation was that when the HMIM:Zn molar ratio was low, the TMV@ZIF-8 core-shell composites had thinner shells and, conversely, at higher HMIM:Zn ratios, the shells thickened.

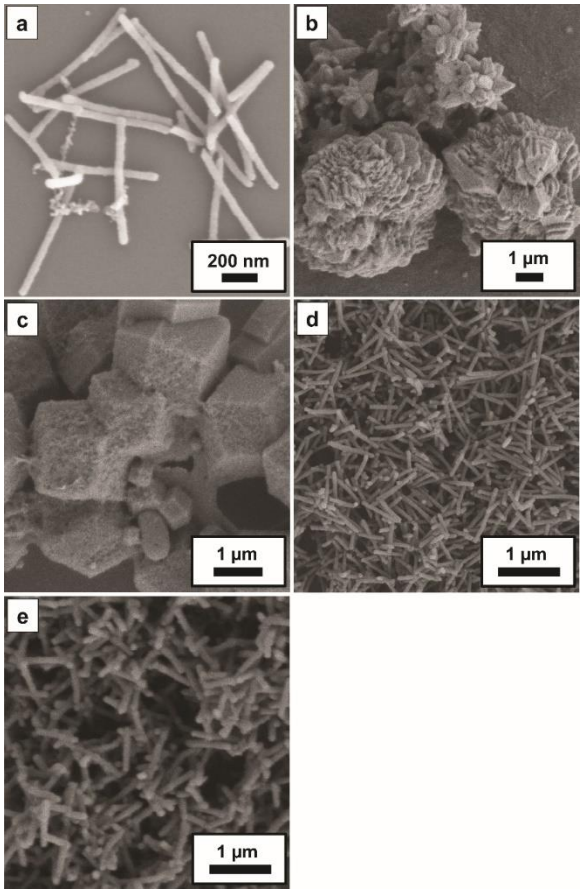

Figure 2.2. SEM micrographs of the first and unstable products we made. Shown are the a) as-prepared TZ-P1 rod composite; b) TZ-P1 after soaking in 18.2 MΩ DI H2O for 16 h; c) TZ-P1 after soaking in pure methanol for 16 h; These unstable materials are compared to d) TZ-thin and e) TZ-thick after soaking in 18.2 MΩ DI H_2O for 16 h.

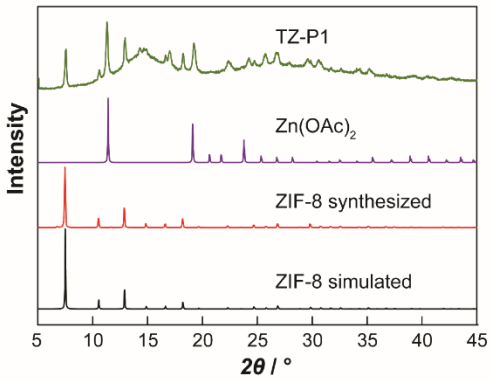

Figure 2.3. PXRD pattern of simulated ZIF-8, as-synthesized ZIF-8, zinc acetate and unstable prototype TZ-P1. From these data it appears that the initial TZ-P1 contained crystalline $Zn(OAc)_2$, making it unstable in solutions that did not contain the metal precursor salt.

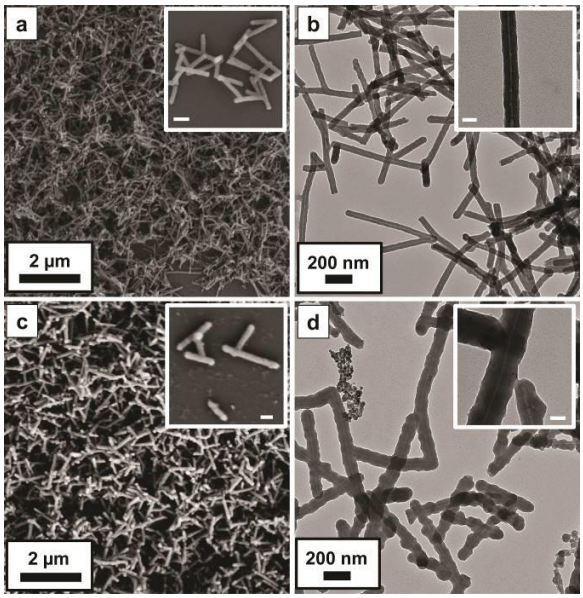

Figure 2.4. a) SEM and b) TEM of as-synthesized TZ-thin. c) SEM and d) TEM of as-synthesized TZ-thick. Inset scale bar: a), c) 200 nm; b), d) 50 nm.

Two representative products of this investigation are presented in Figure 2.4, denoted as TZ-thin (micrographs shown in Figure 2.4 a and b) and TZ-thick (Figure 2.4 c and d). Synthetically, these two composites are differentiated by the HMIM:Zn molar ratio used in their preparation. Specifically, the TZ-thin composite was prepared from a 20:1 ratio and the thicker wall of TZ-

thick was obtained when that ratio was increased to 40:1. SEM analysis shows that both composites form regular and homogenous rods with very tightly controlled thickness. TZ-thin, for instance, is 70 nm in diameter and TZ-thick is 100 nm. We found we could control the surface coating of the TMV@ZIF-8 as well by changing the concentration used in drop casting. The dense forest shown in the SEM micrographs are a result of drop casting at high concentrations. TEM shows the viral interior, which arises from the low contrast TMV rod residing within the shell (Figure 2.4 b and d). This provides direct evidence of successful ZIF-8 encapsulation of the tubular virus particle. We also observed rods much longer than 300 nm by SEM and TEM. This arises from TMV's propensity to align head-to-tail.[47, 50] This phenomenon is illustrated in the insert of Figure 2.4 d, which shows clearly one of these supramolecular junctions where the virus particles line up in a head-to-tail fashion.

Crystallinity was confirmed by PXRD analysis showing reflections in excellent agreement with the simulated ZIF-8 pattern (Figure 2.5 a). Thermogravimetric analysis (Figure 2.5 b) under air atmosphere shows a two-stage weight loss in both TZ-thin and TZ-thick, starting from 250 to 350 °C, which we attributed to the decomposition of the proteins, then a sharp decrease at 450 °C consistent with decomposition of pure ZIF-8. Permanent porosity of the resulting shell was confirmed by nitrogen absorption analysis at 77 K (Figure 2.5 c). The final BET surface area values of the separate composites show an expected decrease in available surface area associated with the incorporation of the virus. Solution stability and synthetic yield were analyzed by functionalizing the inner channel of the TMV with a fluorescent FITC tag (fTMV, see Section 2.4) and then growing the ZIF-8 shell around the resulting virus. Following growth and centrifugation of the

composite, we found nearly undetectable levels of fluorescence remaining in the growth solution (Figure 2.5 d, inset 1), indicating a near quantitative capture of fTMV. To determine if TMV could

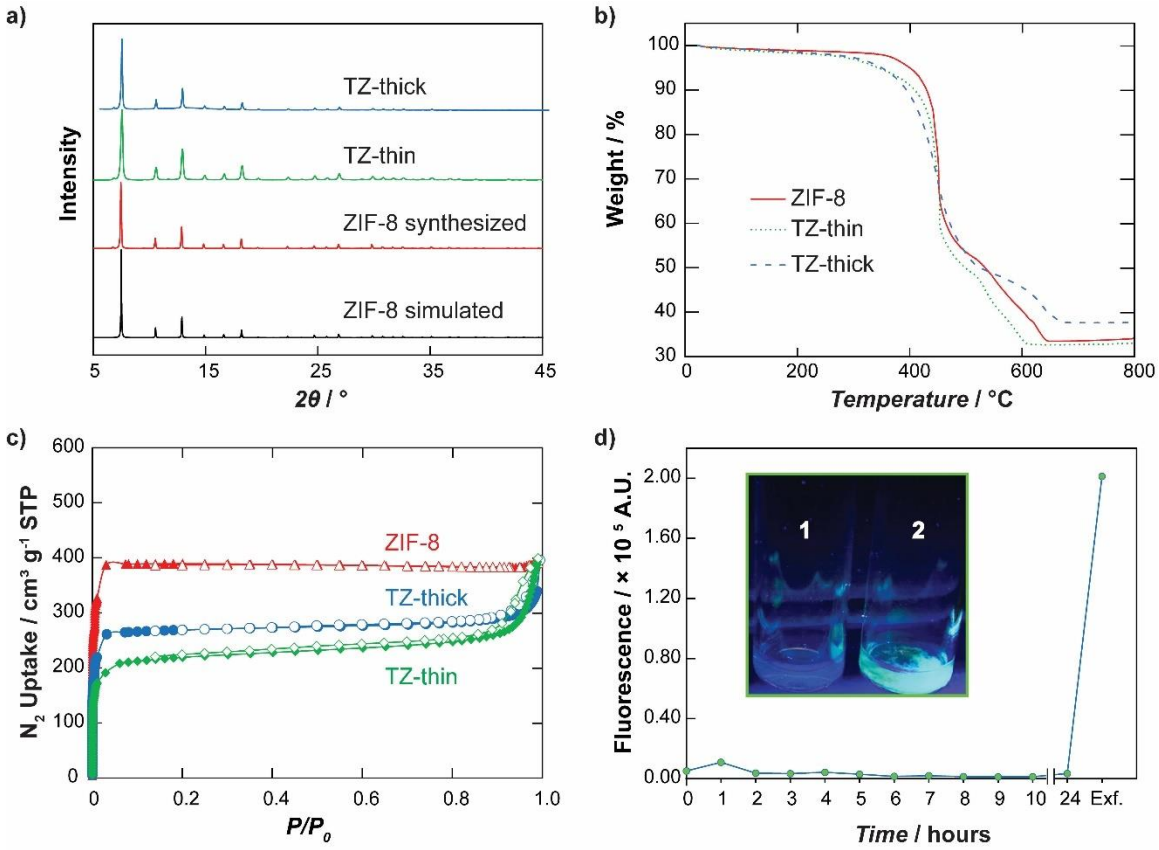

Figure 2.5. a) PXRD of simulated ZIF-8, synthesized ZIF-8, TZ-thin and TZ-thick. b) TGA curves of ZIF-8, TZ-thin and TZ-thick obtained in air atmosphere. c) N_2 sorption isotherm of ZIF-8, TZ-thin and TZ-thick. The calculated BET surface area of ZIF-8, TZ-thick and TZ-thin is 1537, 1053 and 847 m^2/g, respectively. d) Fluorescence measurement of solution after centrifugation at each time point and after exfoliation of ZIF-8 (Exf.); inset: 1) growth solution and 2) fTMV@ZIF-8 under UV light.

escape from the ZIF-8 and re-enter the solution, we tested the fluorescence of a fTMV@ZIF-8 solution (Figure 2.5 d insert 2) over a 24 h period. As shown in Figure 2.5 d the fluorescence never increased until the shell was removed by treatment with EDTA, indicating that the TMV was

unable to leave the ZIF-8 shell and enter into the solution. These data clearly indicate that ZIF-8 shell growth is both high yielding and robust.

An advantage to emerge from encapsulating biomaterials has been stability[55] against environmental stressors such as organic solvents and high temperature, which would typically denature a protein. The stability of the resultant TZ-thin and TZ-thick composites were thus tested by soaking them in organic solvents of varying polarity. After soaking, we looked at the resulting rods by SEM to confirm the composites retained their distinctive morphology following a 16 h soak (Figure 2.6 and 2.7).

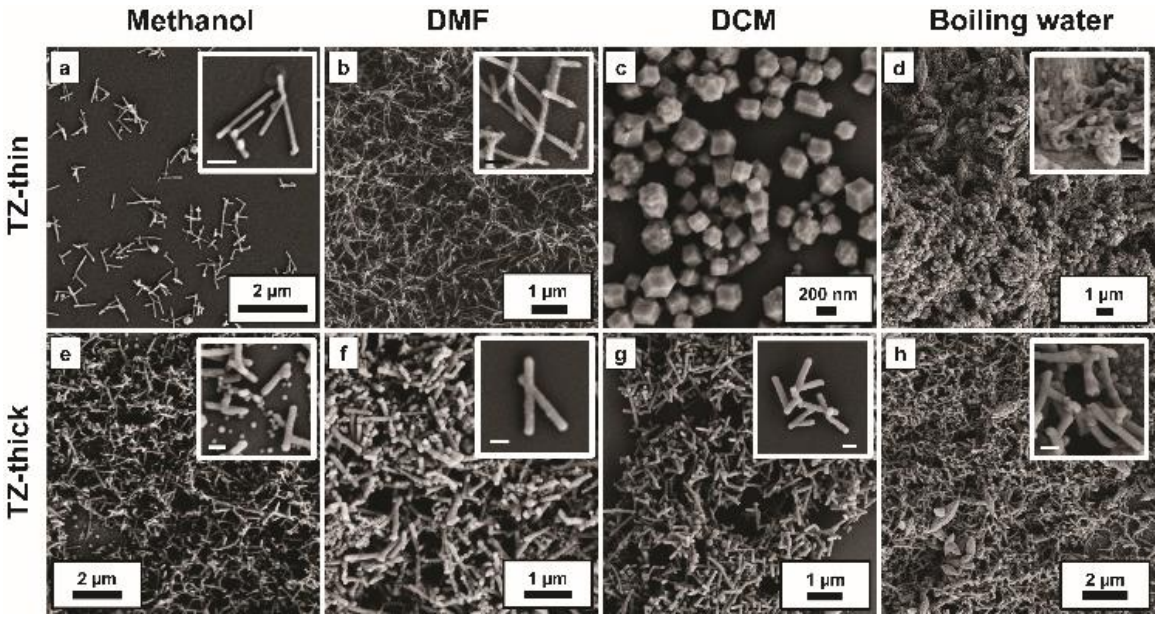

Figure 2.6. SEM of TZ-thin after soaking in a) methanol, b) DMF, c) DCM for 16 h, and in d) boiling water for 20 min. TZ-thick after soaking in e) methanol, f) DMF, g) DCM for 16 h, and in h) boiling water for 20 min. Inset scale bar: a) 300 nm; b, d, e, f, g and h) 200 nm.

Both composites fared well in polar solvents (methanol and DMF) and, quite remarkably, TZ-thick was able to soak in DCM[61] without structural degradation while TZ-thin recrystallized into cuboid

particles of ZIF-8 (Figure 2.6 c and g). We were able to further demonstrate the structural stability of TZ-thick by showing the rod-shape of the composite was largely retained even after boiling in

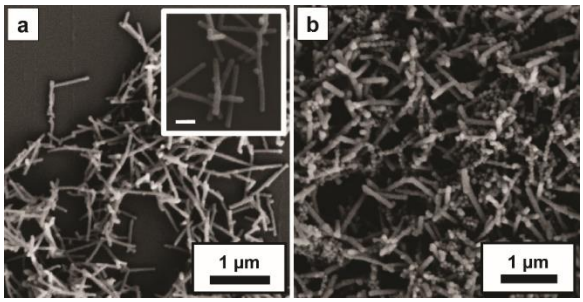

Figure 2.7. SEM micrographs of (a) TZ-thin (inset scale bar= 200 nm) and (b) TZ-thick after soaking in acetonitrile for 16 h.

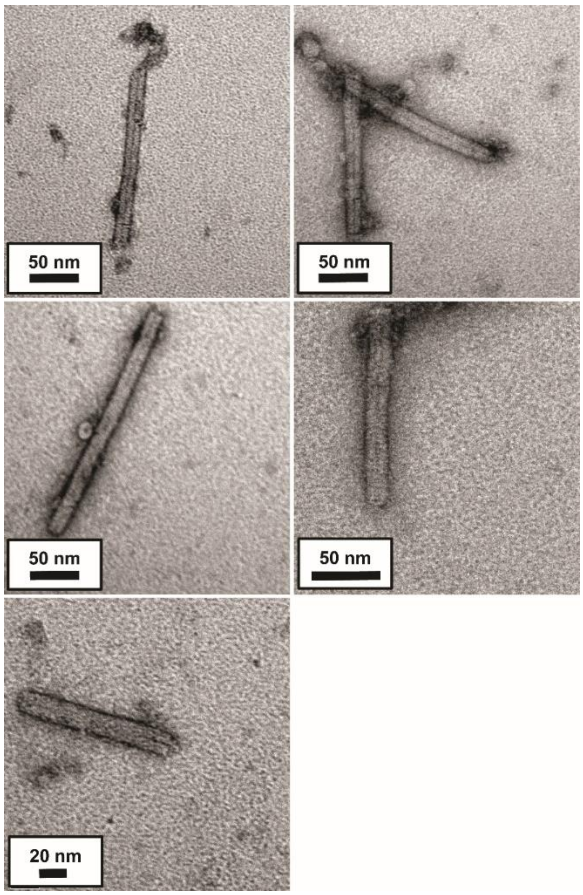

Figure 2.8. Representative TEM micrographs of TMV virus particle obtained following exfoliation of the ZIF-8 shell in a sample of TZ-thick that had been soaked for 16 h in methanol. TZ-thick was immersed in exfoliation solution to remove the ZIF-8 shell.

Figure 2.9. TMV functionalized with diazonium dye after soaking in methanol for 16 h. The TMV denatured and formed a gel within 30 min. The TMV is functionalized with a *p*-nitrodiazo dye to better visualize the denaturing.

water for 20 min (Figure 2.6 h). We were even able to recover the intact virus after soaking the composite in methanol overnight for 16 h by exfoliating the MOF shell using an aqueous solution of EDTA. Without the ZIF-8 shell, methanol rapidly turns TMV into a slimy gel (Figures 2.8 and 2.9). These results demonstrate that a thick MOF shell serves as robust chainmail for the viral template against a denaturing solvent.[62]

A key benefit to MOFs is their permanent porosity and hitherto, strategies used to create biomimetically mineralized shells on TMV essentially use the protein core as a sacrificial template. This means that the functional group rich surface under the shell is no longer accessible. Since ZIF-8 contains pores that allow for the diffusion of small molecules,[63-69] we wondered if we could still perform bioconjugation reactions on the TMV surface in TMV@ZIF-8. To demonstrate this, we attempted a classic diazonium coupling reaction[70] to ascertain if the viral core is capable of post-functionalization after formation of the crystalline MOF shell. The reaction procedure is illustrated in Figure 2.10 a.

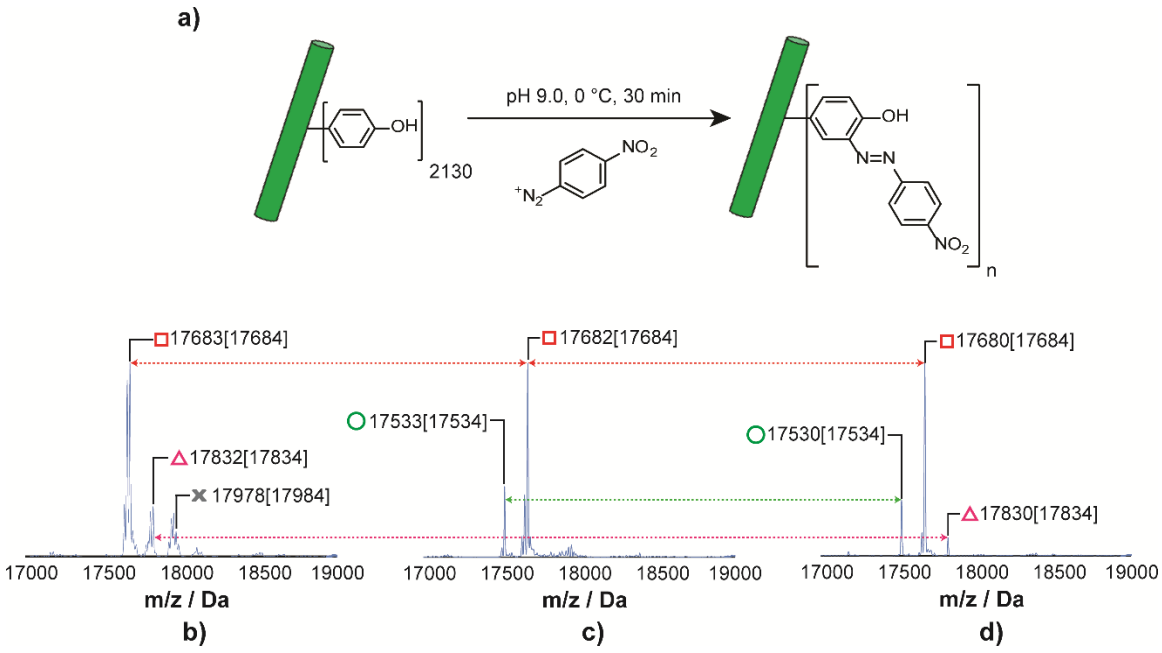

Figure 2.10. a) Diazonium coupling reaction on tyrosine group on TMV. ESI-MS spectrum of TMV coat protein obtained from b) native TMV, c) TZ-thin and d) TZ-thick after diazonium coupling reaction; theoretical mass is quoted for unmodified coat protein (circle), coat protein with one (square), two (triangle), and three (**X**) functionalized residues.

A solution of *p*-nitrobenzene diazonium salt was mixed with TZ-thin solution at 0 °C. The whitish starting material quickly turned orange, indicating the formation of a nitrobenzyl diazo dye on the surface of the virus. After 30 min, the reaction mixture was centrifuged and the mother liquor was decanted. The solid was thoroughly washed with DI water and then suspended in glacial acetic acid to dissolve ZIF-8 and precipitate the RNA for analysis by ESI-MS. The deconvoluted mass spectrum, shown in Figure 2.10 c, shows two intense peaks at 17533 Da and 17682 Da corresponding to unfunctionalized native coat protein and coat protein functionalized with the diazo dye, respectively. Curiously, when the reaction was repeated on TZ-thick,[71] the yield increased (Figure 2.10 d). This was a slightly surprising result considering that the shell is thicker. Following removal of the ZIF-8 shell with EDTA, we confirmed by TEM that TZ-thick retained

its quaternary structure after the bioconjugation reaction. As shown in Figure 2.11 c-f, viral particles stay intact after reaction and exfoliation with EDTA.

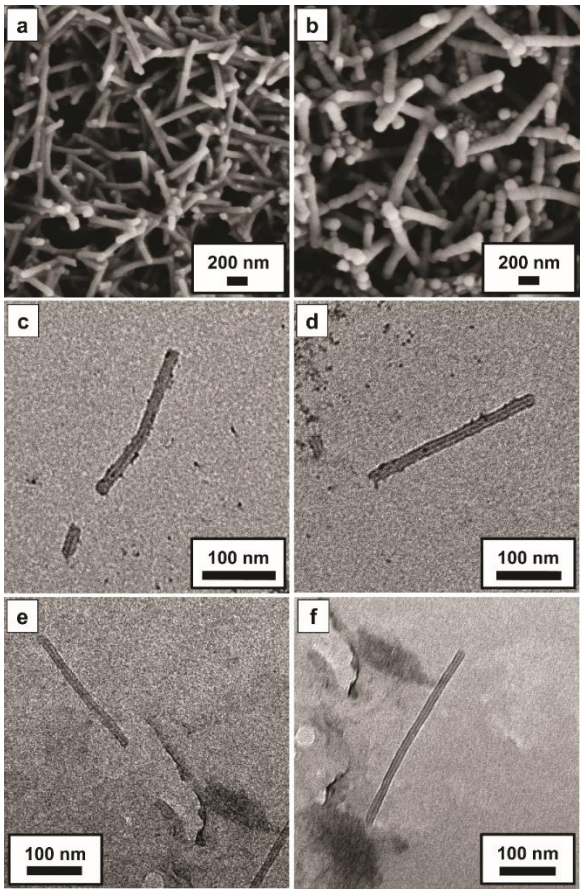

Figure 2.11. SEM micrographs of a) TZ-thin and b) TZ-thick after the diazonium coupling reaction. Notably, there has been no change in morphology; c-f) TEM micrographs of TMV virus particle obtained from TZ-thick after the diazonium reaction and exfoliation of the ZIF-8 shell.

2.3 Conclusion

In conclusion, we have successfully prepared TMV@ZIF-8 rod-shaped CSBNs with tunable shell thickness. Morphological (shell thickness) control is possible by tuning the ligand:metal ratio during the shell growth phase. The rod-like core-shell composites are stable in polar organic solvents for 16 h. The core-shell particles with thicker shells show extended stability in low

polarity organic solvents and at higher temperature. Post-functionalization on the viral exterior via diazonium coupling reaction is possible, demonstrating that these materials will likely have value to a broad audience. Our synthetic strategy not only provides a novel method for size and morphological control of MOF core-shell systems, but also improves the stability of TMV without losing functionalizability of surface-exposed tyrosine residues. We envision that this synthetic strategy will allow design and fabrication of one-dimensional high aspect ratio nanoparticles with more sophisticated functionalities accompanied with mass storage or transfer. This novel prototype may benefit applications such as drug delivery, imaging, sensing, and catalysis.

2.4 Experimental

2.4.1 - Chemicals

Glacial acetic acid, acetonitrile, aminoguanidine bicarbonate, boric acid, 2-bromoethanamine hydrobromide, 1-butanol, chloroform, cupric sulfate pentahydrate, dichloromethane (DCM), diethyl ether, 1-(3-dimethylaminopropyl)-3-ethylcarbodiimide hydrochloride (EDC), dimethylsulfoxide (DMSO), ethylenediaminetetraacetic acid, (EDTA), fluorescein isothiocyanate (FITC), hydrochloric acid, 1-hydroxybenzotriazole hydrate (HOBt), anhydrous magnesium sulfate, *β*-mercaptoethanol, methanol, 2-methylimidazole (HMIM), 4-nitroaniline, polyethylene glycol 8000 (PEG 8000), potassium hydroxide, propargylamine, sodium ascorbate, sodium azide, sodium chloride, sodium hydroxide, sodium nitrite, *p*-toluenesulfonic acid monohydrate, triethylamine, tris(3-hydroxypropyltriazolylmethyl)amine (THPTA), Triton X-100 surfactant, and zinc acetate dihydrate were purchased from Alfa Aesar, Acros Organics, Fisher Scientific, or Sigma Aldrich, and used as received without further purification. 18.2 MΩ DI H_2O was obtained from an ELGA

PURELAB flex water purification system or a Thermo Scientific Barnstead NANOpure water purification system.

2.4.2 - Centrifuges

All microcentrifuge tubes were centrifuged using a Beckman Coulter Microfuge 16 Microcentrifuge. TMV isolation centrifugation was carried out using a Beckman Coulter Optima L-100 XP Ultracentrifuge with a Type 45 Ti rotor. Sartorius Vivaspin Turbo centrifugal concentrators were centrifuged using a Beckman Coulter Allegra X-14R Centrifuge with a SX4750 rotor.

2.4.3 - Electron Microscopy

Scanning electron microscopy (SEM) was conducted on a Zeiss Supra 40 Scanning Electron Microscope with an accelerating voltage of 2.5 kV. To enhance the conductivity, the sample was treated with gold sputtering method prior to microscope characterization. Transmission electron microscopy (TEM) was conducted by FEI Tecnai G2 Spirit Biotwin transmission electron microscope with an accelerating voltage of 120 kV. For TZ-thin and TZ-thick, the diluted sample suspension was directly cast on copper grid without negative staining. The purified exfoliated TZ-thick sample, which simply contains a dilute solution of TMV, was treated with negative staining using 2% uranyl acetate aqueous solution for 30 s.

2.4.4 - Powder X-ray Diffraction (PXRD)

PXRD data for ZIF-8, TMV@ZIF-8 composites were collected using a Bruker D8 Advance powder X-ray diffractometer with CuKα (1.54060 Å) at 40 kV and 30 mA. 2θ was measured from 5° to 80° with 0.02° step size.

2.4.5 - Thermogravimetric Analysis (TGA)

Thermal stability analysis for ZIF-8, TZ-thin and TZ-thick was conducted on a TA Instruments Q500 Thermogravimetric Analyzer under air atmosphere. The heating ramp was set as 10 °C/min from 25 to 800 °C.

2.4.6 - N_2 Sorption Analysis

Low-pressure gas adsorption experiments of activated ZIF-8, TZ-thin and TZ-thick (up to 760 Torr) were carried out on a Micromeritics ASAP 2020 surface area analyzer. Ultrahigh-purity-grade N_2, (obtained from Airgas Corporation) was used for all adsorption measurements. N_2 (77 K) isotherms were measured using a liquid nitrogen bath. Brunauer-Emmett-Teller (BET) surface areas were calculated using the relative pressure range 0.01-0.1 P/P_0. Pore size distributions were determined using a non-local density functional theory (NLDFT) carbon slit-pore model in the Micromeritics Software Package.

2.4.7 - Fluorescence

Fluorescence measurements were recorded on a Synergy™ H4 Hybrid Multi-Mode Microplate Reader.

2.4.8 - Electrospray Ionization Mass Spectrometry (ESI-MS)

Modified TMV samples were characterized by LC/ESI-MS system composed of Agilent 1100 series HPLC system followed by 4000 QTRAP mass spectrometer. HPLC was performed using reverse phase Agilent Zorbax® C18 (150 mm) column with acetonitrile:18.2 MΩ DI H_2O gradient (1 mL/min) mobile phase containing 0.1% acetic acid. Spectra obtained from Analyst software (4000 QTRAP) were deconvoluted using Peakview 2.1 software from AB SCIEX.

2.4.9 - NanoDrop

NanoDrop UV-Vis measurements were performed on a Thermo Scientific NanoDrop 2000 Spectrophotometer.

2.4.10 - Nuclear Magnetic Resonance Spectroscopy (NMR)

NMR spectroscopy was performed on a Bruker Ascend 500 MHz Spectrometer.

2.4.11 - Isolation of TMV

TMV was isolated from infected *N. Benthamiana* leaves according to a modification of a published procedure.[72] The tobacco plants were grown and infected in-house, and infected leaves were collected and stored at -80 °C until needed. 100 g of leaves were pulverized with a mortar and pestle and homogenized in an ice cold extraction buffer (0.1 M pH 7.4 KP buffer, 0.2% (v/v) β-mercaptoethanol). The mixture was filtered through cheesecloth to remove the plant solids, and the filtrate centrifuged at 11000 ×*g* for 20 min at 4°C. The supernatant was filtered through cheesecloth again, and an equal volume of 1:1 chloroform/1-butanol mixture was added and stirred on ice for 30 min. The mixture was centrifuged at 4500 ×*g* for 10 min. The supernatant was collected and the aqueous phase separated. To the aqueous phase was added NaCl to 0.2 M, 8% (w/w) PEG 8000, and 1% (w/w) Triton X-100 surfactant. The mixture was stirred on ice for 30 min and stored at 4 °C for 1 h. The solution was centrifuged at 22000 ×*g* for 15 min at 4 °C. The supernatant was discarded, and the pellet resuspended in 0.1 M pH 7.4 KP buffer at 4 °C overnight. The solution was carefully layered over a 40% (w/w) sucrose cushion and centrifuged at 160000 ×*g* for 2.5 h at 4 °C. The supernatant was discarded, and the pellet resuspended in 0.01 M pH 7.4 KP buffer overnight. The solution was portioned equally into microcentrifuge tubes and centrifuged at 15513 ×*g* for 15 min. The supernatant was collected as the final TMV solution. UV-

vis measurements were taken with NanoDrop at 260 nm (RNA) and 280 nm (protein). A ratio of A_{260}/A_{280} around 1.26 indicates intact TMV. Using the Beer-Lambert Law with ε = 3 as reported,[72] the solution concentration was determined.

2.4.12 - Desalting Procedure for Buffer Replacement

This protocol is used on any concentration of TMV stock to remove the buffer and replace it with 18.2 MΩ DI H_2O using a GE Health Care PD midi Trap G-25 column. The column was rinsed with 4 mL 18.2 MΩ DI H_2O four times before adding 1 mL of the virus solution. The initial void volume was then discarded. Another 1.5 mL of 18.2 MΩ DI H_2O was then added to the top of the column and this volume was collected as the desalted virus solution and its concentration was re-determined by NanoDrop.

2.4.13 - Preparation of Initial TMV@ZIF-8 Prototype

The initial prototype is denoted as TZ-P1. In a typical synthesis of TZ-P1, 41.7 µL of a 6 mg/mL desalted TMV solution (0.25 mg of TMV) was added into a microcentrifuge tube, followed by 500 µL of a 160 mM HMIM aqueous solution and 500 µL of a 40 mM $Zn(OAc)_2$ aqueous solution (HMIM:Zn= 4:1). The mixture was shaken for 20 s then set on the bench overnight. The whitish flocculates formed right after shaking. The flocculates were separated by centrifugation at 2656 ×*g* for 10 min. The product was washed by 18.2 MΩ DI H_2O twice.

2.4.14 - Preparation of TZ-thin

In a typical synthesis, 10.4 µL of a 6 mg/mL desalted TMV solution (0.0625 mg of TMV) was added into a microcentrifuge tube, followed by 500 µL of a 400 mM HMIM aqueous solution and 500 µL of a 20 mM $Zn(OAc)_2$ aqueous solution. The mixture was shaken for 20 s then set on the bench overnight to allow full crystal growth. The whitish flocculates formed right after shaking.

The flocculates were separated by centrifugation at 2656 ×*g* for 10 min. The product was washed by 18.2 MΩ DI H_2O twice.

2.4.15 - Preparation of TZ-thick

In a typical synthesis, 18.5 µL of a 6 mg/mL desalted TMV solution (0.111 mg of TMV) was added into a 20 mL glass scintillation vial, followed by 3000 µL of a 400 mM HMIM aqueous solution and 1500 µL of a 20 mM $Zn(OAc)_2$ aqueous solution. The mixture was shaken for 20 s then set on the bench overnight. The whitish flocculates formed right after shaking. The flocculates were separated by centrifugation at 2656 ×*g* for 10 min. The product was washed by 18.2 MΩ DI H_2O twice.

2.4.16 - General Exfoliation Procedure

The exfoliation solution was prepared by adding EDTA to 1 M to a 1 M aqueous KOH solution, adding KOH until the EDTA dissolved, and then adjusting the pH to 7.0 with HCl. The TMV@ZIF-8 suspension is centrifuged at 2656 ×*g* for 10 min and the supernatant carefully removed. 500 µL of the exfoliation solution is added, the TMV solution is vortexed for 30 s, and left to sit for 2 h. The solution is then desalted as described earlier.

2.4.17 - Synthesis of 2-azidoethanamine

2-azidoethanamine was synthesized as reported in the literature.[73] A 50 mL round bottom flask was charged with 10 mL of H_2O and 1.9172 g of sodium azide. 2.0633 g of 2-bromoethanamine hydrobromide was added and the reaction stirred at 80 °C for 24 h. The reaction mixture was cooled to 0 °C in an ice bath and 10 mL of diethyl ether and 3 g of solid KOH was added. The mixture was washed 3× with diethyl ether and the combined organic phases dried with $MgSO_4$,

filtered, the solvent evaporated under a stream of dry N_2, and transferred between vessels with DCM. 0.3691 g of the product was recovered as a viscous brown liquid (43% yield). ^{1}H-NMR ($CDCl_3$, 500 MHz, Figure 2.12) δ: 3.35 (t, J = 5.55, 2H) 2.86 (t, J = 5.60, 2H) 1.53 (s, 2H). ^{13}C-NMR ($CDCl_3$, 125 MHz, Figure 2.13) δ: 54.52, 41.25.

2.4.18 - Synthesis of fluorescein-azide

5-(3-(2-Azidoethyl)thioureido)-2-(6-hydroxy-3-oxo-3H-xanthen-9-yl)-benzoic acid [fluorescein-azide] was synthesized as reported in the literature[74]. A 25 mL round bottom flask was charged with 0.1523 g of FITC in 15 mL of methanol. 0.0738 g of 2-azidoethanamine and 500 µL of triethylamine was added, and the reaction stirred at room temperature overnight. The solvent was evaporated under vacuum and 0.0846 g of dark orange powder collected (46% yield). ^{1}H-NMR (CD_3OD, 500 MHz, Figure 2.14) δ: 7.99 (d, J = 1.95, 1H), 7.73 (dd, J = 8.15, J = 2.05, 1H), 7.21 (d, J = 8.15, 1H), 7.08 (d, J = 9.05, 2H), 6.65 (d, J = 2.20, 2H), 6.62 (dd, J = 9.08, J = 2.23, 2H), 3.84 (t, J = 5.90, 2H), 3.60 (t, J = 5.95, 2H). ^{13}C-NMR (DMSO-d6, 125 MHz, Figure 2.15) δ: 180.96, 168.62, 160.48, 152.20, 146.07, 141.31, 129.13, 127.39, 124.37, 116.90, 113.16, 109.98, 102.31, 49.44, 42.92.

2.4.19 - Preparation of interior-alkyne-TMV

2 mg of TMV (391 µL of 5.12 mg/mL in 0.01 M pH 7.4 KP buffer) was diluted to 774 µL with 0.1 M pH 7.4 HEPES buffer and thoroughly mixed in a small scintillation vial. To this solution was added 130 µL of 0.1 M propargylamine in 18.2 MΩ DI H_2O and 3.0 mg of HOBt. 32 µL of 0.1 M EDC in 18.2 MΩ DI H_2O was added at t=0 h to start the reaction, and again after t=6 h and

t=18 h. The vial was mixed gently until t=24 h. The TMV solution was passed through a pre-equilibrated GE Health Care PD midi Trap G-25 column with 0.01 M pH 7.4 KP buffer.

2.4.20 - Preparation of fTMV

Aminoguanidine bicarbonate was dissolved in conc. HCl and evaporated under vacuum to yield aminoguanidine hydrochloride. The interior-alkyne-TMV solution was concentrated in a Sartorius Vivaspin Turbo 15 centrifugal concentrator (M.W. cutoff = 10,000 Da) and then diluted to 770 µL with 0.01 M pH 7.4 KP buffer in a small scintillation vial. 190 µL of DMSO, and 10 µL of 0.01 M fluorescein-azide in DMSO were added to the solution and vortexed for 10 s. In a separate vial, 25 mg of $CuSO_4 \cdot 5H_2O$ and 220 mg THPTA were added to 1 mL of 18.2 MΩ DI H_2O, vortexed for 10 s, and left to sit for 5 min to allow the coordination complex to form. To the TMV solution was added 10 µL of the Cu-THPTA solution, 10 µL of 0.2 M aminoguanidine hydrochloride in 18.2 MΩ DI H_2O, and lastly, 10 µL of 0.2 M sodium ascorbate in 18.2 MΩ DI H_2O (which starts the click reaction). The virus solution was gently mixed for 2 h. 10 µL of 0.5 M EDTA in 18.2 MΩ DI H_2O (buffered to pH 8.0 with NaOH pellets) was added and the solution stirred for 10 min to remove the copper. The solution was passed through a pre-equilibrated GE Health Care PD midi Trap G-25 column with 0.01 M pH 7.4 KP buffer. The eluent was concentrated in a centrifugal concentrator and concentration determined by NanoDrop to be 0.994 mg/mL. Excitation/Emission spectra of fTMV is shown in Figure 2.16.

2.4.21 - Preparation of fTMV@ZIF-8

The fTMV@ZIF-8 was prepared by following the TZ-thin synthetic procedure (SI Section 3.3).

2.4.22 - Diazonium Coupling Reaction on Native TMV

Diazonium salt was prepared by mixing the following solutions at 0 °C for 1 h: 400 μL of an ice cold 0.3 M *p*-toluenesulfonic acid monohydrate solution, 75 μL of a 0.68 M 4-nitroaniline solution in acetonitrile, and 25 μL of a 3.0 M aqueous sodium nitrite solution. Next, 791 μL of 0.1 M pH 8.8 borate buffer was added to 171 μL of 11.71 mg/mL TMV solution on ice. To this mixture, 38 μL of the *in situ* formed diazonium salt (35 eq) was added and this reaction mixture was briefly vortexed, then placed in an ice bath for 30 min. The modified TMV sample was purified by passing through a GE Health Care PD midi Trap G-25 column. To determine the reaction efficiency, TMV coat proteins were characterized by ESI-MS (Figure 2.17) following a published procedure.[46] The coat proteins were isolated by adding two volumes of glacial acetic acid to the TMV solution and centrifuging at 14462 ×*g* for 10 min to remove any of the particles in the solution.

2.4.23 - Diazonium Coupling Reaction on TZ-thin and TZ-thick

Diazonium salt was prepared by mixing following solutions at 0 °C for 1 h: 400 μL of an ice cold 0.3 M *p*-toluenesulfonic acid monohydrate solution; 75 μL of 0.68 M 4-nitroaniline in acetonitrile; and 25 μL of 3.0 M aqueous sodium nitrite. Subsequently, TZ-thin or TZ-thick containing 1 mg of TMV was suspended in 18.2 MΩ DI H_2O. Diazonium salt (38 μL) was then added to the TMV@ZIF-8 suspension. The reaction mixture was briefly vortexed, then place in an ice bath for 30 min. Then TZ-thin or TZ-thick composite materials were separated from the reactants by centrifugation at 2656 ×*g* for 10 min followed by thoroughly washing with 18.2 MΩ DI H_2O. Modified TZ-thin or TZ-thick was characterized using ESI-MS (Figure 2.18 and 2.19). The coat proteins were isolated by adding two volumes of glacial acetic acid to the TMV solution and centrifuging at 14462 ×*g* for 10 min to remove any of the particles in the solution.

2.4.24 - Calibration Curve of fTMV

Fluorescence intensity readings were taken in a 96-well plate using 100 µL aliquots, 0.01 M pH 7.4 KP buffer as a blank, and aliquots of the base fTMV solution with dilution factors of 1×, 10×, 20×, 40×, 80×, 160×, 320×, 640×, 1280×, 2560×, and 5120× at 518 nm with excitation at 450 nm. The points were plotted and a linear best-fit line ($R^2 = 0.9964$) constructed to use as a calibration curve (Figure 2.20).

2.4.25 - Fluorescence of Supernatant

The fTMV@ZIF-8 was suspended in 1 mL of 18.2 MΩ DI H_2O. Because TMV@ZIF-8 forms a stable suspension in water and does not settle out of solution, it is necessary to gently centrifuge the sample to afford a headspace to extract an aliquot of the sample. These centrifuge speeds are incapable of sedimenting non-encapsulated TMV. After centrifugation, the sedimentation gradually returns to form a heterogeneous suspension again. Therefore, for each time point, the mixture was centrifuged at 4722 ×*g* for 10 min. 100 µL was carefully removed from the top of the supernatant, and put in a 96-well plate, with 100 µL of 18.2 MΩ DI H_2O as a blank, and fluorescence intensity recorded at 518 nm with excitation at 450 nm. The 100 µL supernatant aliquot was returned to the fTMV@ZIF-8 solution. The solution was centrifuged and a 100 µL aliquot measured and returned every hour for 10 h, and again at the 24 h time point.

2.4.26 - Exfoliation and Recovery of Fluorescence

After the 24 h stability test, the fTMV was released by treating the sample with exfoliation solution to dissolve the ZIF-8 over 2 h. The solution was again centrifuged at 4722 ×*g* for 10 min. A 100 µL aliquot was taken from the supernatant and its fluorescence intensity was measured in a 96-well plate against 100 µL of the exfoliation solution as a blank at 518 nm with excitation at 450

nm. If the detector was saturated, 50 µL of the supernatant aliquot was transferred to another well and diluted with 50 µL of exfoliation solution and re-measured. This was repeated until the detector was not saturated. In this case, a 4× dilution was required, and the intensity value correspondingly multiplied by 4 to get the original intensity.

2.4.27 - Stability Test for Organic Solvent Tolerance

In a microcentrifuge tube, the fresh product (TZ-thin or TZ-thick) was suspended in methanol after being properly washed with 18.2 MΩ DI H_2O and methanol. Then the product was centrifuged at 2656 ×*g* and washed with the desired organic solvent (DMF/acetonitrile/methanol/DCM) to remove water. The composite was then suspended in the organic solvent for 16 h. To confirm the integrity by SEM, an aliquot of the composite suspension (5 µL) was directly cast on a clean silicon chip and dried under ambient conditions, except the suspension in DMF, which needed to be re-suspended in methanol to facilitate drying process.

To determine the stability of the embedded virus particles in methanol, TZ-thick was soaked in methanol for 16 h. The solution was centrifuged at 2656 ×*g* for 10 min, and the supernatant carefully removed. The solids were treated with exfoliation solution to dissolve the ZIF-8 shell. The solution was then desalted as described earlier. Later, the integrity of virus was characterized by TEM with negative staining.

2.4.28 - Thermal Stability Test

In a microcentrifuge tube, TZ-thin or TZ-thick was suspended in 500 µL of 18.2 MΩ DI H_2O. A beaker of tap water was heated to 100 °C and allowed to boil. The microcentrifuge tubes were floated in the boiling water bath for 20 min. The sample was allowed to cool down to room

temperature on the bench and 5 μL of this suspension was added directly to a clean Si chip and characterized by SEM.

2.5 Appendix

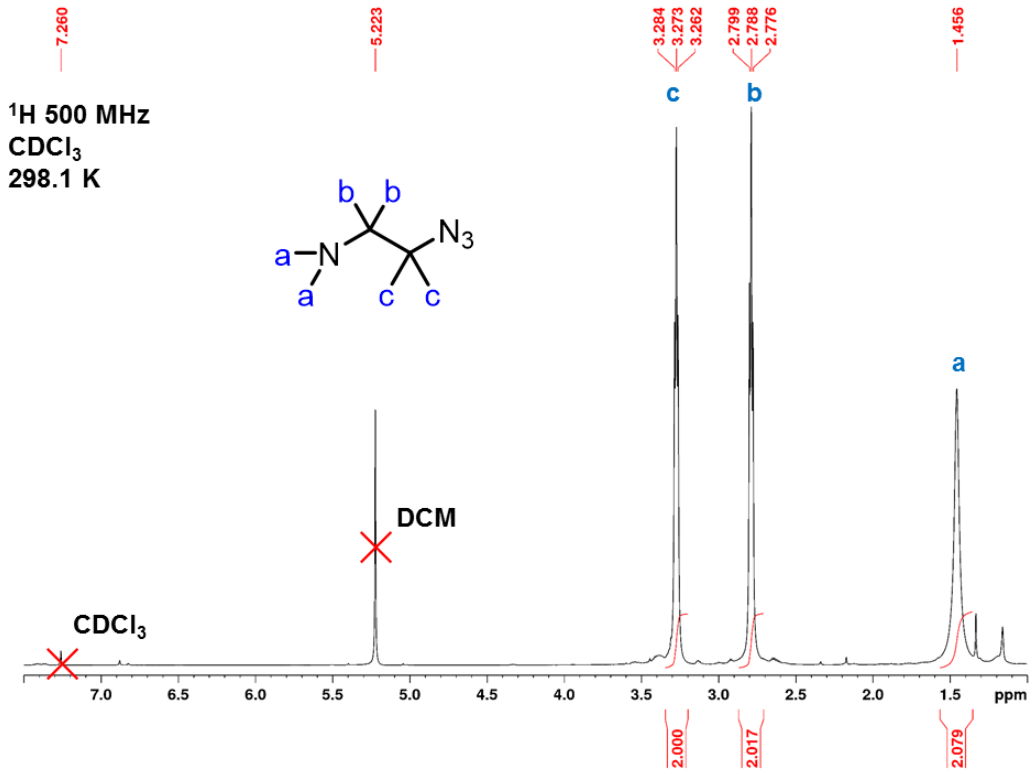

Figure 2.12. 1H NMR spectrum of 2-azidoethanamine in CDCl3 at 500 MHz, referenced to CDCl3.

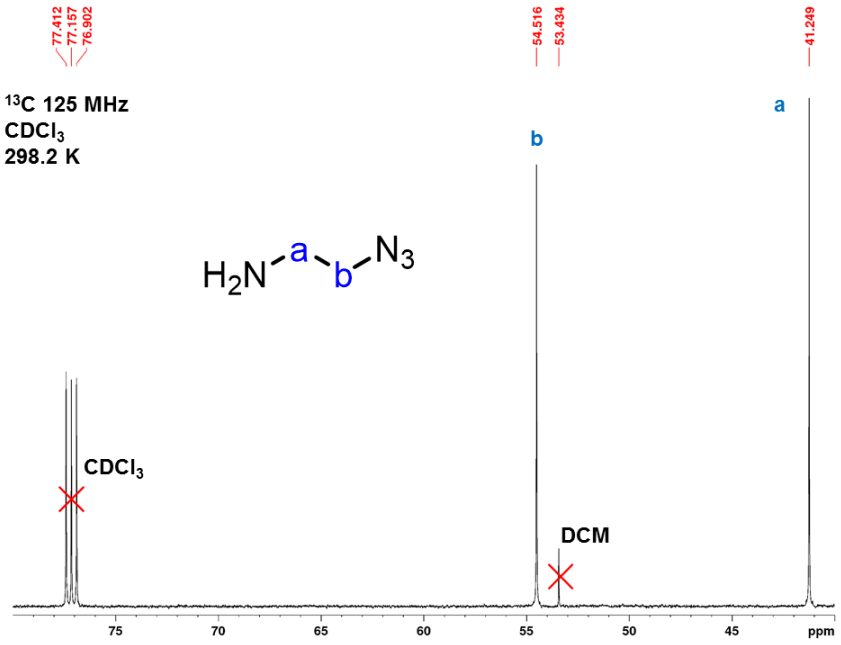

Figure 2.13. 13C NMR spectrum of 2-azidoethanamine in CDCl3 at 125 MHz, referenced to CDCl3.

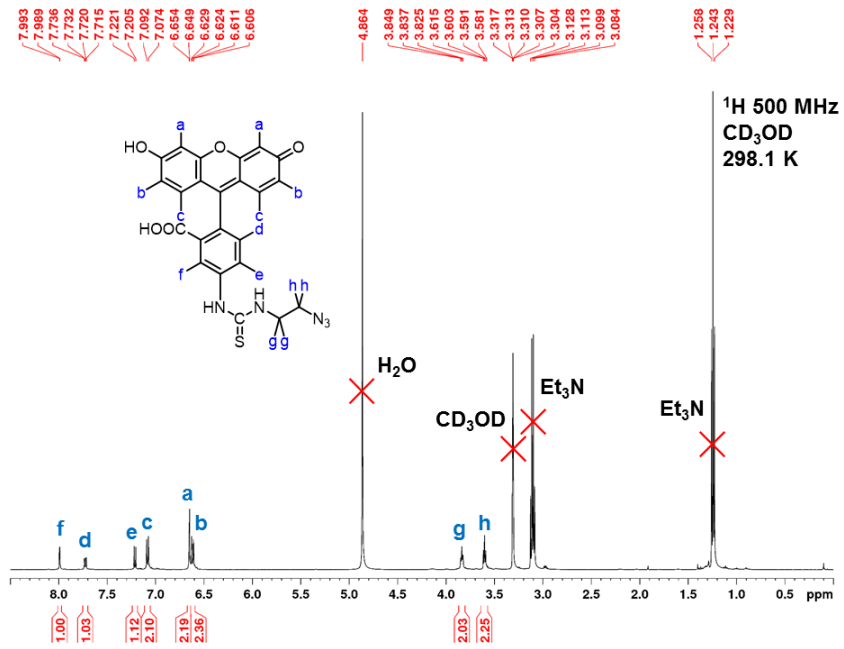

Figure 2.14. 1H NMR spectrum of fluorescein-azide in CD3OD at 500 MHz, referenced to CD3OD.

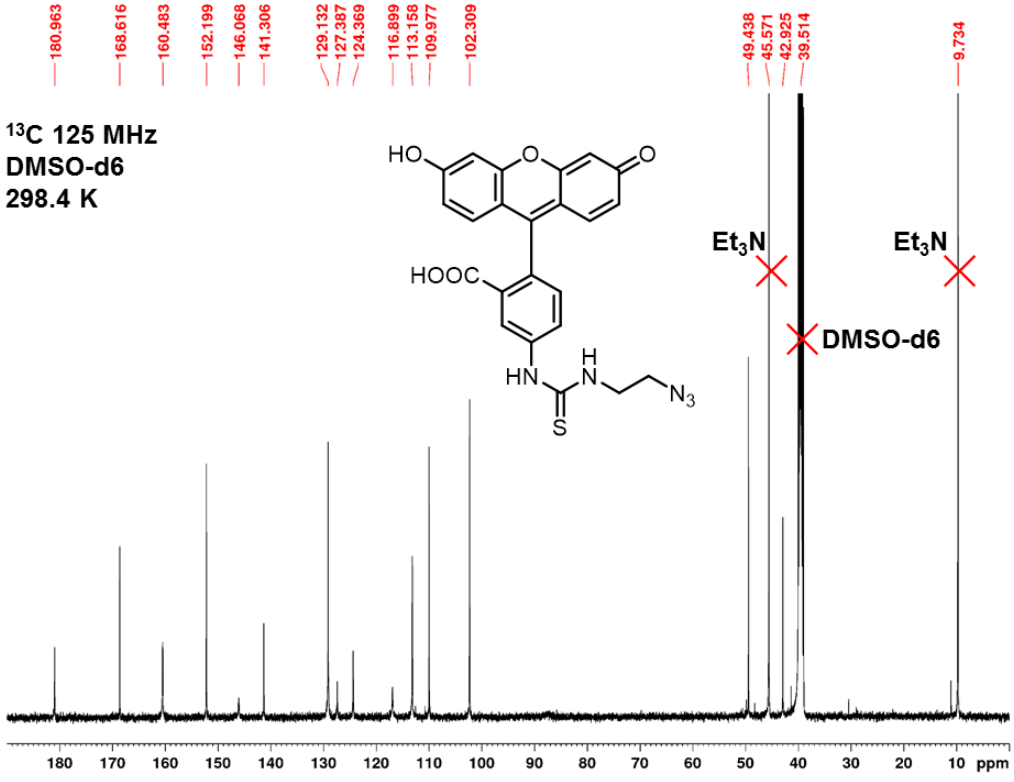

Figure 2.15. ^{13}C NMR spectrum of fluorescein-azide in DMSO-d_6 at 125 MHz, referenced to DMSO-d_6.

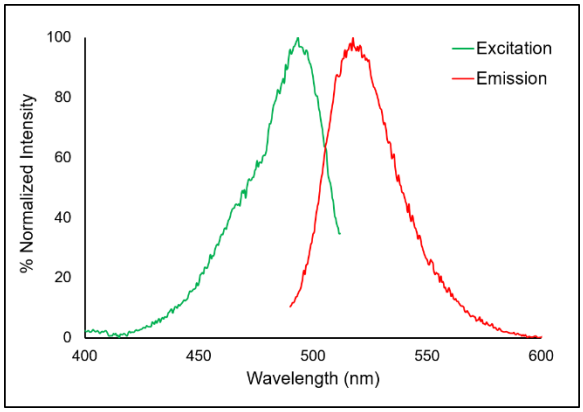

Figure 2.16. Excitation/Emission spectra of fTMV.

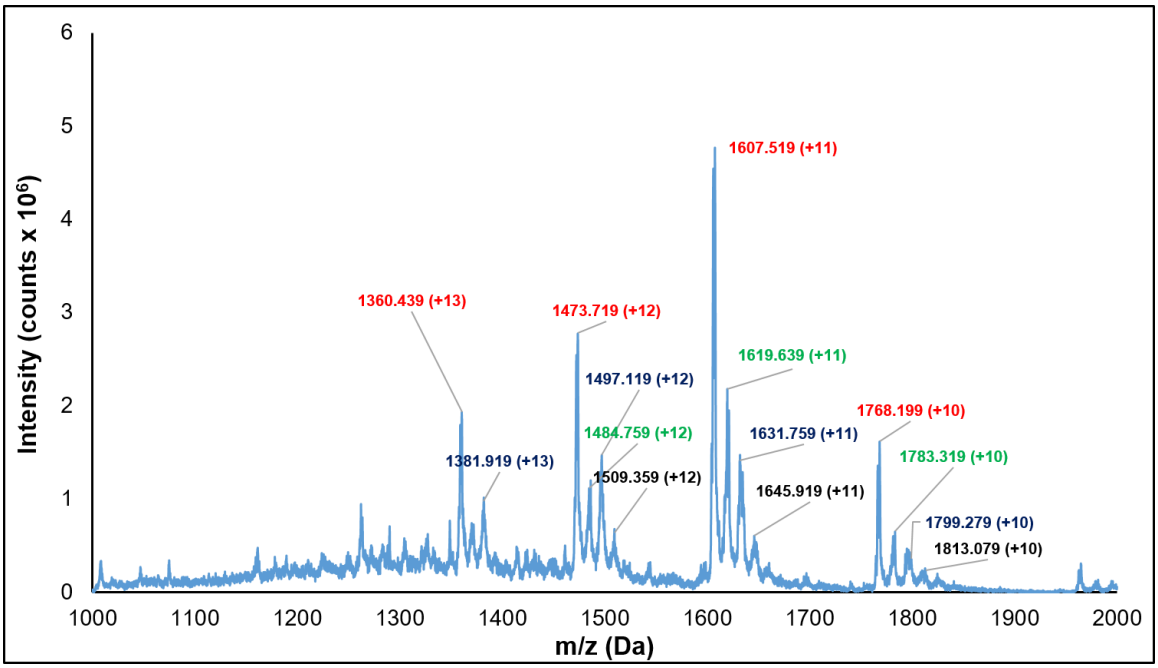

Figure 2.17. Raw non-deconvoluted ESI-MS spectrum of modified native TMV; all four tyrosine residues have been modified.

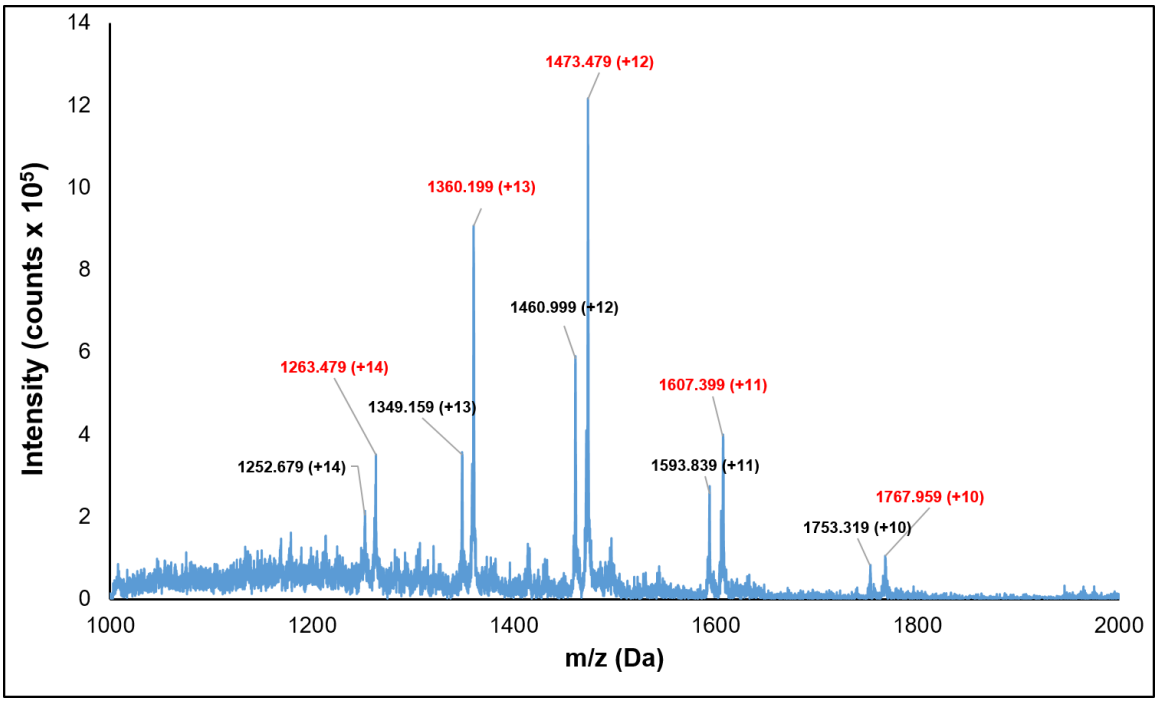

Figure 2.18. Raw non-deconvoluted ESI-MS spectrum of TZ-thin rods.

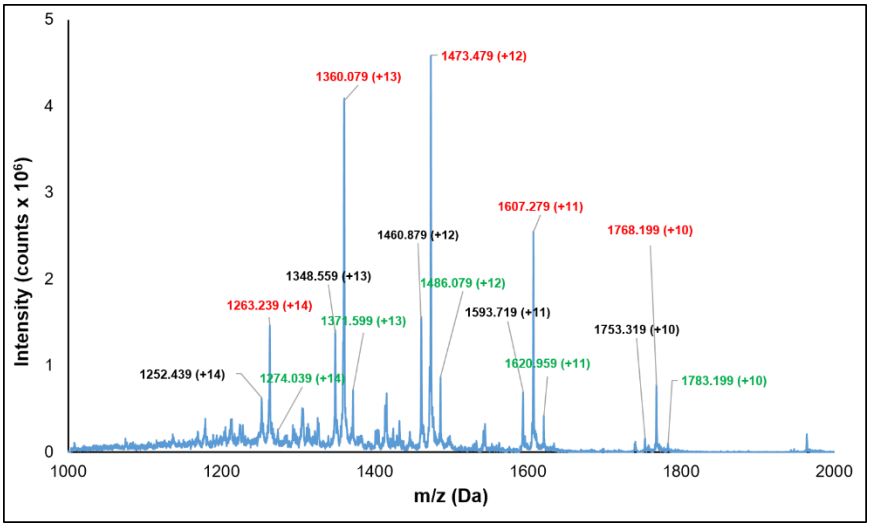

Figure 2.19. Raw non-deconvoluted ESI-MS spectrum of TZ-thick rods.

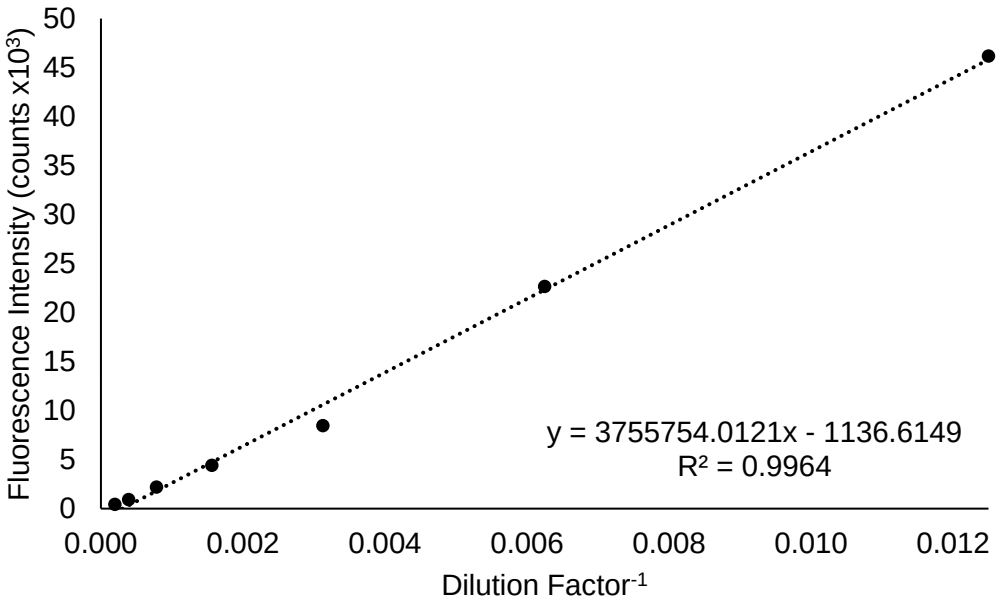

Figure 2.20. Calibration curve for fTMV. The dilutions of 1×, 10×, 20×, and 40× were not included on the line because the detector was saturated at these points.

2.6 References

1. Yaghi, O. M.; O'Keeffe, M.; Ockwig, N. W.; Chae, H. K.; Eddaoudi, M.; Kim, J. Reticular synthesis and the design of new materials. *Nature* **2003,** *423*, 705-714.

2. Furukawa, H.; Cordova, K. E.; O'Keeffe, M.; Yaghi, O. M., The Chemistry and Applications of Metal-Organic Frameworks. *Science* **2013,** *341*, 1230444.

3. Farha, O. K.; Özgür Yazaydın, A.; Eryazici, I.; Malliakas, C. D.; Hauser, B. G.; Kanatzidis, M. G.; Nguyen, S. T.; Snurr, R. Q.; Hupp, J. T. De novo synthesis of a metal–organic framework material featuring ultrahigh surface area and gas storage capacities. *Nat. Chem.* **2010,** *2*, 944-948.

4. Li, J.-R.; Zhou, H.-C. Bridging-ligand-substitution strategy for the preparation of metal–organic polyhedra. *Nat. Chem.* **2010,** *2*, 893-898.

5. Farha, O. K.; Eryazici, I.; Jeong, N. C.; Hauser, B. G.; Wilmer, C. E.; Sarjeant, A. A.; Snurr, R. Q.; Nguyen, S. T.; Yazaydın, A. Ö.; Hupp, J. T. Metal–Organic Framework Materials with Ultrahigh Surface Areas: Is the Sky the Limit? *J. Am. Chem. Soc.* **2012,** *134*, 15016-15021.

6. Farha, O. K.; Wilmer, C. E.; Eryazici, I.; Hauser, B. G.; Parilla, P. A.; O'Neill, K.; Sarjeant, A. A.; Nguyen, S. T.; Snurr, R. Q.; Hupp, J. T. Designing Higher Surface Area Metal–Organic Frameworks: Are Triple Bonds Better Than Phenyls? *J. Am. Chem. Soc.* **2012,** *134*, 9860-9863.

7. Marshall, R. J.; Griffin, S. L.; Wilson, C.; Forgan, R. S. Single-Crystal to Single-Crystal Mechanical Contraction of Metal–Organic Frameworks through Stereoselective Postsynthetic Bromination. *J. Am. Chem. Soc.* **2015,** *137*, 9527-9530.

8. Li, Q.; Zhang, W.; Miljanić, O. Š.; Sue, C.-H.; Zhao, Y.-L.; Liu, L.; Knobler, C. B.; Stoddart, J. F.; Yaghi, O. M. Docking in Metal-Organic Frameworks. *Science* **2009,** *325*, 855-859.

9. Peng, Y.; Krungleviciute, V.; Eryazici, I.; Hupp, J. T.; Farha, O. K.; Yildirim, T. Methane Storage in Metal–Organic Frameworks: Current Records, Surprise Findings, and Challenges. *J. Am. Chem. Soc.* **2013,** *135*, 11887-11894.

10. Gándara, F.; Furukawa, H.; Lee, S.; Yaghi, O. M. High Methane Storage Capacity in Aluminum Metal–Organic Frameworks. *J. Am. Chem. Soc.* **2014,** *136*, 5271-5274.

11. Lu, G.; Farha, O. K.; Zhang, W.; Huo, F.; Hupp, J. T. Engineering ZIF-8 Thin Films for Hybrid MOF-Based Devices. *Adv. Mater.* **2012,** *24*, 3970-3974.

12. He, C.; Lu, K.; Lin, W. Nanoscale Metal–Organic Frameworks for Real-Time Intracellular pH Sensing in Live Cells. *J. Am. Chem. Soc.* **2014,** *136*, 12253-12256.

13. Karagiaridi, O.; Lalonde, M. B.; Bury, W.; Sarjeant, A. A.; Farha, O. K.; Hupp, J. T. Opening ZIF-8: A Catalytically Active Zeolitic Imidazolate Framework of Sodalite Topology with Unsubstituted Linkers. *J. Am. Chem. Soc.* **2012,** *134*, 18790-18796.

14. Beyzavi, M. H.; Klet, R. C.; Tussupbayev, S.; Borycz, J.; Vermeulen, N. A.; Cramer, C. J.; Stoddart, J. F.; Hupp, J. T.; Farha, O. K. A Hafnium-Based Metal–Organic Framework as an Efficient and Multifunctional Catalyst for Facile CO_2 Fixation and Regioselective and Enantioretentive Epoxide Activation. *J. Am. Chem. Soc.* **2014,** *136*, 15861-15864.

15. Falkowski, J. M.; Sawano, T.; Zhang, T.; Tsun, G.; Chen, Y.; Lockard, J. V.; Lin, W. Privileged Phosphine-Based Metal–Organic Frameworks for Broad-Scope Asymmetric Catalysis. *J. Am. Chem. Soc.* **2014,** *136*, 5213-5216.

16. Mondloch, J. E.; Katz, M. J.; Isley Iii, W. C.; Ghosh, P.; Liao, P.; Bury, W.; Wagner, G. W.; Hall, M. G.; DeCoste, J. B.; Peterson, G. W.; Snurr, R. Q.; Cramer, C. J.; Hupp, J. T.; Farha, O. K. Destruction of chemical warfare agents using metal–organic frameworks. *Nat. Mater.* **2015,** *14*, 512-516.

17. Lee, C. Y.; Farha, O. K.; Hong, B. J.; Sarjeant, A. A.; Nguyen, S. T.; Hupp, J. T. Light-Harvesting Metal–Organic Frameworks (MOFs): Efficient Strut-to-Strut Energy Transfer in Bodipy and Porphyrin-Based MOFs. *J. Am. Chem. Soc.* **2011,** *133*, 15858-15861.

18. Son, H.-J.; Jin, S.; Patwardhan, S.; Wezenberg, S. J.; Jeong, N. C.; So, M.; Wilmer, C. E.; Sarjeant, A. A.; Schatz, G. C.; Snurr, R. Q.; Farha, O. K.; Wiederrecht, G. P.; Hupp, J. T. Light-Harvesting and Ultrafast Energy Migration in Porphyrin-Based Metal–Organic Frameworks. *J. Am. Chem. Soc.* **2013,** *135*, 862-869.

19. Choi, K. M.; Jeong, H. M.; Park, J. H.; Zhang, Y.-B.; Kang, J. K.; Yaghi, O. M. Supercapacitors of Nanocrystalline Metal–Organic Frameworks. *ACS Nano* **2014,** *8*, 7451-7457.

20. He, C.; Lu, K.; Liu, D.; Lin, W. Nanoscale Metal–Organic Frameworks for the Co-Delivery of Cisplatin and Pooled siRNAs to Enhance Therapeutic Efficacy in Drug-Resistant Ovarian Cancer Cells. *J. Am. Chem. Soc.* **2014,** *136*, 5181-5184.

21. Liu, D.; Poon, C.; Lu, K.; He, C.; Lin, W. Self-assembled nanoscale coordination polymers with trigger release properties for effective anticancer therapy. *Nat. Commun.* **2014,** *5*, 4182.

22. Lu, K.; He, C.; Lin, W. Nanoscale Metal–Organic Framework for Highly Effective Photodynamic Therapy of Resistant Head and Neck Cancer. *J. Am. Chem. Soc.* **2014,** *136*, 16712-16715.

23. Sindoro, M.; Yanai, N.; Jee, A.-Y.; Granick, S. Colloidal-Sized Metal–Organic Frameworks: Synthesis and Applications. *Acc. Chem. Res.* **2014,** *47*, 459-469.

24. Cho, W.; Lee, H. J.; Oh, M. Growth-Controlled Formation of Porous Coordination Polymer Particles. *J. Am. Chem. Soc.* **2008,** *130*, 16943-16946.

25. Tsuruoka, T.; Furukawa, S.; Takashima, Y.; Yoshida, K.; Isoda, S.; Kitagawa, S. Nanoporous Nanorods Fabricated by Coordination Modulation and Oriented Attachment Growth. *Angew. Chem., Int. Ed.* **2009,** *48*, 4739-4743.

26. Diring, S.; Furukawa, S.; Takashima, Y.; Tsuruoka, T.; Kitagawa, S. Controlled Multiscale Synthesis of Porous Coordination Polymer in Nano/Micro Regimes. *Chem. Mater.* **2010,** *22*, 4531-4538.

27. Cravillon, J.; Nayuk, R.; Springer, S.; Feldhoff, A.; Huber, K.; Wiebcke, M. Controlling Zeolitic Imidazolate Framework Nano- and Microcrystal Formation: Insight into Crystal Growth by Time-Resolved In Situ Static Light Scattering. *Chem. Mater.* **2011,** *23*, 2130-2141.

28. Umemura, A.; Diring, S.; Furukawa, S.; Uehara, H.; Tsuruoka, T.; Kitagawa, S. Morphology Design of Porous Coordination Polymer Crystals by Coordination Modulation. *J. Am. Chem. Soc.* **2011,** *133*, 15506-15513.

29. Kennedy, R. D.; Krungleviciute, V.; Clingerman, D. J.; Mondloch, J. E.; Peng, Y.; Wilmer, C. E.; Sarjeant, A. A.; Snurr, R. Q.; Hupp, J. T.; Yildirim, T.; Farha, O. K.; Mirkin, C. A. Carborane-Based Metal–Organic Framework with High Methane and Hydrogen Storage Capacities. *Chem. Mater.* **2013,** *25*, 3539-3543.

30. Hu, P.; Zhuang, J.; Chou, L.-Y.; Lee, H. K.; Ling, X. Y.; Chuang, Y.-C.; Tsung, C.-K. Surfactant-Directed Atomic to Mesoscale Alignment: Metal Nanocrystals Encased Individually in Single-Crystalline Porous Nanostructures. *J. Am. Chem. Soc.* **2014,** *136*, 10561-10564.

31. Na, K.; Choi, K. M.; Yaghi, O. M.; Somorjai, G. A. Metal Nanocrystals Embedded in Single Nanocrystals of MOFs Give Unusual Selectivity as Heterogeneous Catalysts. *Nano Lett.* **2014,** *14*, 5979-5983.

32. Zhang, W.; Wu, Z.-Y.; Jiang, H.-L.; Yu, S.-H. Nanowire-Directed Templating Synthesis of Metal–Organic Framework Nanofibers and Their Derived Porous Doped Carbon Nanofibers for Enhanced Electrocatalysis. *J. Am. Chem. Soc.* **2014,** *136*, 14385-14388.

33. Zhang, Z.; Chen, Y.; Xu, X.; Zhang, J.; Xiang, G.; He, W.; Wang, X. Well-Defined Metal–Organic Framework Hollow Nanocages. *Angew. Chem., Int. Ed.* **2014,** *53*, 429-433.

34. Zhao, M.; Deng, K.; He, L.; Liu, Y.; Li, G.; Zhao, H.; Tang, Z. Core–Shell Palladium Nanoparticle@Metal–Organic Frameworks as Multifunctional Catalysts for Cascade Reactions. *J. Am. Chem. Soc.* **2014,** *136*, 1738-1741.

35. Zhou, J.; Wang, P.; Wang, C.; Goh, Y. T.; Fang, Z.; Messersmith, P. B.; Duan, H. Versatile Core–Shell Nanoparticle@Metal–Organic Framework Nanohybrids: Exploiting Mussel-Inspired Polydopamine for Tailored Structural Integration. *ACS Nano* **2015,** *9*, 6951-6960.

36. Strable, E.; Prasuhn, D. E.; Udit, A. K.; Brown, S.; Link, A. J.; Ngo, J. T.; Lander, G.; Quispe, J.; Potter, C. S.; Carragher, B.; Tirrell, D. A.; Finn, M. G. Unnatural Amino Acid Incorporation into Virus-Like Particles. *Bioconjugate Chem.* **2008,** *19*, 866-875.

37. Schwarz, B.; Douglas, T. Development of virus-like particles for diagnostic and prophylactic biomedical applications. *Wiley Interdiscip. Rev. Nanomed. Nanobiotechnol.* **2015,** *7*, 722-735.

38. Zhao, X.; Lin, Y.; Wang, Q. Virus-based scaffolds for tissue engineering applications. *Wiley Interdiscip. Rev. Nanomed. Nanobiotechnol.* **2015,** *7*, 534-547.

39. Chen, Z.; Li, N.; Chen, L.; Lee, J.; Gassensmith, J. J. Dual Functionalized Bacteriophage Qβ as a Photocaged Drug Carrier. *Small* **2016**, *33*, 4563-4571.

40. Chen, Z.; Li, N.; Li, S.; Dharmarwardana, M.; Schlimme, A.; Gassensmith, J. J. Viral chemistry: the chemical functionalization of viral architectures to create new technology. *Wiley Interdiscip. Rev. Nanomed. Nanobiotechnol.* **2016,** *8*, 512-534.

41. Wen, A. M.; Infusino, M.; De Luca, A.; Kernan, D. L.; Czapar, A. E.; Strangi, G.; Steinmetz, N. F. Interface of Physics and Biology: Engineering Virus-Based Nanoparticles for Biophotonics. *Bioconjugate Chem.* **2015,** *26*, 51-62.

42. Ma, Y.-Z.; Miller, R. A.; Fleming, G. R.; Francis, M. B. Energy Transfer Dynamics in Light-Harvesting Assemblies Templated by the Tobacco Mosaic Virus Coat Protein. *J. Phys. Chem. B* **2008,** *112*, 6887-6892.

43. Miller, R. A.; Stephanopoulos, N.; McFarland, J. M.; Rosko, A. S.; Geissler, P. L.; Francis, M. B. Impact of Assembly State on the Defect Tolerance of TMV-Based Light Harvesting Arrays. *J. Am. Chem. Soc.* **2010,** *132*, 6068-6074.

44. Bruckman, M. A.; Hern, S.; Jiang, K.; Flask, C. A.; Yu, X.; Steinmetz, N. F. Tobacco mosaic virus rods and spheres as supramolecular high-relaxivity MRI contrast agents. *J. Mater. Chem. B* **2013,** *1*, 1482-1490.

45. Bruckman, M. A.; Randolph, L. N.; Gulati, N. M.; Stewart, P. L.; Steinmetz, N. F. Silica-coated Gd(DOTA)-loaded protein nanoparticles enable magnetic resonance imaging of macrophages. *J. Mater. Chem. B* **2015,** *3*, 7503-7510.

46. Schlick, T. L.; Ding, Z.; Kovacs, E. W.; Francis, M. B. Dual-Surface Modification of the Tobacco Mosaic Virus. *J. Am. Chem. Soc.* **2005,** *127*, 3718-3723.

47. Shenton, W.; Douglas, T.; Young, M.; Stubbs, G.; Mann, S. Inorganic–Organic Nanotube Composites from Template Mineralization of Tobacco Mosaic Virus. *Adv. Mater.* **1999,** *11*, 253-256.

48. Dujardin, E.; Peet, C.; Stubbs, G.; Culver, J. N.; Mann, S. Organization of Metallic Nanoparticles Using Tobacco Mosaic Virus Templates. *Nano Lett.* **2003,** *3*, 413-417.

49. Knez, M.; Sumser, M.; Bittner, A. M.; Wege, C.; Jeske, H.; Martin, T. P.; Kern, K. Spatially Selective Nucleation of Metal Clusters on the Tobacco Mosaic Virus. *Adv. Func. Mater.* **2004,** *14*, 116-124.

50. Niu, Z.; Liu, J.; Lee, L. A.; Bruckman, M. A.; Zhao, D.; Koley, G.; Wang, Q. Biological Templated Synthesis of Water-Soluble Conductive Polymeric Nanowires. *Nano Lett.* **2007,** *7*, 3729-3733.

51. Royston, E.; Ghosh, A.; Kofinas, P.; Harris, M. T.; Culver, J. N. Self-Assembly of Virus-Structured High Surface Area Nanomaterials and Their Application as Battery Electrodes. *Langmuir* **2008,** *24*, 906-912.

52. Pomerantseva, E.; Gerasopoulos, K.; Chen, X.; Rubloff, G.; Ghodssi, R. Electrochemical performance of the nanostructured biotemplated V_2O_5 cathode for lithium-ion batteries. *J. Power Sources* **2012,** *206*, 282-287.

53. Park, K. S.; Ni, Z.; Côté, A. P.; Choi, J. Y.; Huang, R.; Uribe-Romo, F. J.; Chae, H. K.; O'Keeffe, M.; Yaghi, O. M. Exceptional chemical and thermal stability of zeolitic imidazolate frameworks. *Proc. Natl. Acad. Sci. U. S. A.* **2006,** *103*, 10186-10191.

54. Chulkaivalsucharit, P.; Wu, X.; Ge, J. Synthesis of enzyme-embedded metal-organic framework nanocrystals in reverse micelles. *RSC Adv.* **2015,** *5*, 101293-101296.

55. Liang, K.; Ricco, R.; Doherty, C. M.; Styles, M. J.; Bell, S.; Kirby, N.; Mudie, S.; Haylock, D.; Hill, A. J.; Doonan, C. J.; Falcaro, P. Biomimetic mineralization of metal-organic frameworks as protective coatings for biomacromolecules. *Nat. Commun.* **2015,** *6*, 7240.

56. Wu, X.; Ge, J.; Yang, C.; Hou, M.; Liu, Z. Facile synthesis of multiple enzyme-containing metal-organic frameworks in a biomolecule-friendly environment. *Chem. Commun.* **2015,** *51*, 13408-13411.

57. Wu, X.; Yang, C.; Ge, J.; Liu, Z. Polydopamine tethered enzyme/metal-organic framework composites with high stability and reusability. *Nanoscale* **2015,** *7*, 18883-18886.

58. Liang, K.; Coghlan, C. J.; Bell, S. G.; Doonan, C.; Falcaro, P. Enzyme encapsulation in zeolitic imidazolate frameworks: a comparison between controlled co-precipitation and biomimetic mineralisation. *Chem. Commun.* **2016,** *52*, 473-476.

59. Lyu, F.; Zhang, Y.; Zare, R. N.; Ge, J.; Liu, Z. One-Pot Synthesis of Protein-Embedded Metal–Organic Frameworks with Enhanced Biological Activities. *Nano Lett.* **2014,** *14*, 5761-5765.

60. Shieh, F.-K.; Wang, S.-C.; Yen, C.-I.; Wu, C.-C.; Dutta, S.; Chou, L.-Y.; Morabito, J. V.; Hu, P.; Hsu, M.-H.; Wu, K. C. W.; Tsung, C.-K. Imparting Functionality to Biocatalysts via Embedding Enzymes into Nanoporous Materials by a de Novo Approach: Size-Selective Sheltering of Catalase in Metal–Organic Framework Microcrystals. *J. Am. Chem. Soc.* **2015,** *137*, 4276-4279.

61. The current result shows that these recrystallized particles are 200 to 300 nm in diameter, which is slightly shorter than the TMV@MOF rods that are mostly seen longer than 300 nm indicating that the virus particles are likely not encapsulated in the crystals. Further studies are underway to see if protein is incarcerated inside. We observed the morphological change of TZ-thin in DCM via SEM characterization. The micrographs indicate that within the first 40 min the rod-shape is retained; however, only polyhedral microcrystals are found after 3 h.

62. Lee, S.-Y.; Lim, J. S.; Culver, J. N.; Harris, M. T. Coagulation of tobacco mosaic virus in alcohol–water–LiCl solutions. *J. Colloid Interface Sci.* **2008,** *324*, 92-98.

63. Fairen-Jimenez, D.; Moggach, S. A.; Wharmby, M. T.; Wright, P. A.; Parsons, S.; Düren, T. Opening the Gate: Framework Flexibility in ZIF-8 Explored by Experiments and Simulations. *J. Am. Chem. Soc.* **2011,** *133*, 8900-8902.

64. Zhang, K.; Lively, R. P.; Zhang, C.; Chance, R. R.; Koros, W. J.; Sholl, D. S.; Nair, S. Exploring the Framework Hydrophobicity and Flexibility of ZIF-8: From Biofuel Recovery to Hydrocarbon Separations. *J. Phys. Chem. Lett.* **2013,** *4*, 3618-3622.

65. Zhang, L.; Hu, Z.; Jiang, J. Sorption-Induced Structural Transition of Zeolitic Imidazolate Framework-8: A Hybrid Molecular Simulation Study. *J. Am. Chem. Soc.* **2013,** *135*, 3722-3728.

66. Kolokolov, D. I.; Diestel, L.; Caro, J.; Freude, D.; Stepanov, A. G. Rotational and Translational Motion of Benzene in ZIF-8 Studied by 2H NMR: Estimation of Microscopic Self-Diffusivity and Its Comparison with Macroscopic Measurements. *J. Phys. Chem. C* **2014,** *118*, 12873-12879.

67. Tanaka, H.; Ohsaki, S.; Hiraide, S.; Yamamoto, D.; Watanabe, S.; Miyahara, M. T. Adsorption-Induced Structural Transition of ZIF-8: A Combined Experimental and Simulation Study. *J. Phys. Chem. C* **2014,** *118*, 8445-8454.

68. Zhang, L.; Wu, G.; Jiang, J. Adsorption and Diffusion of CO_2 and CH_4 in Zeolitic Imidazolate Framework-8: Effect of Structural Flexibility. *J. Phys. Chem. C* **2014,** *118*, 8788-8794.

69. Kolokolov, D. I.; Stepanov, A. G.; Jobic, H. Mobility of the 2-Methylimidazolate Linkers in ZIF-8 Probed by 2H NMR: Saloon Doors for the Guests. *J. Phys. Chem. C* **2015,** *119*, 27512-27520.

70. Bruckman, M. A.; Steinmetz, N. F. Chemical Modification of the Inner and Outer Surfaces of Tobacco Mosaic Virus (TMV). In *Virus Hybrids as Nanomaterials: Methods and Protocols*, Lin, B.; Ratna, B., Eds. Humana Press: Totowa, NJ, 2014; pp 173-185.

71. Our current hypothesis on this difference in yield is that the thick MOF shell contains better crystallinity comparing to the thin shell; thus, the thick ZIF shell possesses a higher order of periodicity of the pore structure, which could facilitate the transportation of small molecules.

72. Bruckman, M. A.; Steinmetz, N. F. Chemical Modification of the Inner and Outer Surfaces of Tobacco Mosaic Virus (TMV). In *Virus Hybrids as Nanomaterials: Methods and Protocols*, Lin, B.; Ratna, B., Eds. Humana Press: Totowa, NJ, 2014; pp 173-185.

73. Wang, T.; Wu, Y.; Kuan, S. L.; Dumele, O.; Lamla, M.; Ng, D. Y. W.; Arzt, M.; Thomas, J.; Mueller , J. O.; Barner-Kowollik , C.; Weil, T. A Disulfide Intercalator Toolbox for the Site-Directed Modification of Polypeptides. *Chem. - Eur. J.* **2015,** *21*, 228-238.

74. Gnaccarini, C.; Ben-Tahar, W.; Mulani, A.; Roy, I.; Lubell, W. D.; Pelletier, J. N.; Keillor, J. W. Site-specific protein propargylation using tissue transglutaminase. *Org. Biomol. Chem.* **2012,** *10*, 5258-5265.

CHAPTER 3

INVESTIGATION OF CONTROLLED GROWTH OF METAL ORGANIC FRAMEWORKS ON ANISOTROPIC VIRUS PARTICLES

Authors - Shaobo Li, Madushani Dharmarwardana, Raymond P. Welch, Candace E. Benjamin, Alexandra Shamir, Steven O. Nielsen, and Jeremiah J. Gassensmith

The Department of Chemistry and Biochemistry, BE26

The University of Texas at Dallas

800 West Campbell Road

Richardson, Texas, 75080-3021

Reprinted with permission from Li, S.; Dharmarwardana, M.; Welch, R. P.; Benjamin, C. E.; Shamir, A. M.; Nielsen, S. O.; Gassensmith, J. J. Investigation of Controlled Growth of Metal Organic Frameworks on Anisotropic Virus Particles. *ACS Appl. Mater. & Interfaces*, **2018**, *10*, 18161-18169. https://pubs.acs.org/doi/10.1021/acsami.8b01369.

3.1 Introduction

The *in-situ* crystallization of metal-organic frameworks (MOFs) on biological macromolecules, otherwise called bio-mimetic mineralization of MOFs, has emerged in recent years as a promising strategy to offer robust protection to encapsulated biological materials against environmental stresses.[1-7] MOFs are a family of porous crystalline materials constructed of metal nodes linked by organic ligands to form porous and high surface area crystals.[8-10] The tunable pore sizes and distribution confers potentially valuable properties in mass transfer, storage, sensing, and catalysis.[11-22] Among the previously reported MOF candidates for biomimetic mineralization, zeolitic imidazolate frameworks (ZIFs)[9]—in particular ZIF-8 with its constituent organic ligand being 2-methylimidazole (HMIM)—has shown tremendous flexibility in the syntheses on a broad variety of biological templates from enzymes,[23-38] to viruses,[3] to living yeast cells.[39-40] The ubiquity of ZIF-8 in biomimetic mineralization is owed, at least partially, to its hydrolytic and thermal stability and being readily prepared in pure aqueous solutions under ambient conditions. The resulting enzyme and viral composites[3, 26] demonstrate enhanced stability toward organic solvents and even boiling water. In addition to affording stability, the ZIF-8 shell allows reactants to travel through the pores and undergo catalysis by the inlaid enzyme under conditions normally leading to protein denaturation or to modify the surface of the protein in a bioconjugation reaction. This has excited researchers as it presents unique opportunities to make enzymes function even under extreme environmental conditions.[41-44]

A curious difference in the resulting morphology of the biomimetic mineralization process emerges using ZIF-8 at the size and length scale of viral nanoparticles. As illustrated in Figure 3.1, a single 300 × 18 nm tobacco mosaic virus (TMV),[45-48] forms an exoskeleton of very fine ZIF-8

crystals, which creates a core-shell bionanoparticle (CSBN). In contrast, many enzymes, which are typically < 10 nm, become entrapped in a single crystal that retains the micron-sized rhombic dodecahedral (r.d.) morphology of pristine ZIF-8. The fact that CSBNs retain the underlying morphology of the virus following their biomimetic mineralization process is intriguing as it is not clear why TMV should form CSBNs and not end up trapped in larger regular crystals *en masse*, as illustrated in Figure 3.1 d. Nevertheless, CSBNs offer an approach to the articulated interest[49-51] of combining mesoscale and microscale pore structure in the formation of MOF films and composites. One means of getting to such structures is via exploitation of recent advances in viral nanotechnology.[52-53] In particular, TMV can be engineered to create proteinaceous nanoparticles of custom lengths and very specific shapes like nano-stars, short nanorods and nanospheres.[54-56] This makes TMV an ideal model biological template to study the biomimetic mineralization of ZIF-8, the understanding of which could guide the fabrication of biology@MOF composite materials as drug carriers, biosensors, and biocatalysts.

In this manuscript, we report progress toward mechanistically understand the process that produces CSBNs. We have found that the concentrations and relative ratios of the starting reactants are vital parameters in the crystallization processes and they control the (i) phases[57] of the formed metal coordination polymer (ii) product morphology and (iii) nucleation of ZIF-8 in either a bio-catalyzed process or a spontaneous process. The bio-catalyzed crystallization can be described as crystal growth that is triggered by the protein surface of TMV. Spontaneous crystallization, for the purposes of this paper, is defined as the sudden nucleation and growth of ZIF-8 in water free of protein—essentially the product of mixing Zn and HMIM into water.

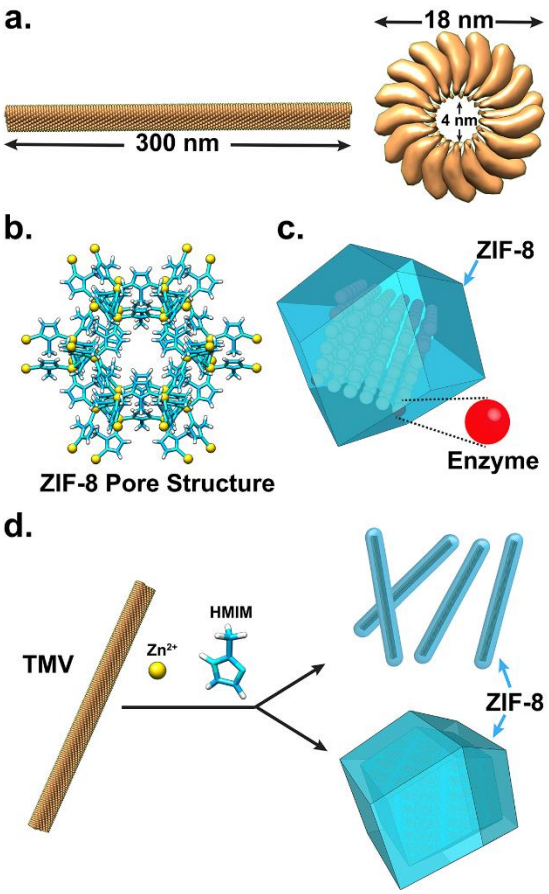

Figure 3.1. a) Model of TMV that shows a 300-nm long tube-shaped virus with an 18-nm diameter and a 4-nm inner channel; b) the pore structure of ZIF-8 assembled from Zn and MIM; c) schematic representation of reported enzyme@ZIF-8, which shows enzymes distributed within a r.d. ZIF-8 crystal; d) schematic illustration of TMV-templated ZIF-8 mineralization which will yield CSBNs (top) or r.d. composites (bottom), depending on the applied synthetic conditions.

By applying a series of systematically designed preparation conditions, we discovered that the resultant morphology and crystallinity of the products are produced in an evolving pattern, which is achieved by altering the ligand to metal molar ratio (L/M ratio) and precursor concentrations. Notably, a trend emerged that shows the formation of CSBNs are most favored in reaction conditions in which the spontaneous formation of ZIF-8 is otherwise disfavored. Finally, we investigated the role of TMV-Zn interaction in the formation of TMV@ZIF-8 composites by

adopting well-developed bioconjugation strategies, fluorescence spectroscopy, and isothermal titration calorimetry (ITC) techniques to create a more comprehensive explanation as to why CSBNs form under conditions that disfavor the so-called spontaneous crystallization of ZIF-8.

3.2 Results & Discussion

I. The Impact of Synthetic Conditions

The influence of metal and ligand concentrations and their relative molar ratios as experimental factors that dictate the final size, shape, and crystallinity of the as-synthesized ZIF-8 products has been known for some time. For instance, in 2011, Lai *et al.* [58] reported the synthesis of nanometer-sized ZIF-8 in water using a concentrated zinc nitrate aqueous precursor solution (500 mM) and a HMIM aqueous precursor solution (3500 mM) with a L/M ratio of 70. Subsequently in 2015, a comprehensive study by Zhang *et al.* [59] convincingly demonstrated that the concentration of zinc precursor, and the L/M ratios had a profound impact on the resultant shape, size, and crystallinity of ZIF-8 crystals. Similarly, in our previous study of TMV@ZIF-8 CSBN synthesis,[11] we briefly discussed that a higher L/M ratio could effectively improve phase purity of the as-prepared CSBNs, leading to robust stability against denaturing conditions. Inspired by these works, we sought to explore the relationship between metal and ligand precursor solutions to yield generalizable rules for the relationship between synthetic conditions and morphology of TMV@ZIF-8 CSBNs. In general, all the preparations of TMV-involved biomimetic mineralization of ZIF-8 were conducted as follows: TMV of a fixed quantity (1.6 pmol) was added into a microcentrifuge tube, followed by an aliquot of ligand precursor (HMIM) solution and an aliquot of metal precursor (zinc acetate) solution of the same volume. The reaction mixture was placed under ambient conditions without agitation overnight. The resulting flocculates were centrifuged at 2656 ×*g* and the as-formed

composites were washed by ultrapure water twice. We investigated the metal precursor concentration from 5 mM to 80 mM, and the L/M ratio from 2 to 80, which was altered simply by using ligand precursor solutions at varied concentrations, as the volumes of precursor solutions were always equal.

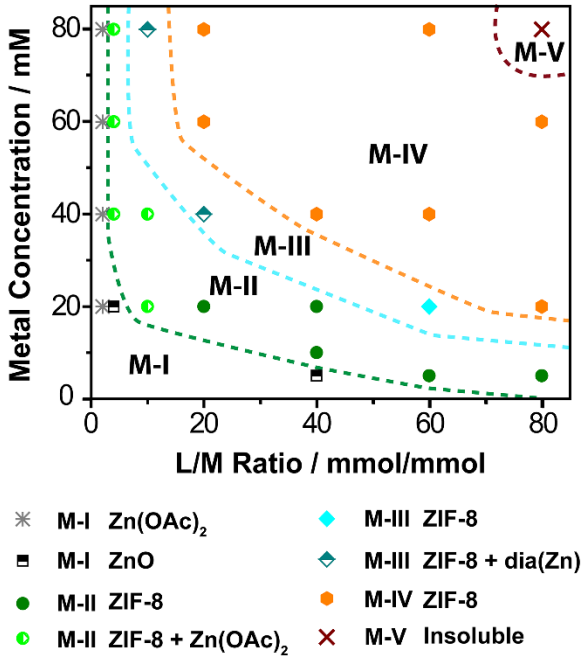

Figure 3.2. Composite Transformation Map, which correlates the SEM and PXRD characterizations of the as-obtained composites to their synthetic conditions. M-I represents non-ZIF-8 composites that are either strips of $Zn(OAc)_2$ (✳) or nearly aggregates of ZnO (▬); M-II represents rod-like CSBNs of either phase pure ZIF-8 (●) or a mixture of ZIF-8 and $Zn(OAc)_2$ (◔); M-III represents an intermediate mixture of composites with pure ZIF-8 phase CSBNs and r.d. crystals (◆), or a mixture of ZIF-8 and dia(Zn) of both CSBNs and r.d. crystals (◈); M-IV represents r.d. composites with pure ZIF-8 phase (⬢) and M-V (✕) is a region on the map where solubility issues of HMIM limit further study.

The products were analyzed via scanning electron microscopy (SEM) and powder X-ray diffraction (PXRD) and several surprises emerged from this exercise. Firstly, rod-like CSBNs were not the exclusive product of TMV-templated ZIF-8 mineralization; we were able to identify three other reaction products, which we categorized below. Moreover, we found that the characteristics

of the resultant composites can be readily grouped by the changes in L/M ratio and metal precursor concentration, which is concisely presented in a composite transfor transformation map in Figure 3.2. Through M-I to M-IV on the map, the applied reaction conditions were tuned to increasingly favor spontaneous crystallization of ZIF-8. Briefly, these "M" regions of the graph correspond to product morphology differences with M-II having rods, M-III having a mixture of both rods and r.d. crystals and M-IV showing exclusively r.d. crystals. The M-I region represents conditions that are incapable of forming ZIF-8 crystals, which is in good agreement with previously reported results.[83] The main products in this region are either micron-sized strips of zinc acetate composites[60] or poorly diffracting zinc oxide composites[61] (Figure 3.3 and 3.4). Lastly, the M-V region was drawn to indicate unachievable experimental conditions owing to solubility issues with ligand at such high concentrations.

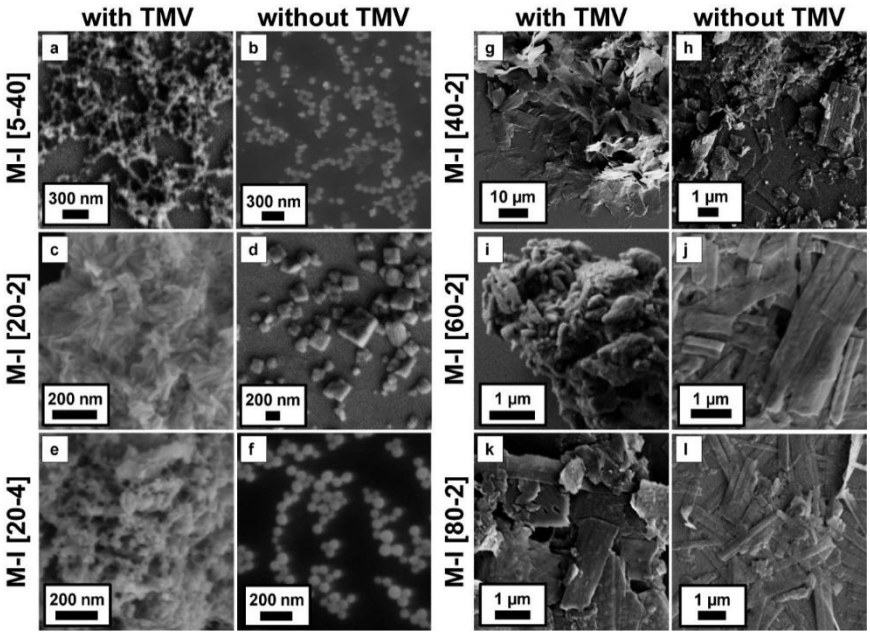

Figure 3.3. SEM micrographs of resultant products obtained at varied metal concentration and L/M ratios from the M-I region of the Composite Transformation Map. a), c), e), g), i) and k), samples that were prepared with 1.6 pmol TMV; b), d), f), h), j) and l), samples that were prepared without TMV.

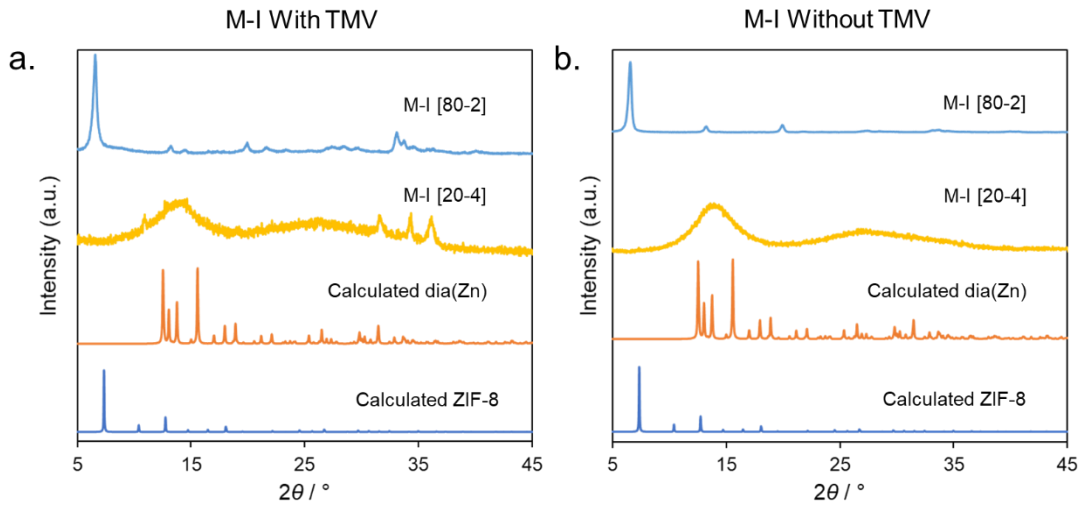

Figure 3.4. Representative PXRD patterns of resultant products obtained at varied metal concentration and L/M ratios from the M-I region; a) samples were prepared with 1.6 pmol TMV and b) samples were prepared without TMV.

Typical results obtained under synthetic conditions in the regions M-II, M-III, and M-IV are shown in Figures 3.5 and 3.6. To aid the discussion, we have adopted the nomenclature M-(morphology number) [metal concentration - L/M ratio]. In these figures, the concentration of metal precursor is fixed at 20 mM and the L/M ratio is increased moving down the figure. In each case, the product was pelleted via centrifugation without further washing or activation in order to analyze the as-synthesized bulk material. We further repeated the experiment without the presence of TMV to illustrate the products obtained via spontaneous crystallization, which are denoted as "without TMV." From these initial tests, it is clear that while larger micron sized r.d. crystals could form in the presence of TMV, they could also form in the TMV-free solutions. On the other hand, when CSBNs formed with the presence of TMV, only amorphous granules formed in TMV-free solutions. These results left us with the initial impression that conditions that favor r.d. crystals of ZIF-8 disfavor the formation of CSBNs. Upon closer examination, these impressions were incomplete—the situation is slightly more complex, as detailed below.

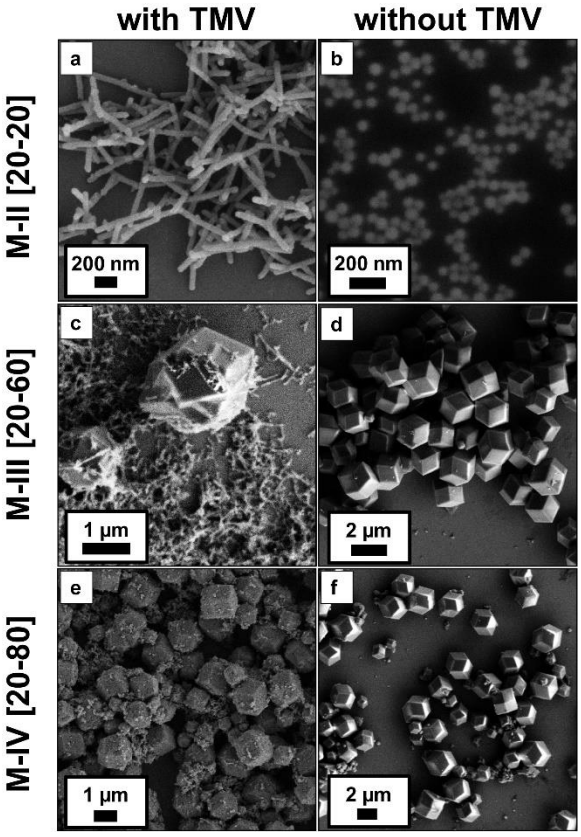

Figure 3.5. SEM characterization of resultant morphologies that are formed at constant metal (20 mM) concentration but with different L/M ratios. a), c) and e), samples that were prepared with 1.6 pmol TMV; b), d) and f), samples that were prepared without TMV.

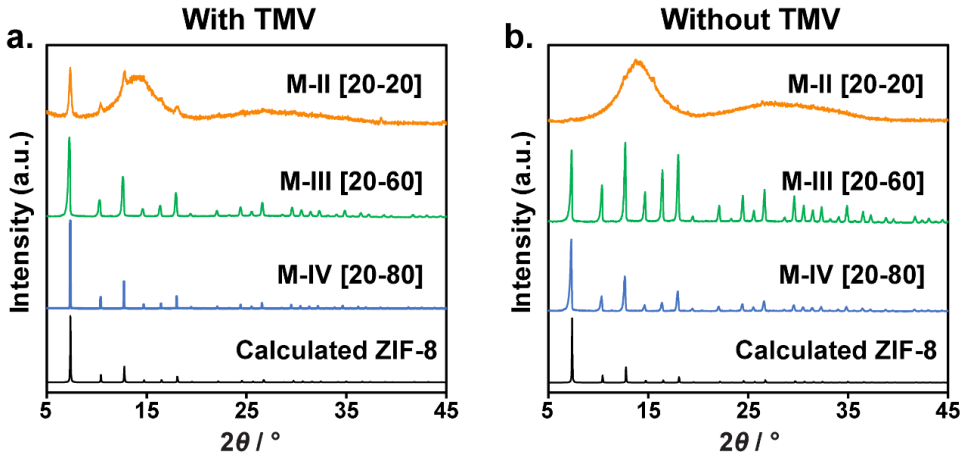

Figure 3.6. PXRD of resultant products from Figure 3.5. a) samples that were prepared in the presence of 1.6 pmol TMV and b) samples that were prepared without TMV.

M-II: CSBN Composites

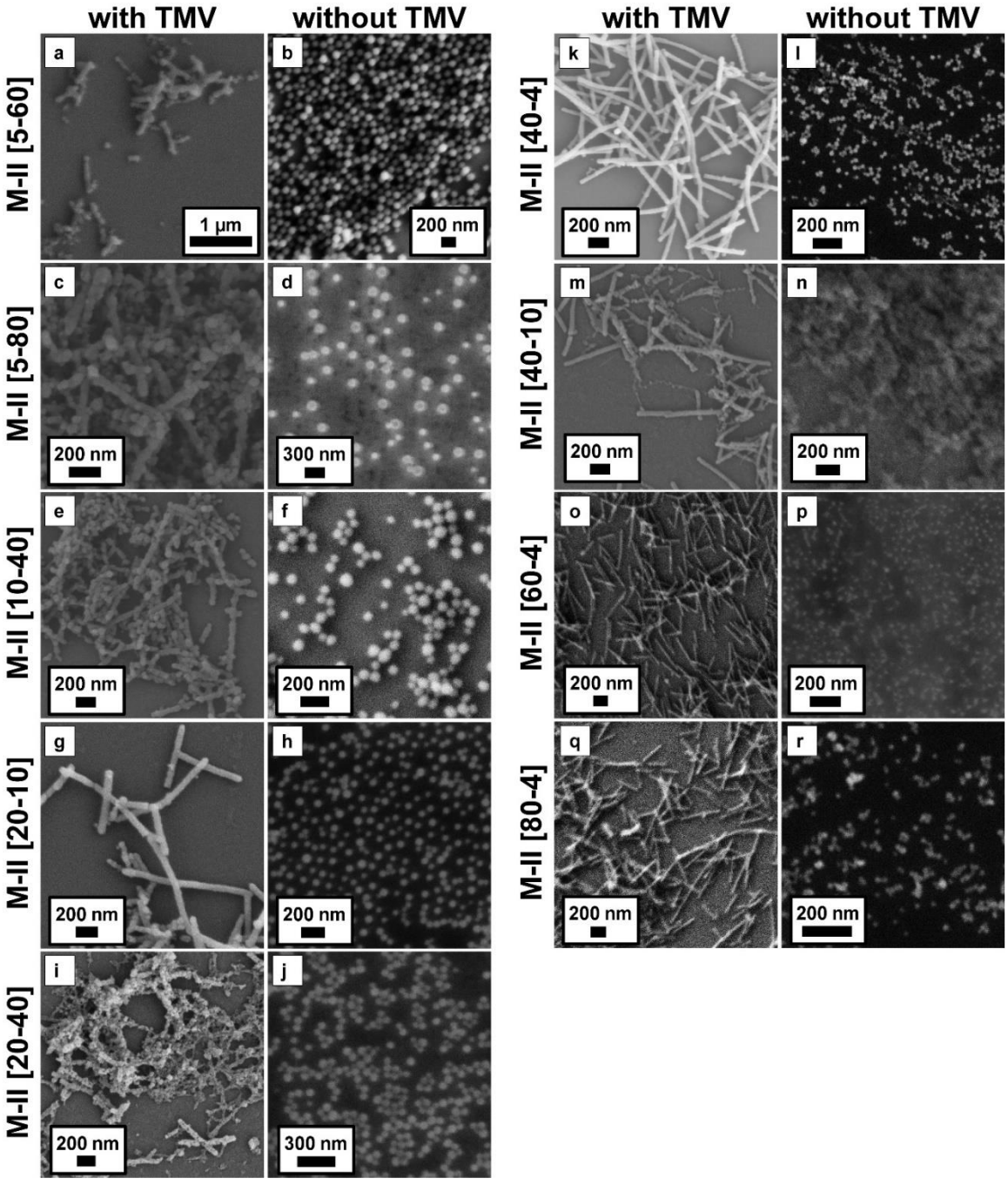

Figure 3.7. SEM micrographs of resultant products obtained at varied metal concentration and L/M ratios from the M-II region of the Composite Transformation Map. a), c), e), g), i), k), m), o) and q), samples that were prepared with 1.6 pmol TMV; b), d), f), h), j), l), n), p) and r), samples that were prepared without TMV.

While all M-II conditions produce rod-like CSBNs with a diameter ranging from 50 to 70 nm (Figure 3.5 a and 3.7) in some cases the rods are slightly ill-shaped (Figure 3.7 a and i) and the diffraction pattern of as-synthesized composites contain impurities. In some cases, these impurities are transient kinetic products. For instance, CSBNs obtained from the M-II [20-20] preparation (Figure 3.5 a and 3.6 a) show sharp reflections that align well with the calculated ZIF-8 diffraction peaks in addition to a broad peak at 14°, which is very nearly identical to that of the amorphous granules—a coordination polymer, which we now believe to be the kinetic product—that are produced in the absence of TMV (Figure 3.5 b and 3.6 b).

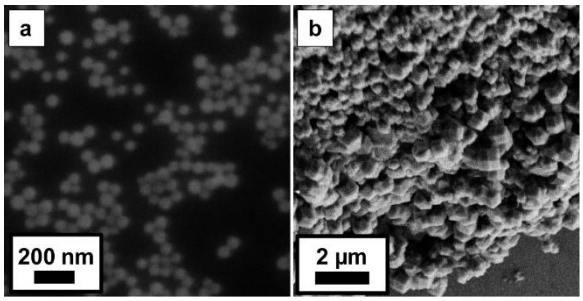

Figure 3.8. SEM micrographs of a) freshly prepared P-II [20-20] amorphous granules and b) P-II [20-20] amorphous granules after immersion in methanol at ambient conditions for 12 days.

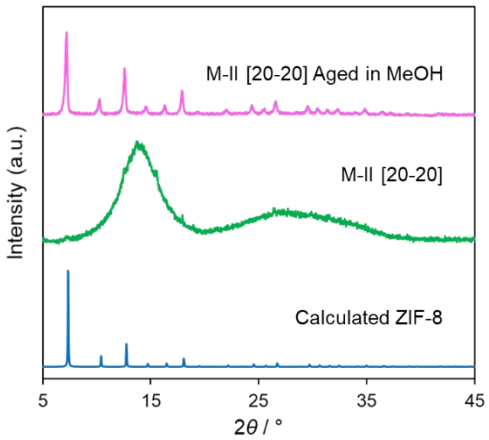

Figure 3.9. PXRD patterns of freshly prepared P-II [20-20] amorphous granules and P-II [20-20] amorphous granules after immersion in methanol at ambient conditions for 12 days.

When these amorphous granules are incubated in methanol, they ripen to the thermodynami thermodynamically favored ZIF-8 (Figure 3.8 and 3.9) and so we are able to produce phase-pure CSBNs simply by activating the ZIF-8 in methanol (*vide infra*). This finding is consistent with the previously reported observation and characterization of amorphous nanoclusters at the early stage of ZIF-8 crystallization.[62-63] On the other hand, preparations with lower L/M ratios (M-II [20-10] and M-II [40-4]) also contain ZIF-8 and amorphous phases, however, two sharp reflections at 11.1° and 19.0° that are attributed to zinc acetate (Figure 3.10 a) were observed. Generally, we have found that CSBNs which contain these impurities degrade rapidly in pure water and their shell is not stable.[3] Consequently, morphology alone is an inadequate predictor of stability.

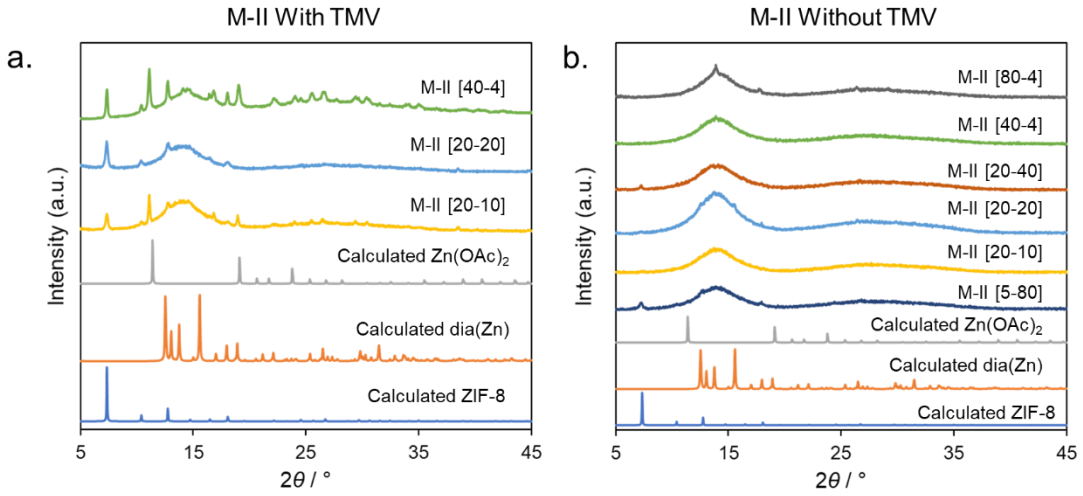

Figure 3.10. Representative PXRD patterns of resultant products obtained at varied metal concentration and L/M ratios from the M-II region; a) samples were prepared with 1.6 pmol TMV and b) samples were prepared without TMV.

For the M-II region in particular, we found incredible dissimilarity between the TMV-templated crystallization and the spontaneous crystallization (denoted as without TMV). That is, all the tested TMV-free M-II conditions produce amorphous granules with a broad peak at 14°—occasionally with trace quantities of ZIF-8 (Figure 3.10 b)—however, with the presence of TMV, nanometers-

thick crystalline shells, rather than amorphous granules, form on the exterior of TMV nanoparticles, with the crystallinity dependent on synthetic conditions.

M-III: Mixed Morphology Composites

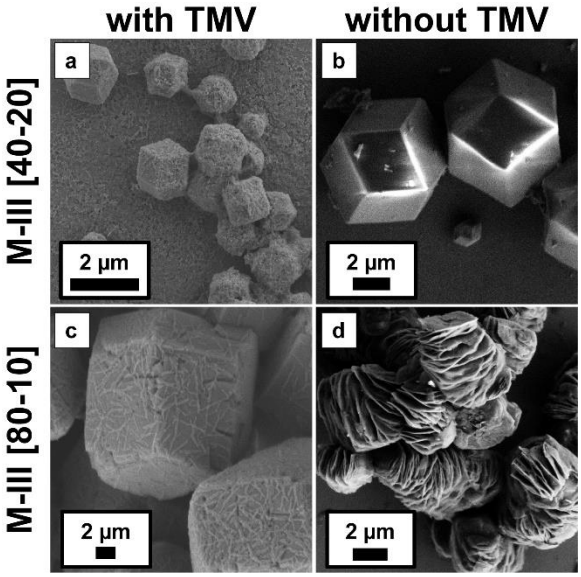

Figure 3.11. SEM micrographs of resultant products obtained at varied metal concentration and L/M ratios from the M-III region of the Composite Transformation Map. a) and c), samples that were prepared with 1.6 pmol TMV; b) and d), samples that were prepared without TMV.

The M-III region is characterized by the formation of multiple morphologies of products, including a mixture of discrete rod-like nanoparticles and r.d. crystals (M-III [20-60], Figure 3.5 c), a mixture of ill-shaped nanorods and r.d. crystals (M-III [40-20], Figure 3.11 a), and r.d. crystals with embedded rod-like CSBNs on the surface (M-III [80-10], Figure 3.11 c), respectively. A very curious observation was the presence of the non-porous dia(Zn) polymorph (M-III [80-10], Figure 3.12) that has been previously described,[64] also very recently noted in the case of biomimetic mineralization.[38] It is not possible to say if the formed CSBNs contain this non-porous polymorph as multiple crystalline phases as well as morphologies are presented in these syntheses. At low metal concentrations and high L/M ratios (*e.g.* M-III [20-60]), free rod-like CSBNs and free-

standing r.d. crystals with apparently biomimetically mineralized TMV stuck to the surface were obtained. Based upon a pristine PXRD and inspection by SEM, they are exclusively ZIF-8. We confirmed by PXRD that the spontaneously produced (*i.e.* TMV-free solution) crystals are the same phase(s) as their TMV-laden counterpart composites (Figure 3.6 b and Figure 3.12 b).

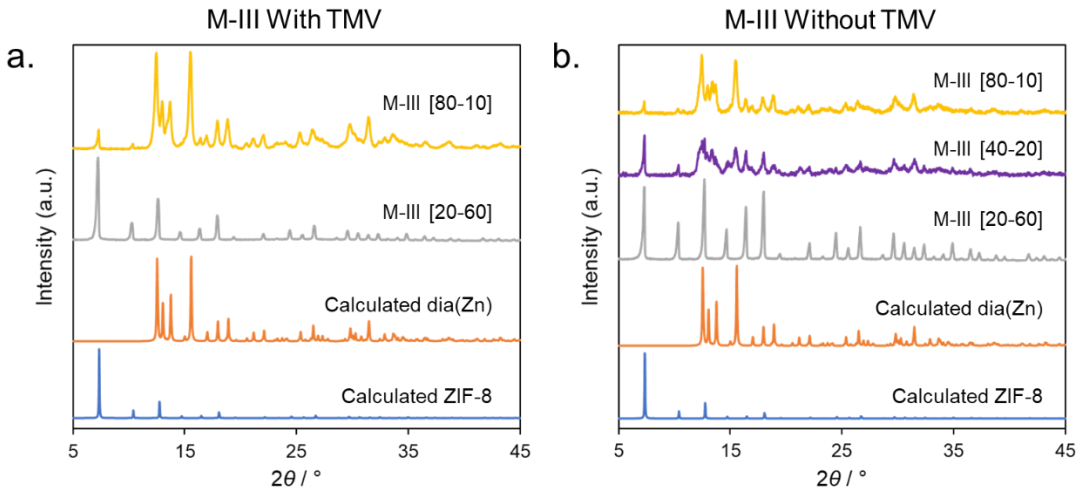

Figure 3.12. Representative PXRD patterns of resultant products obtained at varied metal concentration and L/M ratios from the M-III region; a) samples were prepared with 1.6 pmol TMV and b) samples were prepared without TMV.

M-IV: Rhombic Dodecahedral Crystal Composites

After conditions pass through the M-III region, the reaction systems begin to yield excellent consistency in the M-IV grouping of synthetic conditions. As shown in Figure 3.5 e, f and Figure 3.13, all the resultant composites appear as r.d. crystals with sizes ranging from about 100 nm to a few microns. It is worth noting that though no rod-like CSBNs could be found in those r.d. crystal composites, all micron-sized composites possess what appears to be small rods of TMV stuck to the outer surface of these r.d. crystals—something also observed in the isolated M-III crystals—while the nano-sized composites are frequently observed interconnected (Figure 3.13 g and k).

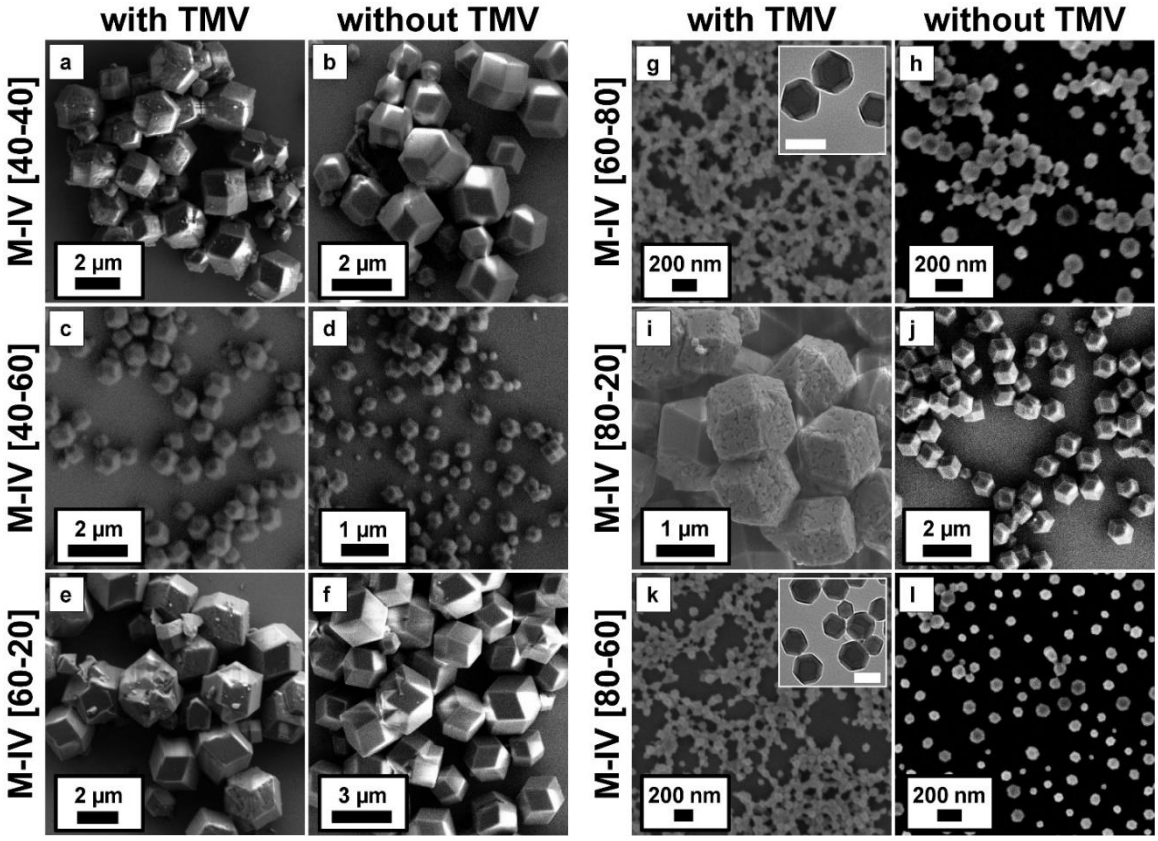

Figure 3.13. SEM micrographs of resultant products obtained at varied metal concentration and L/M ratios from the M-IV region of the Composite Transformation Map. a), c), e), g), i) and k), samples that were prepared with 1.6 pmol TMV; b), d), f), h), j) and l), samples that were prepared without TMV. Inset TEM micrographs of g) and k): scale bar = 100 nm.

Hitherto, we had suspected that the TMV nucleated the growth of all crystalline products—both the rod-like and r.d. morphologies—in solution. However, by conducting time-dependent crystallization and SEM analysis, we found the actual mechanism to be more complicated.

As illustrated in Figure 3.14, rod-like CSBNs were present at the 5-min point of the reaction along with amorphous granules—the kinetic product. The r.d. crystals with smooth surfaces formed independently from the CSBNs at the 60-min mark while the CSBNs and amorphous granules continue to populate the visual field.

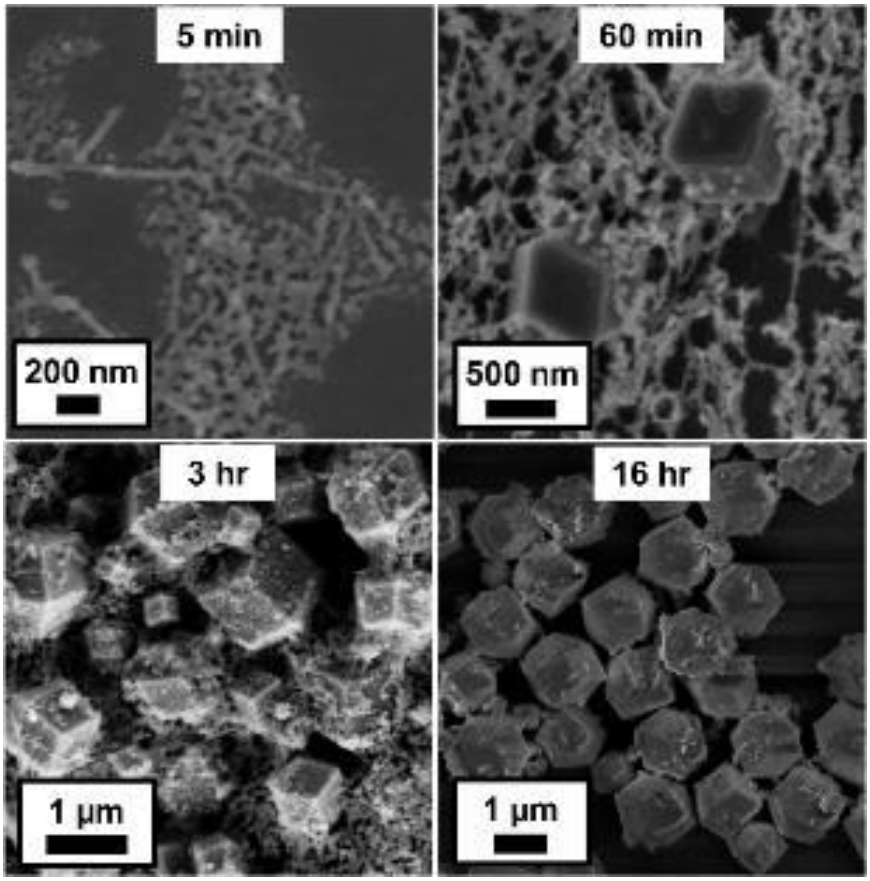

Figure 3.14. Time-dependent SEM characterization of M-IV [20-80] that illustrates the morphology of as-obtained TMV@ZIF-8 composites at each investigated time point.

At the 3-hr point of the reaction, the r.d. crystals were larger and had rod-shaped embossments on the surface of the crystals. Finally, at 16-hr, though no significant changes were found to the crystals, the free-standing rod-shaped particles were gone, indicating all the CSBNs have been bound to the surface of the r.d. crystals.

The same set of time dependent SEM experiments were conducted with M-III [80-10] composites and a similar growth pattern was found (Figure 3.15), though some CSBNs remained free, which is typical of the mixed morphologies produced under M-III conditions.

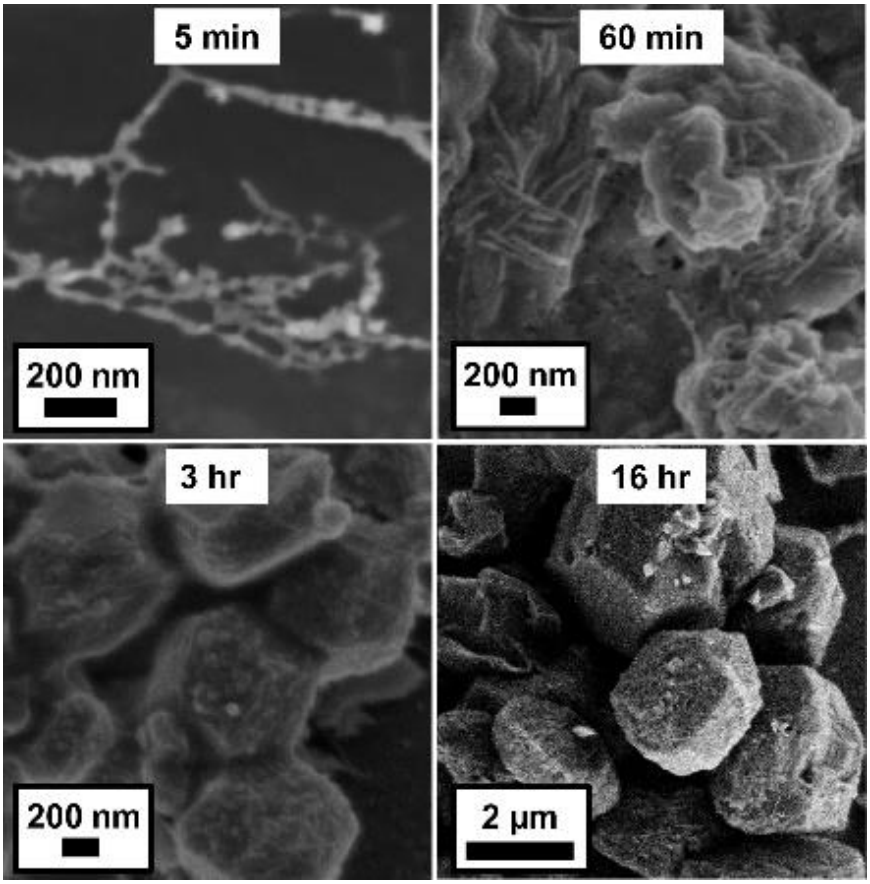

Figure 3.15. Time dependent SEM characterization of M-III [80-10] that illustrates the morphology of as-obtained TMV@ZIF-8 composites at each investigated time point.

To demonstrate further that the CSBNs were surface bound only after core formation, we labeled the interior channel of TMV with the green fluorescent FITC tag (denoted as *in*FITC-TMV, Figure 3.18 d) and prepared them as the M-IV [20-80] composite. Confocal laser scanning microscopy (CLSM) images reveal fluorescence primarily on the edge of the r.d. crystals (Figure 3.16)—consistent with the time-dependent SEM results. In other words, the CSBNs appear to adsorb to the surface after r.d. crystals of ZIF-8 form. We speculate that the kinetically produced amorphous granules equilibrate to form ZIF-8, as these granules are gone at the end of the reaction by SEM.

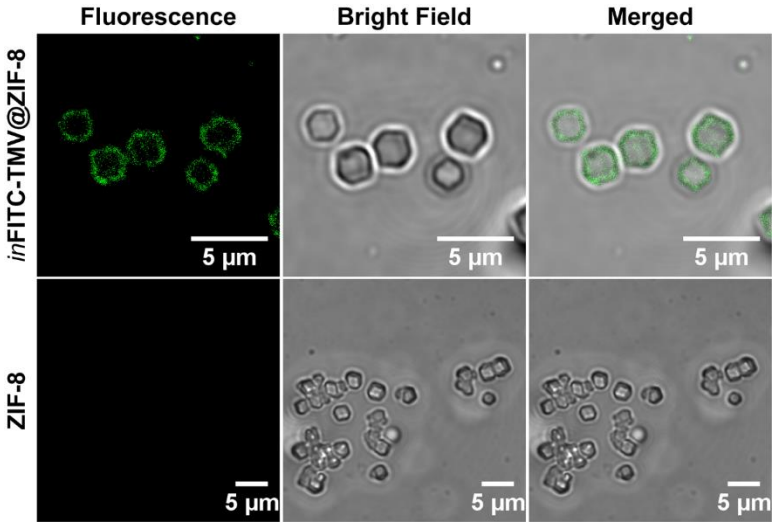

Figure 3.16. CLSM images of inFITC-TMV@ZIF-8 grown at M-IV [20-80] and the TMV-free ZIF-8 grown under the same conditions. The fluorescence is localized in the outer edges of the crystal. Additional z-stack "3D" images are available in Figure 3.17.

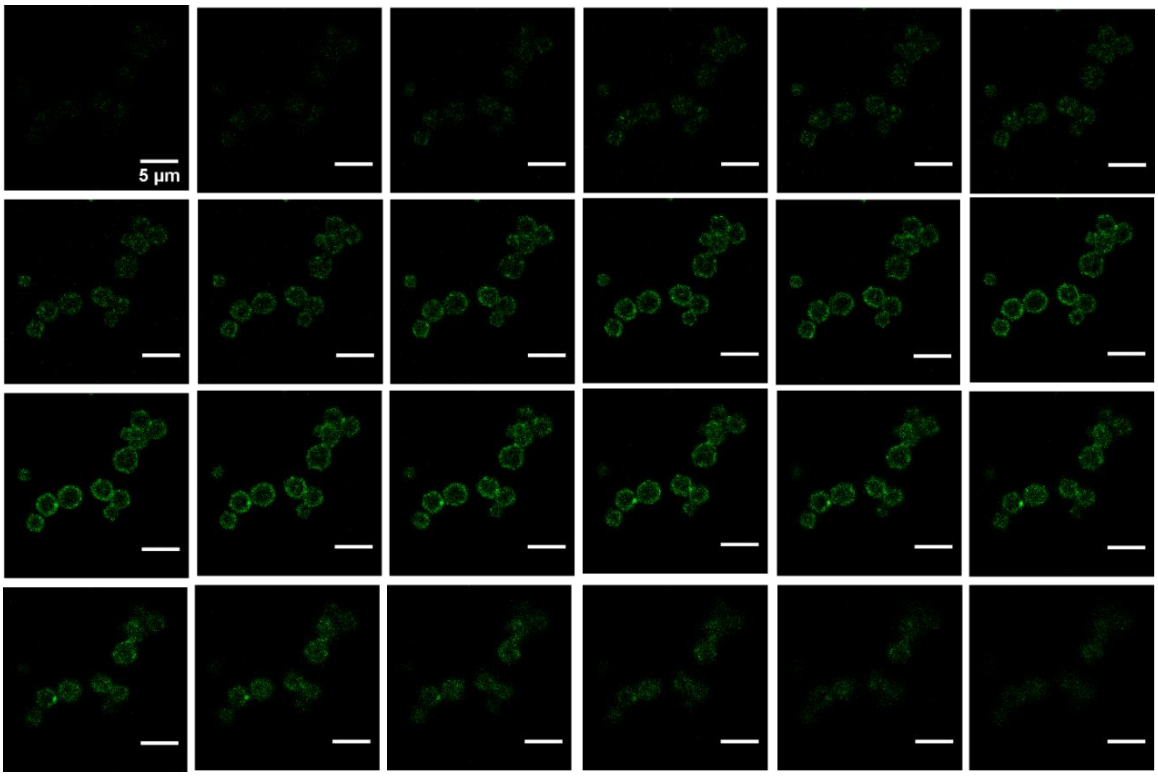

Figure 3.17. CLSM Z-Stack Images of CLSM images of inFITC-TMV@ZIF-8 grown at M-IV [20-80]. Each 0.2 µm slice shows that the FITC fluorescence is confined to the outer edges of the ZIF-8 crystal.

II. The Impact of Surface Charge

The surface charge dependence of crystal growth was also investigated. The isoelectric point (IP) of TMV is 3.5, and in our experiments, under all growth conditions, the surface of TMV has a negative charge, owing to the alkaline nature of HMIM. We hypothesized somewhat intuitively that the induced crystallization was driven by electrostatic interactions between the negatively charged viral particles and metal cations. Because bioconjugation of organic substrates is a very common way to add functionality to viral nanoparticles and biomacromolecules in general, we wondered how the yield of biomimetic mineralization would be impacted by common changes of surface charge induced by typical bioconjugation reactions on the surface of the virus. TMV possesses a tyrosine on the exterior surface, which can be modified via diazonium coupling.[65] The virus also contains glutamate residues on the interior surface, which can be modified by EDC coupling.[65] In this way, we could add a green fluorescent FITC tag to the interior after modifying the exterior to produce *ex*R-*in*FITC-TMV conjugates (where *ex*R-TMV, R= 1C/2C/1A/2A/PEG in Figure 3.18 c). Surface charges were varied by attaching to the exterior one or two anionic carboxylate-terminated functional groups (*ex*1A-TMV and *ex*2A-TMV) to enhance the surface negative charge and one or two cationic tetraalkylammonium-terminated functional groups (*ex*1C-TMV and *ex*2C-TMV) to introduce positive charge. We also introduced a PEG2000 (*ex*PEG-TMV*)* polymer to the surface as a charge neutral—though sterically encumbering—functional group.

In a typical bioconjugation reaction, we first treated TMV with *in situ* prepared diazonium salt of 3-ethynylaniline to introduce an alkyne group to the exterior of TMV (Figure 3.18 b). We used high-performance liquid chromatography/electrospray ionization mass spectrometry (HPLC/ESI-MS) data (see SI) to determined that >90% of the TMV coat protein monomers were converted to

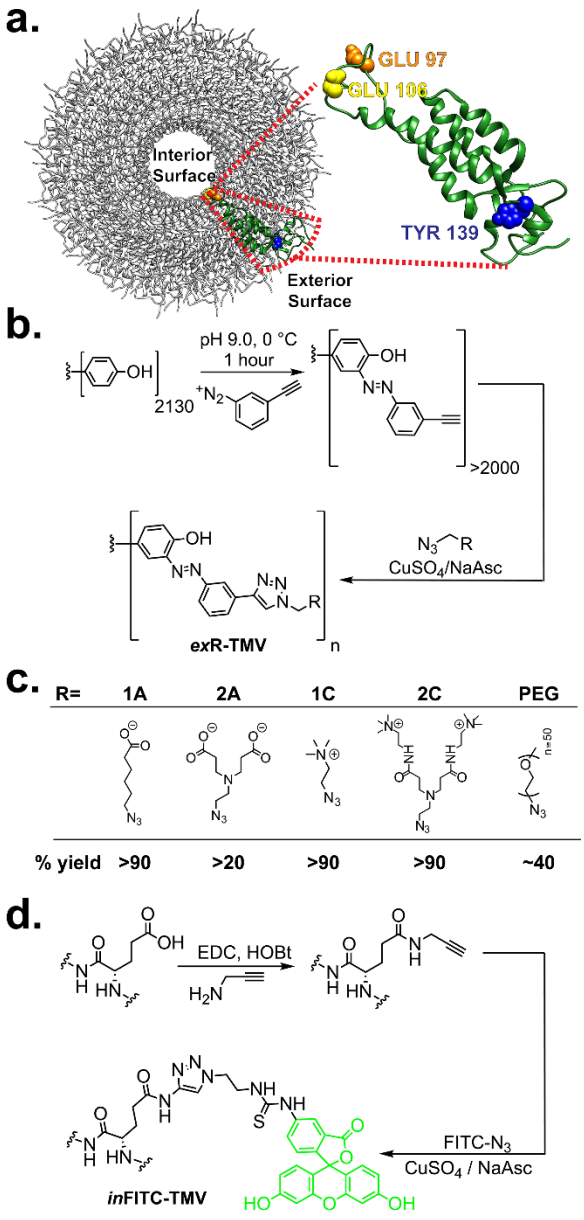

Figure 3.18. a) Crystallographic (PDB ID: 2TMV) structure of TMV with known reactive residues highlighted. b) The bio-conjugation strategy used to functionalize the exterior of TMV at Y139 with linkers to produce exR-TMV where R is defined in c) the table of linkers, which also indicated the percentage of modification to the TMV. d) Shows the bio-conjugation strategy used to functionalize the interior of TMV at E97 and E106 with FITC-N3 to produce inFITC-TMV. When the two syntheses are conducted sequentially on the same TMV, the product is denoted as exR-inFITC-TMV.

the alkyne derivative. We then used a Cu(I)-catalyzed azide-alkyne cycloaddition (CuAAC) reaction to attach the functionalized azides (Figure 3.18 c) to the TMV surface.

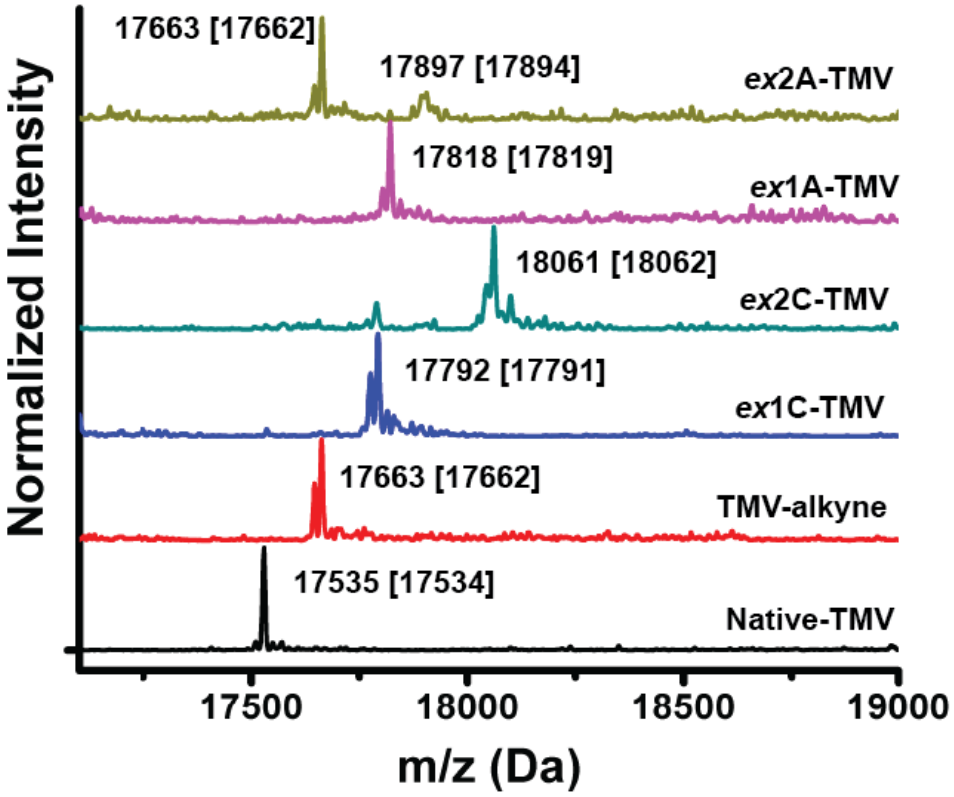

Figure 3.19. ESI-MS of exR-TMV conjugates.

From our HPLC/ESI-MS data (Figure 3.19), we found generally good yields—in excess of 90%—with the exception of the doubly-anionic carboxylate *ex*2A-TMV, and *ex*PEG-TMV; however, these yields are in line with literature values.[66]. Following exterior functionalization, the interior was conjugated via a routine procedure using a modified FITC-N_3 tag (see Supporting Information for FITC-N_3 attachment). The surface charge of TMV after these surface modifications was qualitatively analyzed by agarose gel band shift assay (Figure 3.20 a). Compared to native TMV, the cationic ammonium-functionalized TMV (*ex*1C-*in*FITC-TMV and *ex*2C-*in*FITC-TMV) shows

retarded mobility towards the positive electrode at the bottom of the gel while the anionic carboxylate-functionalized TMV (*ex*1A-*in*FITC-TMV and *ex*2A-*in*FITC-TMV) demonstrated enhanced mobility towards the positive electrode. To ascertain CSBN yields of each conjugate, the doubly modified *ex*R-*in*FITC-TMV conjugates were individually added to ZIF-8 precursors under identical conditions (M-II [20-20]) and the resultant solutions centrifuged and the products characterized by SEM and PXRD (Figure 3.21 and 3.22) after they were activated by soaking in methanol. The samples did not show any difference in terms of morphology and crystallinity—each sample contained pristine ZIF-8 coated CSBNs—however, there was a noticeable difference in the yield between each batch. Yields were determined via fluorescence spectroscopy of the reaction solution after all solids were removed and these data are plotted in Figure 3.20 b as the amount of free TMV.

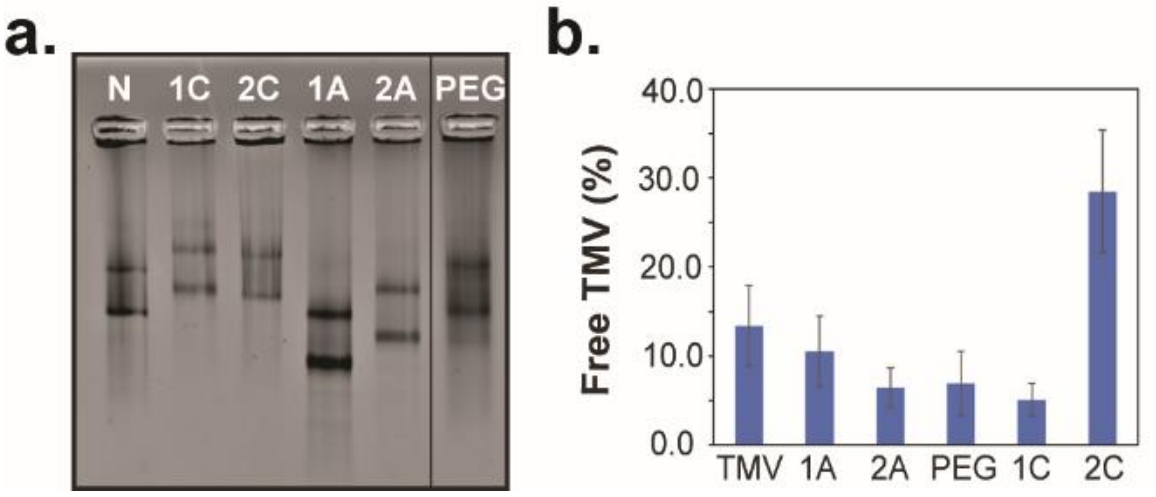

Figure 3.20. a) Band shift assay by agarose gel electrophoresis comparing native TMV (N= inFITC-TMV) and TMV functionalized with one of the five linkers (1C= ex1C-inFITC-TMV; 2C= ex2C-inFITC-TMV; 1A= ex1A-inFITC-TMV; 2A= ex2A-inFITC-TMV and PEG= exPEG-inFITC-TMV). Migration toward the positive electrode at the bottom corresponds to more negatively charged TMV assuming functional groups do not significantly affect the size of the original virus. b) Encapsulation efficiency, as determined by fluorescence of the remaining supernatant from CSBN formation, as the surface charge is altered.

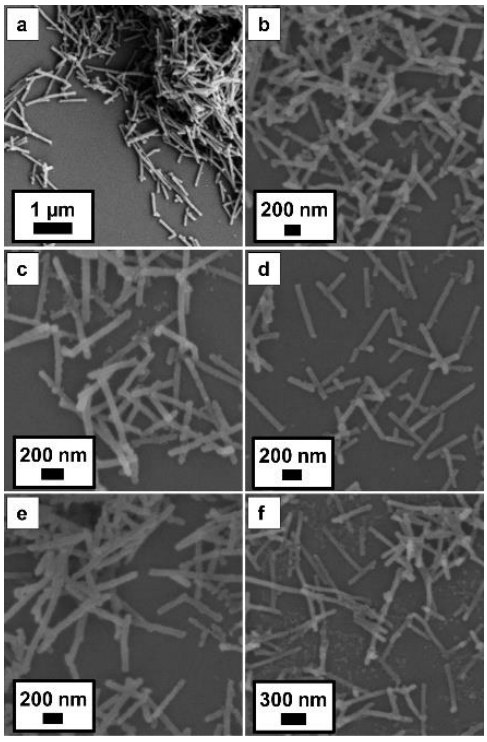

Figure 3.21. SEM micrographs of as-prepared TMV@ZIF-8 with using a) inFITC-TMV; b) exPEG-inFITC-TMV; c) ex1A-inFITC-TMV; d) ex2A-inFITC-TMV; e) ex1C-inFITC-TMV and f) ex2C-inFITC-TMV.

The TMV featuring the most positive charges (*ex*2C-*in*FITC-TMV) shows the highest free TMV content after crystallization, while the other modifications do not appear to affect the yield. This is instructive, as it suggests that CSBN formation proceeds in very good yields (~90%) under most circumstances, unless the surface is highly positively charged, in which case the yield is still ~70%. Interestingly, the yield of the CSBN on *ex*PEG-*in*FITC-TMV appeared unaffected by the PEG2000 chain. This was modestly surprising as PEG coatings are routinely used to inhibit antibody recognition[67-68] of TMV by blocking the protein surface from antibody recognition. Molecular dynamics (MD) computer simulations of a TMV with 45% PEG 2000 coverage (namely 22 of the 49 proteins in the MD unit cell have PEG attached to their modified TYR-139 residue, see SI for

details) were performed to quantify the exposure of the protein outer cylinder surface. The actual exposure is 72% using a small probe size (see SI for details), 44% using a medium probe size, and 11% using a large probe size. Which probe size is appropriate depends on the context: since antibodies are large, the low exposure for the large probe size suggests, correctly, that this PEG coverage is sufficient to inhibit antibody recognition. On the other hand, using a smaller probe size would suggest, again in agreement with the experimental data, that this PEG coverage is inadequate to prevent biomimetic mineralization. Together, this indicated that ZIF-8 could be an effective capping strategy for highly functionalized biomaterials—even those with functionality that can evade antibody binding.

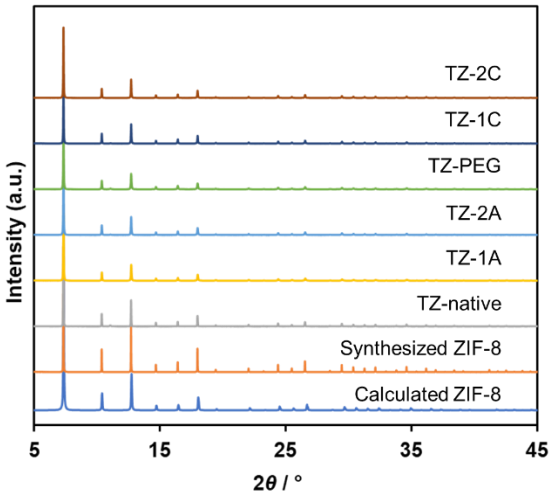

Figure 3.22. PXRD patterns of as-prepared ZIF-8 and TMV@ZIF-8 with using inFITC- TMV (TZ-native); ex1A-inFITC-TMV (TZ-1A); ex2A-inFITC-TMV (TZ-2A); exPEG-inFITC-TMV (TZ-PEG); ex1C-inFITC-TMV (TZ-1C); and ex2C-inFITC-TMV (TZ-2C), respectively.

The attenuated yield of CSBN formation on the highly charged doubly-cationic conjugate (*ex*2C-*in*FITC-TMV) suggests coulombic repulsion with either Zn or protonated ligand H_2MIM^+. To determine which of these two species were being affected, Isothermal titration calorimetry (ITC) was conducted with zinc acetate into TMV and ligand in two separate experiments (Figure 3.23 a).

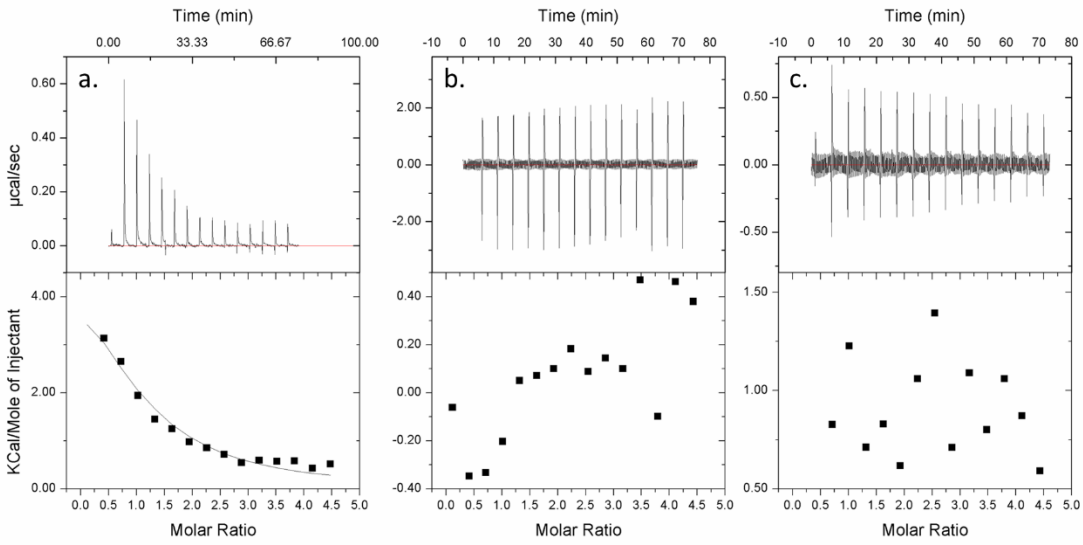

Figure 3.23. Results of Isothermal Titration Calorimetry for a) 3 mM Zn(OAc)2 binding to TMV in 0.1 M 1-MIM (pH 9.61) (Ka:2.27 × 104 M-1 ± 3.08 × 103; ΔH: 6636 ± 329.4 cal/mol; ΔS: 42.2 cal/mol deg; ΔG: -5939.6); b) HMIM binding to TMV 0.1 M 1-MIM (pH 9.61); c) 3 mM HMIM titrated into 0.1 M 1-MIM (pH 9.61); All isotherms are background corrected with the first 0.4 µL injection discarded and fit to a one site binding model. Plots (b) and (c) could not be fit due to the small binding enthalpies of these systems.

To mimic the reaction conditions—in particular the presence of ligand and the alkaline pH—the zinc acetate titrant and TMV titrate solutions were diluted with the same stock solution of 1-methylimidazole (1MIM). 1MIM is a constitutional isomer of HMIM (or 2-methylimidazole) incapable of forming extended frameworks on its own,[69] yet increases the pH and coordinates to Zn from its lone coordinating nitrogen. ITC shows endothermic binding of Zn under these conditions with an estimated K_a of 10^4 M^{-1}. Analysis of the surface of TMV show primarily the alcohol functionalized serine and threonine as the most exposed amino acid side chains as well as aspartic acid (Figure 3.24). A review of the literature[70] shows proteins rich in these side chains do indeed bind zinc at physiological pH with binding constants of ~10^5 M^{-1}, are endothermic, and binding is entropically driven. When this experiment was repeated with the HMIM ligand as the

titrant, however, there was no detectable enthalpy of binding to TMV (Figures 3.23 b), suggesting that the ligand may have limited ability to interact with the protein surface. In any case, recent literature has shown that the protonated ligand HMIM—much less H_2MIM^+ the conjugate acid of HMIM—does not participate in the formation of ZIF-8.[59]

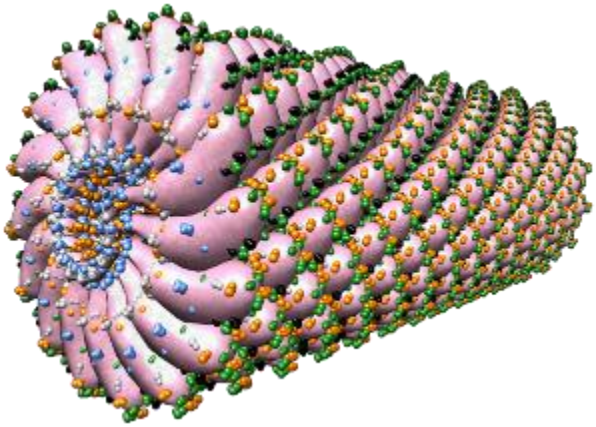

Figure 3.24. Image of the Tobacco Mosaic Virus with solvent excluded surface area in pink. Polar resides in the solvent exposed region are indicated as space filling models and colored thusly: The alcohol functionalized groups: Serine is green and Threonine is orange; the carboxylate groups: Aspartic Acid is black and Glutamic Acid is blue; and the amide functionalized Glutamine is grey. The exterior shows a high density of serine, threonine, and aspartate groups and the interior is rich in glutamic acid and threonine.

These results cumulatively paint a compelling picture that zinc cations accumulate at the surface and are exchanging within the microenvironment around the TMV creating "pseudo" elevated concentration. From Figure 3.2, we see that the spontaneous formation of ZIF-8 occurs at elevated zinc concentrations for a given L/M ratio. This very local concentration of zinc permits ZIF-8 growth on the TMV, even though zinc concentrations in bulk solution are otherwise too low. Further, as the absolute Zn concentration is increased, and the L/M ratio remains high, r.d. ZIF-8 forms in solution in a separate crystal growth process. It is clear that the kinetics of CSBN formation is faster than r.d. ZIF-8 formation indicating underlying mechanistic differences in

crystal formation and growth. This mechanism is most certainly dependent upon the surface charge of the protein, as shown by the attenuated yield when the surface was made more cationic.

3.3 Conclusion

We have conducted a comprehensive study to elucidate the mechanistic underpinnings of core-shell bionanoparticle formation (CSBNs) with ZIF-8 on TMV and have come to discover the mechanism is far less straightforward than we had originally suspected. That is, i) the TMV-catalyzed biomimetic mineralization of ZIF-8 is still greatly influenced by precursor concentrations and L/M ratios, which coherently work with viral particles to produce various morphologies and crystallinities that are summarized in the Composite Transformation Map (Figure 3.2); ii) the formation of CSBNs, which we subjectively considered the most interesting form of biology@MOF composites, highly favors the synthetic conditions that dominantly produce kinetic products—amorphous granules—rather than more ripened conditions that yield ZIF-8 crystals spontaneously; and iii) the growth of ZIF-8 on the surface of biomolecules, at least in the case of TMV, proceeds at different rates from ZIF-8 in solution and is likely catalyzed by a high local concentration of zinc in and around the microenvironment of the proteins owed to modest association of the zinc ions to the amino acid side chains. Nevertheless, the formation of CSBNs is sufficiently rugged that modification of surface charge or even steric encumbrance still produces decent yields of CSBNs, unless a high loading of positive charge is installed on the exterior of viral particles. This suggests that CSBN formation and biomimetic mineralization processes with ZIF-8 are a viable strategy for a wide variety of proteins making this a highly amenable method for many different protein surfaces.

3.4 Experimental

3.4.1- Chemicals

All the solvents and reagents for buffers were purchased from Fisher Scientific. Ethylenediaminetetraacetic acid (EDTA), 1-methylimidazole, 2-methylimidazole, zinc acetate dihydrate, 2-bromoethylamine hydrobromide, 2-chloro-N,N-dimethylethylamine hydrochloride, anhydrous magnesium sulphate, iodomethane, 6-bromohexanoic acid, methyl acrylate, 1,2-diaminoethane, Poly(ethylene glycol) methyl ether (PEG-2000), *p*-toluenesulfonyl chloride, sodium nitrite, *p*-toluenesulfonic acid monohydrate, 3-ethynylaniline, cupric sulfate pentahydrate, sodium ascorbate, aminoguanidine hydrochloride, 1-(3-dimethylaminopropyl)-3-ethylcarbodiimide hydrochloride (EDC), 1-hydroxybenzotriazole hydrate (HOBt), propargylamine, triethylamine, fluorescein isothiocyanate isomer I (FITC), sodium azide, β-mercaptoethanol, polyethylene glycol 8000 (PEG-8000), and Triton X-100 surfactant were purchased from Alfa Aesar, Acros Organics, Fisher Scientific, or Sigma Aldrich, and used without further purification. Protein concentration was measured using a Pierce™ Modified Lowry Protein Assay Kit (Thermal Fisher Scientific, Waltham, MA).

3.4.2- Scanning Electron Microscopy (SEM)

SEM was done on a Zeiss Supra 40 at 2.5 kV with SE2 detector. Samples were prepared by either drop-casting 5 µL of the sample suspension onto a clean silicon substrate or by mixing a small amount of sample powder in a pipette tip with a 5 µL drop of ultrapure water by repeatedly pipetting up and down. The drop was then wicked off with Whatman #2 filter paper, and dried in air.

3.4.3- Transmission Electron Microscopy (TEM)

TEM was done on a JEOL JEM-1400plus at 120 kV with a Gatan CCD 4K×4K detector. Samples were prepared by applying 5 µL of sample solution onto a 300-mesh Formvar-carbon-coated copper grid (Electron Microscopy Sciences, Hatfield, PA, USA) for at least 30 sec, and wicking off the drop with Whatman #2 filter paper. If negative staining was required, a 5 µL of 2% uranyl acetate (SPI Supplies, West Chester, PA, USA) was then applied to the grid for at least 30 sec, then wicked off with filter paper as above. The grids were then dried in air and stored under ambient conditions until imaged.

3.4.4- Powder X-ray Diffraction (PXRD)

PXRD data for all the samples shown in Figure 3.9, 3.10 and 3.12 were collected by using a Rigaku SmartLab X-ray diffractometer with CuKα (1.54060 Å) at 40 kV and 30 mA. The scans were performed for 2θ from 5° to 55° with a step size of 0.01°.

3.4.5- High Resolution Powder Diffraction

PXRD data that is shown in Figure 3.22 were collected from the 11-BM beamline at the Advanced Photon Source at Argonne National Laboratory. The samples were characterized using a wavelength of 0.457676 Å that scans 2θ from 0.5° to 50° with a step size of 0.001°.

3.4.6- Nuclear Magnetic Resonance (NMR)

NMR spectra were measured using a Bruker AVANCE III 500 MHz spectrometer with $Si(CH_3)_4$ used as a reference standard.

3.4.7- Size Exclusion Chromatography (SEC)

Analytical SEC was performed using an Agilent 1100 series HPLC system on a GS400SWXL (7.8 mm × 300 cm) column with 100 mM pH 7.4 KP buffer with 0.05% NaN_3.

3.4.8- NanoDrop

The concentration of native TMV was determined via UV-Vis measurements on a Thermo Scientific NanoDrop™ One spectrophotometer. UV-vis measurement was taken at 260 nm (RNA) and 280 nm (coat protein). A ratio of A_{260}/A_{280} of 1.2 indicates intact TMV. The concentration of TMV was calculated by using the Beer-Lambert Law with A_{260} and extinction coefficient of 3 $mL \cdot mg^{-1} \cdot cm^{-1}$ as reported.[65]

3.4.9- Lowry Assay

The concentration of surface-functionalized TMV was determined by Pierce™ Modified Lowry Protein Assay Kit (Thermal Fisher Scientific) on a Biotek Synergy H4 hybrid reader.

3.4.10- Fluorescence Spectrometry

Fluorescence emission spectra were collected on a Horiba Fluorolog spectrofluorometer. The excitation wavelength was set at 480 nm and emission spectra was collected from 500 nm to 700 nm.

3.4.11- Confocal Microscopy

Fluorescence imaging was performed on an Olympus FV300RS Confocal Microscope with a 100× oil immersion objective. Filter Sitting: FITC (Excitation: 488 nm, Emission: 490-525 nm). Z Stacks were acquired using 0.2 µm slices over 20 µm.

3.4.12- Isothermal Calorimetry

All measurements performed using a MicroCal ITC200 calorimeter at 25 °C. Data was analyzed as a non-linear regression with single site binding model and the first 0.4 µL injection was discarded. All integration and normalization were performed in ORIGIN v. 7.0 (MicroCal Inc). Additional experimental parameters: Reference power of 1.2 V; Stirring of 2000 rpm.

3.4.13- TMV Purification

TMV was collected and purified according to a literature method.[65] 100 g of infected *Nicotiana Benthamiana* leaves were ground in a blender in ~500 mL cold extraction buffer (0.1 M pH 7.4 potassium phosphate buffer with 0.2% (w/v) 2-mercaptoethanol). The homogenate was stirred for 30 min on ice then filtered through several layers of cheesecloth and the filtrate collected. The leftover pulp was ground in a mortar and pestle with extraction buffer and refiltered, collecting the combined filtrates. The filtrates were centrifuged at 11000 ×*g* (7676 rpm in Fiberlite F10-4×1000 LEX rotor) for 20 min at 4 °C. The supernatant was filtered through more cheesecloth to remove extra plant matter and an equal volume (~500 mL) of 1:1 chloroform:*n*-butanol solution was added to the filtrate and stirred on ice for 30 min. The mixture was centrifuged at 4500 ×*g* (4909 rpm in Fiberlite F10-4×1000 LEX rotor) for 10 min at 4 °C to break the emulsion. The aqueous layer was separated and collected. NaCl was added to 0.2 M, 8% (w/v) PEG-8000 and 1% (w/v) Triton X-100 was added and the solution stirred on ice for 30 min and stored at 4 °C for 1 hr. The solution was centrifuged at 20600 ×*g* (10500 rpm in Fiberlite F10-4×1000 LEX rotor) for 20 min at 4 °C. The supernatant was discarded and the pellet resuspended overnight in 0.1 M pH 7.4 potassium phosphate buffer. Sucrose gradients were prepared in ultraclear centrifuge tubes by freezing 40% (w/w) sucrose in 0.1 M pH 7.4 potassium phosphate buffer at -20 °C and thawing to room

temperature at least once. The resuspended pellet solution was carefully layered on top of the sucrose gradient and ultracentrifuged at 96000 ×*g* (28000 rpm in SW-28 rotor) for 120 min at 4 °C in a swing-bucket rotor with no brake. The light-scattering blue band was collected from each tube, combined, diluted with 0.1 M pH 7.4 potassium phosphate buffer and ultracentrifuged at 160000 ×*g* (70000 rpm in Type 70 Ti rotor) for 180 min at 4 °C. The clear pellet was resuspended in a minimum volume of 0.1 M pH 7.4 potassium phosphate buffer overnight. The solution was portioned into microcentrifuge tubes and centrifuged at 7500 ×*g* (8800 rpm in Legend 17 microcentrifuge) for 15 min. The supernatants were collected and combined to form the final purified virus solution. The solution was characterized with NanoDrop, SDS-PAGE, native agarose gel electrophoresis, size-exclusion chromatography, and TEM.

3.4.14- TMV Desaltation

TMV solutions were desalted with an Amicon Ultra-4 (MWCO 10 kDa) centrifugal filter unit (MilliporeSigma, Burlington, MA, USA) by centrifuging at 4303 ×*g* (4300 rpm in SX4750 rotor) for 10 to 30 min as needed at 4 °C. Ultrapure water (1 – 3 mL) was added to the concentrated solution and recentrifuged at least two more times, adding ultrapure water after each cycle. The final solution was collected and the concentration was determined by NanoDrop.

3.4.15- Preparation of TMV-templated Crystallization (Composite Transformation Map)

Desalted TMV solution (contains 0.0625 mg of TMV, the concentration of TMV solution could be 2~10 mg/mL) was added into a 1.5 mL Eppendorf tube, followed by 500 μL of HMIM aqueous solution and 500 μL of $Zn(OAc)_2$ aqueous solution. The precursor concentrations studied can be referred to the Composite Transformation Map (Figure 3.2). After shaking for 20 sec the mixture

was set on the bench overnight under ambient conditions. The precipitates were collected by centrifugation at 2656 ×*g* for 10 min. The product was washed by ultrapure water twice. The dry powder of the products was prepared by lyophilizing the products on a freeze-drier for 3 – 7 days.

3.4.16- Preparation of Spontaneous Crystallization Product (Composite Transformation Map)

The spontaneous crystallization samples were prepared using the same procedure as described above, except TMV was never added to any of the solutions.

3.4.17- Confocal Microscopy

A small amount of dry *in*FITC-TMV@ZIF-8 (prepared under P-IV [20-80] condition) or ZIF-8 crystals was dispersed in 50 µL of MilliQ water. Ten microliters of this solution was added to a 25 mm × 75 mm glass slide and a coverslip was applied. Excess water was removed with a stream of warm air, and the coverslips were sealed before imaging on the microscope.

3.4.18- Preparation of ethynylphenyldiazenylphenol-TMV (TMV-alkyne)

3-ethynylaniline diazonium salt was prepared by adding 400 µL of 0.3 M *p*-toluenesulfonic acid monohydrate, 75 µL of 0.68 M 3-ethynylaniline and 25 µL of 3.0 M sodium nitrite. The resultant mixture was cooled on ice for 1 h. Next, 142 µL of stock TMV solution (14.10 mg/mL) was diluted to 2 mg/mL with 808 µL of 0.1 M pH 8.8 borate buffer and cooled on ice. To this solution, 50 µL of *in situ* prepared 3-ethynylaniline diazonium salt was added and kept on ice for 1 hr. Next, the resultant straw-colored solution (TMV-alkyne) was purified with a PD MidiTrap G-25 column and the solutions were concentrated to 10 mg/mL with a 10K MWCO Pierce™ Protein Concentrator.

3.4.19- General procedure for the preparation of exR-TMV

200 µL of TMV-alkyne (10 mg/mL) was mixed with 730 µL of 0.1 M pH 7.4 KP buffer. Then, 10 µL of 0.01 M R-N_3 (10 eq per coat protein) and 10 µL of 0.1 M aminoguanidine hydrochloride were added to the TMV solution. Then, 10 µL of 0.1 M $CuSO_4$, 10 µL of 0.5 M Tris(3-hydroxypropyltriazolylmethyl)amine (THPTA) were mixed and added to above TMV stock solution. Finally, 10 µL of sodium ascorbate was added to the mixture and the resulting solution was incubated at room temperature for 2 h and 10 µL of 0.5 M EDTA was added to the reaction and incubated another 10 min. The reaction mixture was then purified with a PD MidiTrap G-25 column and the solutions were concentrated to 10 mg/mL with a 10K MWCO Pierce™ Protein Concentrator.

3.4.20- Preparation of exR-inFITC-TMV

The exterior surface of TMV was modified with R-N_3 as described in the "Exterior surface modification of TMV with R-N_3 Linkers" section. Then the interior surface was modified with propargyl amine using an EDC coupling reaction. 142 µL of stock *ex*R-TMV solution (10.0 mg/mL) was diluted to 2 mg/mL with 632 µL of 0.1 M pH 7.4 HEPES buffer at room temperature followed by the addition of 130 µL of 0.1 M TEMPO-NH_2, 3 mg of HOBt, and 96 µL of 0.1 M EDC. The reaction mixture was incubated at room temperature for 24 hrs, purified with a PD MidiTrap G-25 column, and the solutions were concentrated to 10 mg/mL with a 10K MWCO Pierce™ Protein Concentrator to yield interior alkyne modified exR-TMV (*ex*R-*in*PA-TMV). FITC-N_3 was then attached by the CuAAC reaction. 200 µL of *ex*R-*in*PA-TMV (10 mg/mL) was mixed with 750 µL of 0.1 M pH 7.4 KP buffer. Then, 10 µL of 0.01 M FITC-N_3 (10 eq per coat protein) and 10 µL of 0.1 M aminoguanidine hydrochloride were added to the *ex*R-*in*PA-TMV

solution. Next, 10 µL of 0.1 M $CuSO_4$ and 10 µL of 0.5 M THPTA were mixed together and was added to the above solution. Finally, 10 µL of sodium ascorbate was added to this solution, the reaction mixture was incubated at room temperature for 2 hrs, 10 µL of 0.5 M EDTA was added to the reaction, and the solution was incubated for another 10 min. The reaction mixture was then purified with a PD MidiTrap G-25 column and the solutions were concentrated to 10 mg/mL with a 10K MWCO Pierce™ Protein Concentrator to yield *ex*R-*in*FITC-TMV.

3.4.21- Preparation of exR-TMV@ZIF-8 CSBNs and exR-inFITC-TMV@ZIF-8 CSBNs

Desalted *ex*R-TMV or *ex*R-*in*FITC-TMV (R= 1C/2C/1A/2A/PEG, 0.0625 mg) was added into a 1.5 mL Eppendorf tube, followed by 500 µL of 400 mM HMIM aqueous solution and 500 µL of 20 mM $Zn(OAc)_2$ aqueous solution (P-II [20-20] condition). After shaking for 20 sec the mixture was set on the bench overnight under ambient conditions. All the mixtures formed flocculates right after shaking except the samples contain *ex*2C-TMV and *ex*2C-*in*FITC-TMV. The precipitates were collected by centrifugation at 2656 ×*g* for 10 min. The product was washed by ultrapure water twice.

3.4.22- Determination of free TMV after ZIF-8 crystallization

First, *ex*R-*in*FITC-TMV@ZIF-8 CSBNs were prepared as described above. After overnight reaction, the mixtures were centrifuged at 2656 ×*g* for 10 min. Then, 600 µL of supernatant was carefully collected with a pipette. The collected supernatant was further centrifuged at 2656 ×*g* for 10 min to ensure the small particles were completely pelleted down. Later, 500 µL of supernatant was thoroughly mixed with 500 µL of ultrapure water and 1500 µL of 0.5 M EDTA (pH 7.0). The as-prepared sample solution was transferred to a quartz cuvette and directly tested on

spectrofluorometer. Additional dilution may be needed if the excitation intensity exceeded the range. The emission spectrum was collected from 500 nm to 700 nm with excitation at 480 nm. The emission intensity was collected at 519 nm and brought to the pre-determined standard curve to calculate the concentration of free *ex*R-*in*FITC-TMV in the supernatant. The percentage of free *ex*R-*in*FITC-TMV was calculated by weight of free *ex*R-*in*FITC-TMV (calculated concentration times the volume of original reaction mixture) divided by the original weight of *ex*R-*in*FITC-TMV (0.0625 mg).

Table 3.1. Free *ex*R-*in*FITC-TMV in the supernatant after overnight reaction that is determined by fluorimeter.

Sample	Exp-1	Exp-2	Exp-3	Ave	Stdev
	free%	free%	free%		
in FITC-TMV	19.4	12.2	8.5	13.4	4.5
ex 1A-*in* FITC-TMV	11.1	15.1	5.3	10.5	4.0
ex 2A-*in* FITC-TMV	9.5	4.6	5.2	6.4	2.2
ex PEG-*in* FITC-TMV	12.0	4.9	3.9	6.9	3.6
ex 1C-*in* FITC-TMV	7.6	3.1	4.5	5.1	1.9
ex 2C-*in* FITC-TMV	38.0	25.5	22.0	28.5	6.9

3.4.23- Isothermal Calorimetry

All measurements were performed with a 280 µL sample and reference cells at 25 °C. The titrant was 3 mM $Zn(OAc)_2$ or 2-methylimidazole (HMIM) in 0.1 M 1-methylimidazole (1-MIM) pH 9.61 and the titrant was 50 µM TMV coat proteins (TMV-CPs). Microliter injections (×15) were added to the TMV-CPs at 5-min intervals. Data was analyzed as a non-linear regression with single site binding model and the first 0.4 µL injection was discarded.

3.4.24- Investigation of Amorphous Granules

The dry powder (50 mg) of the spontaneous product of P-II [20-20] (no TMV) was dispersed in 10 mL pure methanol in a closed scintillation vial. The sample was left in the hood under ambient conditions for 12 days. The excess methanol was decanted and the solid was air-dried under ambient conditions overnight. The as-obtained dry powder was sampled for SEM and PXRD as described in the Materials and Methods section.

3.5 Appendix

Detailed organic syntheses and bioconjugation refer to DOI: 10.1021/acsami.8b01369.

3.6 References

1. Liang, K.; Carbonell, C.; Styles, M. J.; Ricco, R.; Cui, J.; Richardson, J. J.; Maspoch, D.; Caruso, F.; Falcaro, P. Biomimetic Replication of Microscopic Metal–Organic Framework Patterns Using Printed Protein Patterns. *Adv. Mater.* **2015,** *27*, 7293-7298.

2. Li, P.; Moon, S.-Y.; Guelta, M. A.; Harvey, S. P.; Hupp, J. T.; Farha, O. K. Encapsulation of a Nerve Agent Detoxifying Enzyme by a Mesoporous Zirconium Metal–Organic Framework Engenders Thermal and Long-Term Stability. *J. Am. Chem. Soc.* **2016,** *138*, 8052-8055.

3. Li, S.; Dharmarwardana, M.; Welch, R. P.; Ren, Y.; Thompson, C. M.; Smaldone, R. A.; Gassensmith, J. J. Template-Directed Synthesis of Porous and Protective Core–Shell Bionanoparticles. *Angew. Chem., Int. Ed.* **2016,** *55*, 10691–10696.

4. Doonan, C.; Riccò, R.; Liang, K.; Bradshaw, D.; Falcaro, P. Metal–Organic Frameworks at the Biointerface: Synthetic Strategies and Applications. *Acc. Chem. Res.* **2017,** *50*, 1423-1432.

5. Lian, X.; Fang, Y.; Joseph, E.; Wang, Q.; Li, J.; Banerjee, S.; Lollar, C.; Wang, X.; Zhou, H.-C. Enzyme-MOF (metal-organic framework) composites. *Chem. Soc. Rev.* **2017,** *46*, 3386-3401.

6. Majewski, M. B.; Howarth, A. J.; Li, P.; Wasielewski, M. R.; Hupp, J. T.; Farha, O. K. Enzyme encapsulation in metal-organic frameworks for applications in catalysis. *CrystEngComm* **2017,** *19*, 4082-4091.

7. Riccò, R.; Liang, W.; Li, S.; Gassensmith, J. J.; Caruso, F.; Doonan, C.; Falcaro, P. Metal–Organic Frameworks for Cell and Virus Biology: A Perspective. *ACS Nano* **2018**, *12*, 13-23.

8. Yaghi, O. M.; O'Keeffe, M.; Ockwig, N. W.; Chae, H. K.; Eddaoudi, M.; Kim, J. Reticular synthesis and the design of new materials. *Nature* **2003,** *423*, 705.

9. Park, K. S.; Ni, Z.; Côté, A. P.; Choi, J. Y.; Huang, R.; Uribe-Romo, F. J.; Chae, H. K.; O'Keeffe, M.; Yaghi, O. M. Exceptional chemical and thermal stability of zeolitic imidazolate frameworks. *Proc. Natl. Acad. Sci. U. S. A.* **2006,** *103*, 10186-10191.

10. Furukawa, H.; Cordova, K. E.; O'Keeffe, M.; Yaghi, O. M. The Chemistry and Applications of Metal-Organic Frameworks. *Science* **2013,** *341*, 1230444.

11. Abánades Lázaro, I.; Haddad, S.; Sacca, S.; Orellana-Tavra, C.; Fairen-Jimenez, D.; Forgan, R. S. Selective Surface PEGylation of UiO-66 Nanoparticles for Enhanced Stability, Cell Uptake, and pH-Responsive Drug Delivery. *Chem* **2017**, *2*, 561-578.

12. Li, Q.; Zhang, W.; Miljanić, O. Š.; Sue, C.-H.; Zhao, Y.-L.; Liu, L.; Knobler, C. B.; Stoddart, J. F.; Yaghi, O. M. Docking in Metal-Organic Frameworks. *Science* **2009,** *325*, 855.

13. Karagiaridi, O.; Lalonde, M. B.; Bury, W.; Sarjeant, A. A.; Farha, O. K.; Hupp, J. T. Opening ZIF-8: A Catalytically Active Zeolitic Imidazolate Framework of Sodalite Topology with Unsubstituted Linkers. *J. Am. Chem. Soc.* **2012,** *134*, 18790-18796.

14. Lu, G.; Farha, O. K.; Zhang, W.; Huo, F.; Hupp, J. T. Engineering ZIF-8 Thin Films for Hybrid MOF-Based Devices. *Adv. Mater.* **2012,** *24*, 3970-3974.

15. Gándara, F.; Furukawa, H.; Lee, S.; Yaghi, O. M. High Methane Storage Capacity in Aluminum Metal–Organic Frameworks. *J. Am. Chem. Soc.* **2014,** *136*, 5271-5274.

16. He, C.; Lu, K.; Lin, W. Nanoscale Metal–Organic Frameworks for Real-Time Intracellular pH Sensing in Live Cells. *J. Am. Chem. Soc.* **2014,** *136*, 12253-12256.

17. Kornienko, N.; Zhao, Y.; Kley, C. S.; Zhu, C.; Kim, D.; Lin, S.; Chang, C. J.; Yaghi, O. M.; Yang, P. Metal–Organic Frameworks for Electrocatalytic Reduction of Carbon Dioxide. *J. Am. Chem. Soc.* **2015,** *137*, 14129-14135.

18. Marshall, R. J.; Griffin, S. L.; Wilson, C.; Forgan, R. S. Single-Crystal to Single-Crystal Mechanical Contraction of Metal–Organic Frameworks through Stereoselective Postsynthetic Bromination. *J. Am. Chem. Soc.* **2015,** *137*, 9527-9530.

19. McGuirk, C. M.; Katz, M. J.; Stern, C. L.; Sarjeant, A. A.; Hupp, J. T.; Farha, O. K.; Mirkin, C. A. Turning On Catalysis: Incorporation of a Hydrogen-Bond-Donating Squaramide Moiety into a Zr Metal–Organic Framework. *J. Am. Chem. Soc.* **2015,** *137*, 919-925.

20. Mondloch, J. E.; Katz, M. J.; Isley Iii, W. C.; Ghosh, P.; Liao, P.; Bury, W.; Wagner, G. W.; Hall, M. G.; DeCoste, J. B.; Peterson, G. W.; Snurr, R. Q.; Cramer, C. J.; Hupp, J. T.; Farha, O. K. Destruction of chemical warfare agents using metal–organic frameworks. *Nat. Mater.* **2015,** *14*, 512.

21. Orellana-Tavra, C.; Marshall, R. J.; Baxter, E. F.; Lazaro, I. A.; Tao, A.; Cheetham, A. K.; Forgan, R. S.; Fairen-Jimenez, D. Drug delivery and controlled release from biocompatible metal-organic frameworks using mechanical amorphization. *J. Mater. Chem. B* **2016,** *4*, 7697-7707.

22. Lim, J.; Lee, E. J.; Choi, J. S.; Jeong, N. C., Diffusion Control in the in Situ Synthesis of Iconic Metal–Organic Frameworks within an Ionic Polymer Matrix. *ACS Appl. Mater. Interfaces* **2018,** *10*, 3793-3800.

23. Lykourinou, V.; Chen, Y.; Wang, X.-S.; Meng, L.; Hoang, T.; Ming, L.-J.; Musselman, R. L.; Ma, S. Immobilization of MP-11 into a Mesoporous Metal−Organic Framework, MP-11@mesoMOF: A New Platform for Enzymatic Catalysis. *J. Am. Chem. Soc*. **2011**, *133*, 10382−10385.

24. Lyu, F.; Zhang, Y.; Zare, R. N.; Ge, J.; Liu, Z. One-Pot Synthesis of Protein-Embedded Metal−Organic Frameworks with Enhanced Biological Activities. *Nano Lett*. **2014**, *14*, 5761−5765.

25. Chulkaivalsucharit, P.; Wu, X.; Ge, J. Synthesis of enzyme-embedded metal-organic framework nanocrystals in reverse micelles. *RSC Adv.* **2015,** *5*, 101293-101296.

26. Liang, K.; Ricco, R.; Doherty, C. M.; Styles, M. J.; Bell, S.; Kirby, N.; Mudie, S.; Haylock, D.; Hill, A. J.; Doonan, C. J.; Falcaro, P. Biomimetic Mineralization of Metal-Organic Frameworks as Protective Coatings for Biomacromolecules. *Nat. Commun*. **2015**, *6*, 7240.

27. Shieh, F.-K.; Wang, S.-C.; Yen, C.-I.; Wu, C.-C.; Dutta, S.; Chou, L.-Y.; Morabito, J. V.; Hu, P.; Hsu, M.-H.; Wu, K. C. W.; Tsung, C.-K. Imparting Functionality to Biocatalysts via Embedding Enzymes into Nanoporous Materials by a de Novo Approach: Size-Selective Sheltering of Catalase in Metal–Organic Framework Microcrystals. *J. Am. Chem. Soc*. **2015,** *137*, 4276-4279.

28. Wu, X.; Ge, J.; Yang, C.; Hou, M.; Liu, Z. Facile synthesis of multiple enzyme-containing metal-organic frameworks in a biomolecule-friendly environment. *Chem. Commun.* **2015,** *51*, 13408-13411.

29. Wu, X.; Hou, M.; Ge, J. Metal-organic frameworks and inorganic nanoflowers: a type of emerging inorganic crystal nanocarrier for enzyme immobilization. *Catal. Sci. Technol.* **2015,** *5*, 5077-5085.

30. Wu, X.; Yang, C.; Ge, J.; Liu, Z. Polydopamine tethered enzyme/metal-organic framework composites with high stability and reusability. *Nanoscale* **2015,** *7*, 18883-18886.

31. Li, P.; Modica, Justin A.; Howarth, Ashlee J.; Vargas L, E.; Moghadam, Peyman Z.; Snurr, Randall Q.; Mrksich, M.; Hupp, Joseph T.; Farha, Omar K. Toward Design Rules for Enzyme Immobilization in Hierarchical Mesoporous Metal-Organic Frameworks. *Chem* **2016,** *1*, 154-169.

32. Liang, K.; Coghlan, C. J.; Bell, S. G.; Doonan, C.; Falcaro, P., Enzyme encapsulation in zeolitic imidazolate frameworks: a comparison between controlled co-precipitation and biomimetic mineralisation. *Chem. Commun.* **2016,** *52*, 473-476.

33. Cui, J.; Feng, Y.; Lin, T.; Tan, Z.; Zhong, C.; Jia, S. Mesoporous Metal–Organic Framework with Well-Defined Cruciate Flower-Like Morphology for Enzyme Immobilization. *ACS Appl. Mater. Interfaces,* **2017,** *9*, 10587-10594.

34. Hou, M.; Zhao, H.; Feng, Y.; Ge, J. Synthesis of patterned enzyme–metal–organic framework composites by ink-jet printing. *Bioresour Bioprocess.* **2017,** *4*, 40.

35. Wang, Q.; Zhang, X.; Huang, L.; Zhang, Z.; Dong, S. GOx@ZIF-8(NiPd) Nanoflower: An Artificial Enzyme System for Tandem Catalysis. *Angew.Chem. Int. Ed.* **2017**, *56*,16082 – 16085.

36. Wu, X.; Yang, C.; Ge, J., Green synthesis of enzyme/metal-organic framework composites with high stability in protein denaturing solvents. *Bioresour Bioprocess.* **2017,** *4*, 24.

37. Zhang, C.; Wang, X.; Hou, M.; Li, X.; Wu, X.; Ge, J. Immobilization on Metal–Organic Framework Engenders High Sensitivity for Enzymatic Electrochemical Detection. *ACS Appl. Mater. Interfaces,* **2017,** *9*, 13831-13836.

38. Liang, W.; Ricco, R.; Maddigan, N. K.; Dickinson, R. P.; Xu, H.; Li, Q.; Sumby, C. J.; Bell, S. G.; Falcaro, P.; Doonan, C. J., Control of Structure Topology and Spatial Distribution of Biomacromolecules in Protein@ZIF-8 Biocomposites. *Chem. Mater.* **2018,** *30*, 1069-1077.

39. Liang, K.; Richardson, J. J.; Cui, J.; Caruso, F.; Doonan, C. J.; Falcaro, P. Metal–Organic Framework Coatings as Cytoprotective Exoskeletons for Living Cells. *Adv. Mater.* **2016**, *28*, 7910-7914.

40. Liang, K.; Richardson, J. J.; Doonan, C. J.; Mulet, X.; Ju, Y.; Cui, J.; Caruso, F.; Falcaro, P. An Enzyme-Coated Metal–Organic Framework Shell for Synthetically Adaptive Cell Survival. *Angew.Chem. Int.Ed. 2017, 56*, 8510-8515.

41. DiCosimo, R.; McAuliffe, J.; Poulose, A. J.; Bohlmann, G. Industrial use of immobilized enzymes. *Chem. Soc. Rev.* **2013,** *42*, 6437-6474.

42. Liese, A.; Hilterhaus, L. Evaluation of immobilized enzymes for industrial applications. *Chem. Soc. Rev.* **2013,** *42*, 6236-6249.

43. Min, K.; Yoo, Y. J. Recent progress in nanobiocatalysis for enzyme immobilization and its application. *Bioresour Bioprocess.* **2014,** *19*, 553-567.

44. Hou, M.; Ge, J. Chaper Three-Armoring Enzymes by Metal–Organic Frameworks by the Coprecipitation Method. In *Methods in Enzymology*, Kumar, C. V., Ed. Academic Press; 2017; Vol. 590, pp 59-75.

45. Shenton, W.; Douglas, T.; Young, M.; Stubbs, G.; Mann, S. Inorganic–Organic Nanotube Composites from Template Mineralization of Tobacco Mosaic Virus. *Adv. Mater.* **1999,** *11*, 253-256.

46. Schlick, T. L.; Ding, Z.; Kovacs, E. W.; Francis, M. B., Dual-Surface Modification of the Tobacco Mosaic Virus. *J. Am. Chem. Soc.* **2005,** *127*, 3718-3723.

47. Niu, Z.; Liu, J.; Lee, L. A.; Bruckman, M. A.; Zhao, D.; Koley, G.; Wang, Q. Biological Templated Synthesis of Water-Soluble Conductive Polymeric Nanowires. *Nano Lett.* **2007,** *7*, 3729-3733.

48. Chen, Z.; Li, N.; Li, S.; Dharmarwardana, M.; Schlimme, A.; Gassensmith, J. J. Viral chemistry: the chemical functionalization of viral architectures to create new technology. *Wiley Interdiscip. Rev. Nanomed. Nanobiotechnol.* **2016,** *8*, 512-534.

49. Furukawa, H.; Müller, U.; Yaghi, O. M. "Heterogeneity within Order" in Metal–Organic Frameworks. Angew. Chem. Int. Ed. **2015,** *54*, 3417-3430.

50. Ji, H.; Hwang, S.; Kim, K.; Kim, C.; Jeong, N. C. Direct in Situ Conversion of Metals into Metal–Organic Frameworks: A Strategy for the Rapid Growth of MOF Films on Metal Substrates. *ACS Appl. Mater. Interfaces.* **2016,** *8*, 32414-32420.

51. Li, G.; Sun, H.; Xu, H.; Guo, X.; Wu, D. Probing the Energetics of Molecule–Material Interactions at Interfaces and in Nanopores. *J. Phys. Chem. C.* **2017,** *121*, 26141-26154.

52. Chen, Z.; Li, N.; Chen, L.; Lee, J.; Gassensmith, J. J. Dual Functionalized Bacteriophage Qβ as a Photocaged Drug Carrier. *Small* **2016,** *12*, 4563-4571.

53. Chen, Z.; Boyd, S. D.; Calvo, J. S.; Murray, K. W.; Mejia, G. L.; Benjamin, C. E.; Welch, R. P.; Winkler, D. D.; Meloni, G.; D'Arcy, S.; Gassensmith, J. J. Fluorescent Functionalization across Quaternary Structure in a Virus-like Particle. *Bioconjugate Chem.* **2017,** *28*, 2277-2283.

54. Atabekov, J.; Nikitin, N.; Arkhipenko, M.; Chirkov, S.; Karpova, O. Thermal Transition of Native Tobacco Mosaic Virus and RNA-free Viral Proteins into Spherical Nanoparticles. *J. Gen. Virol.* **2011,** *92*, 453-456.

55. Mueller, A.; Eber, F. J.; Azucena, C.; Petershans, A.; Bittner, A. M.; Gliemann, H.; Jeske, H.; Wege, C. Inducible Site-Selective Bottom-Up Assembly of Virus-Derived Nanotube Arrays on RNA-Equipped Wafers. *ACS Nano* **2011,** *5*, 4512-4520.

56. Eber, F. J.; Eiben, S.; Jeske, H.; Wege, C. Bottom-Up-Assembled Nanostar Colloids of Gold Cores and Tubes Derived From Tobacco Mosaic Virus. *Angew. Chem. Int. Ed*. **2013,** *52*, 7203-7207.

57. Phases, in this context, means both crystalline and amorphous products produced in ZIF-8 synthesis.

58. Pan, Y.; Liu, Y.; Zeng, G.; Zhao, L.; Lai, Z. Rapid Synthesis of Zeolitic Imidazolate Framework-8 (ZIF-8) Nanocrystals in an Aqueous System. *Chem. Comm.* **2011,** *47*, 2071-2073.

59. Jian, M.; Liu, B.; Liu, R.; Qu, J.; Wang, H.; Zhang, X. Water-based Synthesis of Zeolitic Imidazolate Framework-8 with High Morphology Level at Room Temperature. *RSC Adv.* **2015,** *5*, 48433-48441.

60. Zhang, Y.; Zhu, F.; Zhang, J.; Xia, L. Converting Layered Zinc Acetate Nanobelts to One-dimensional Structured ZnO Nanoparticle Aggregates and their Photocatalytic Activity. *Nanoscale Res. Lett.* **2008,** *3*, 201-204.

61. Xiong, G.; Luo, H.; Zhang, J.; Jin, J.; Wan, Y. Synthesis of ZnO by Chemical Bath Deposition in the Presence of Bacterial Cellulose. *Acta Metall. Sin. Engl.* **2014,** *27*, 656-662.

62. Cravillon, J.; Schröder, C. A.; Nayuk, R.; Gummel, J.; Huber, K.; Wiebcke, M., Fast Nucleation and Growth of ZIF-8 Nanocrystals Monitored by Time-Resolved In Situ Small-Angle and Wide-Angle X-Ray Scattering. *Angew. Chem. Int. Ed*. **2011,** *50*, 8067-8071.

63. Terban, M. W.; Banerjee, D.; Ghose, S.; Medasani, B.; Shukla, A.; Legg, B. A.; Zhou, Y.; Zhu, Z.; Sushko, M. L.; De Yoreo, J. J.; Liu, J.; Thallapally, P. K.; Billinge, S. J. L., Early stage structural development of prototypical zeolitic imidazolate framework (ZIF) in solution. *Nanoscale* **2018**, *10*, 4291-4300.

64. Shi, Q.; Chen, Z.; Song, Z.; Li, J.; Dong, J. Synthesis of ZIF-8 and ZIF-67 by Steam-Assisted Conversion and an Investigation of Their Tribological Behaviors. *Angew. Chem. Int. Ed*. **2011,** *50*, 672-675.

65. Bruckman, M. A.; Steinmetz, N. F. In *Virus Hybrids as Nanomaterials: Methods and Protocols*, Lin, B.; Ratna, B., Eds.; Humana Press: Totowa, NJ, 2014; Chapter 13, pp 173-185.

66. Bruckman, M. A.; Randolph, L. N.; VanMeter, A.; Hern, S.; Shoffstall, A. J.; Taurog, R. E.; Steinmetz, N. F. Biodistribution, pharmacokinetics, and blood compatibility of native and PEGylated tobacco mosaic virus nano-rods and -spheres in mice. *Virology* **2014,** *449*, 163-173.

67. Veronese, F. M.; Mero, A. The Impact of PEGylation on Biological Therapies. *BioDrugs* **2008,** *22*, 315-329.

68. Steinmetz, N. F.; Manchester, M. PEGylated Viral Nanoparticles for Biomedicine: The Impact of PEG Chain Length on VNP Cell Interactions In Vitro and Ex Vivo. *Biomacromolecules* **2009,** *10*, 784-792.

69. Cravillon, J.; Nayuk, R.; Springer, S.; Feldhoff, A.; Huber, K.; Wiebcke, M. Controlling Zeolitic Imidazolate Framework Nano- and Microcrystal Formation: Insight into Crystal Growth by Time-Resolved In Situ Static Light Scattering. *Chem. Mater.* **2011,** *23*, 2130-2141.

70. Tang, N.; Skibsted, L. H. Zinc Bioavailability from Whey. Enthalpy-Entropy Compensation in Protein Binding. *Food Res. Int.* **2016,** *89*, 749-755.

CHAPTER 4

VALIDATE THE IMPACTS OF SYNTHETIC CONDITIONS ON MORPHOLOGY, CRYSTALLINITY AND VIABILITY OF BIOMIMETIC MINERALIZED MOFS ON LIVING CELLS

Authors - Zhuo Chen,[†] Shaobo Li,[†] Raymond P. Welch, Sampath Alahakoon, Ronald A. Smaldone, Jeremiah J. Gassensmith

The Department of Chemistry and Biochemistry, BE26

The University of Texas at Dallas

800 West Campbell Road

Richardson, Texas, 75080-3021

Reproduced from manuscript in preparation. Chen, Z.;[†] Li, S.[†] Welch, R. P.; Alahakoon, S.; Smaldone, R. A.; Gassensmith, J. J. Validate the Impacts of Synthetic Conditions on Morphology, Crystallinity and Viability of Biomimetic Mineralized MOFs on Living Cells. [†]These authors contributed equally to this manuscript.

4.1 Introduction

Chemical modifications on the cellular surface provides robust tools to engineer the stability, functionality and behavior in single cells. The hybridization of living cell and *in-situ* formed nanoparticles (NPs) or thin shells on the cellular surface was found to yield new functional mechanisms that are not observed in nature. For example, Yang *et al.*[1] invented a novel artificial photosynthetic device by growing photosensitized inorganic CdS NPs on the surface of CO_2-reducing bacterium, *Moorella thermoacetica*. The hybrid bacteria–CdS system showed a high quantum yield and nearly 90% production rate of acetic acid, demonstrating a high photosynthetic efficiency. Moreover, Qu *et al.*[2] reported a facile cell encapsulation strategy with nano-sized MnO_2 shell, which could protect the inlaid yeast cell from dehydration, lytic enzymes and cytotoxic reactive oxygen species (H_2O_2). In general, cell encapsulation is considered to be the most preferred way to equip both protection and function onto a single cell. In this case cell stability is improved by close confinement by rigid synthetic shell structures to minimize threats from external stresses, while gaps or defects in the shell allow transportation of nutrients to retain cell viability. Ideally, a protective and permeable shell structure with regulated pore size distribution is highly desired, as the mass transportation can be precisely managed by the available pore size of the shell. Metal organic frameworks (MOFs) are a family of porous coordination complexes that are constructed by rigid organic structs and metal cluster nodes. In addition to their inherited high surface area and well-defined porosity, the broad variety of composition, synthetic methods, and physicochemical properties made MOFs a promising functional material for storage, separation, catalysis and biomedical applications.[3-11] In recent years, a class of MOF-encapsulated biological specimens such as proteins, enzymes, viruses, and living cells, have been reported.[12-35] Significant

improvement of biological stability as well as mass transportation with restricted size regulation was highlighted in these studies. Liang *et al.*[24] for instance, first reported MOF-encapsulation on living cell and demonstrated protection against lysis enzymes, inhibition of cell division, recovery and proliferation after shell exfoliation. Later, they conducted MOF encapsulation after coating yeast cells with β-galactosidase, which provides exogenous metabolic pathway that can convert disaccharides into monosaccharides that can be metabolized by cells. Both studies have demonstrated that MOF-encapsulation could be a facile and smart way to protect and functionalize the cells. Unfortunately, these inspiring communications did not catch the deeper understanding in regard to the correlation between synthetic strategies, structure, viability and stability of as-obtained cell@MOF composites. Moreover, no direct evidence has shown whether the MOF shell is defect-free or not, whereas ideal size regulation of the permeable shell essentially relies on complete and non-deficient encapsulation.

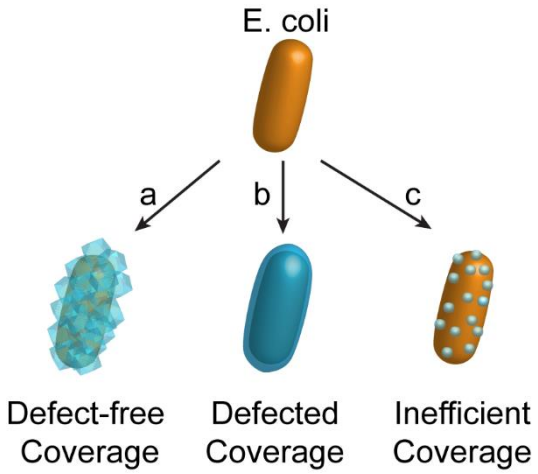

Scheme 4.1. Illustration of three types of *E. coli*@ZIF-8 that can be prepared via different synthetic strategies. Route "a" could yield a faceted thick ZIF-8 shell on *E. coli*. While by reducing the reaction time, precursor concentration, and L/M ratio of precursors a thin ZIF-8 shell (Route b) or even amorphous NPs (Route c) will be formed on the surface of *E. coli*.

Here, we use Escherichia coli (*E. coli*) as a model cellular template and zeolitic imidazolate framework-8 (ZIF-8) as MOF candidate to explore several feasible cell@MOF synthetic strategies and their impacts on consequent cell viability and composite stability (Scheme 1). We are able to show that an almost defect-free ZIF-8 encapsulation on *E. coli* could be accomplished, while cell integrity might be compromised owing to the concentrated precursor solutions used. Further, we show a step-by-step exploration of optimizing synthetic conditions to gain an effective ZIF-8 encapsulation strategy with improved retention of cell viability.

4.2 Results & Discussion

The bacterial cell wall is a natural template for growing inorganic nanomaterials and MOFs.[1, 36-38] Lipopolysaccharide,[39] the main component of gram negative bacteria outer layer, is considered to be responsible for efficiently inducing nucleation and crystal growth due to its negative charge and chelating phosphate groups. In addition to this reactive biological template, the crystallization precursors also play a vital role that directly determine the morphology and crystallinity of the resultant composites. We previously illustrated the impact of precursors upon formation of virus@MOF core-shell bionanoparticles (CSBNs) by using tobacco mosaic virus (TMV) as a biological template.[33] We discovered that CSBNs could be readily fabricated when precursors are prone to yield kinetic products, whereas cuboid crystal composites are formed if more ripened precursors, which can spontaneously form crystalline products, are employed. Encouraged by our previous mechanistic studies, we conducted cell@MOF encapsulation with *E. coli* as a cellular template, using zinc acetate and 2-methylimidazole (HMIM) aqueous solutions as metal and ligand precursors of MOF (ZIF-8). First, we were interested in recognizing the impact of ligand to metal molar ratio (L/M ratios), because it is a predominant factor that determine the formation of either

kinetic products or ripened crystals. In a typical preparation, 1 mg of *E. coli* was mixed with an aliquot of zinc precursor and the mixture was added to an aliquot of HMIM precursor followed by 20 seconds shaking and leaving on the benchtop overnight without further agitation. The L/M ratios were varied by changing the concentration of HMIM precursors, as we kept the volume of both precursors the same.

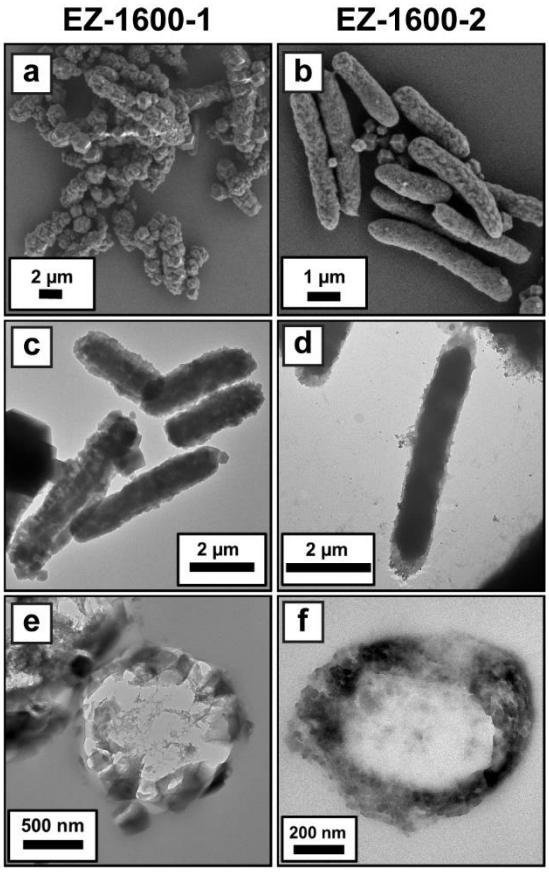

Figure 4.1. SEM micrographs of a) EZ-1600-1 and b) EZ-1600-2; TEM micrographs of c) EZ-1600-1, d) EZ-1600-2, and cross-sectioned view of e) EZ-1600-1 and f) EZ-1600-2.

To differentiate the products produced under varied preparation conditions, we denoted them as "EZ- HMIM concentration (in mM)- n (serial number if synthetic parameters except HMIM concentration are changed)" The product was collected by centrifugation at 9300 ×*g* and washed

twice with ultrapure water. The resultant *E. coli*@ZIF-8 composites (abbreviated as EZ) appeared as slightly yellowish white pellets and the color was dependent on the encapsulation efficiency (the thicker encapsulation, the whiter the pellet). The products were subjected to scanning electron microscopy (SEM) characterization to examine the encapsulation efficiency and morphology.

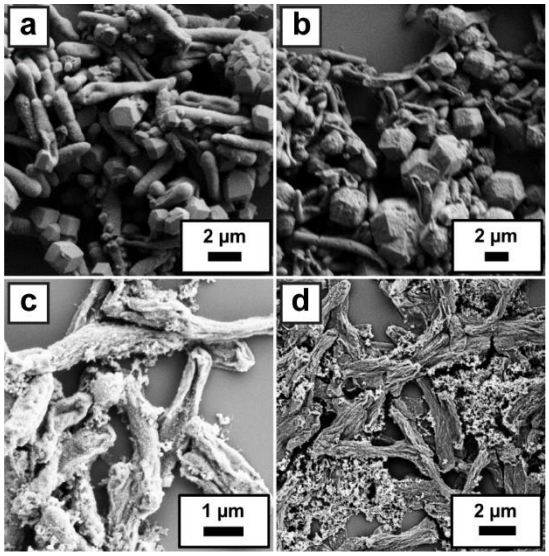

Figure 4.2. SEM micrographs of composites that were prepared with varied L/M ratio: a) 60:1 (EZ-1200); b) 40:1 (EZ-800); c) 20:1 (EZ-400-1).

To our surprise, SEM characterizations revealed that ZIF-8 encapsulation on *E. coli* favors high L/M ratio, which leads to more ripened crystallization conditions. This is contradictory to our finding in the case of TMV@ZIF-8 CSBNs. As illustrated in Figure 4.1 a, the L/M ratio of 80:1(EZ-1600-1) yields free standing micrometer-long rods with faceted surfaces. It is clear that the composites inherited the rod-like shape and length of the original bacterial template. Also, the faceted surfaces indicated a very crystalline shell was constructed on the bacteria. While as we gradually decreased L/M ratios to 60:1 and 40:1 (EZ-1200 and EZ-800), microrods with a smooth surface were obtained, with a large amount of free microcrystals coexisting in the products (Figure

4.2 a and b). Further lowering L/M ratios (20:1 and 10:1, EZ-400-2 and EZ-200) would lead to poor crystallization conditions that resulted in failed encapsulation, as all the composites were found to be flattened (Figure 4.2 c and d). This is due to the cellular structure collapsing as the bacteria with inefficient encapsulation of ZIF-8 cannot withstand high vacuum in the SEM chamber.

Due to the optimal shell growth efficiency, we employed L/M ratio of 80:1 to explore the encapsulation process of *E. coli*@ZIF-8. Figure 4.3 demonstrates an obvious morphological transformation at prolonged time points. A fast and efficient encapsulation could be obtained within just 30 min, as shown in Figure 4.3 a. The encapsulation shows a high level of coverage and strength so that the rod-shape of bacteria is well-preserved. Cuboid crystals formed at 1 h of reaction and continued growing untill the whole surface was covered (Figure 4.3 b – d). Thus, we are able to control the shell thickness by simply varying reaction time.

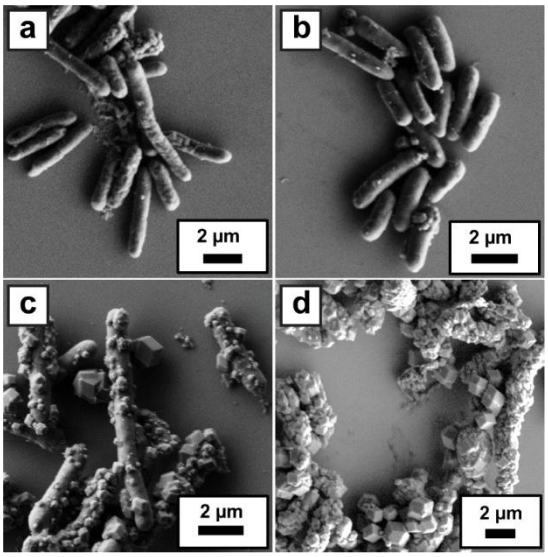

Figure 4.3. SEM micrographs of *E. coli*@ZIF-8 that prepared within different reaction time: a) 30 minutes; b) 1 hour; c) 2 hours and d) 16 hours.

We then chose composites that are synthesized with overnight and 30 minutes (EZ-1600-1 and EZ-1600-2) as representative *E. coli*@ZIF-8 prototypes. Transmission electron microscopy (TEM) confirmed that bacteria reside in the middle of ZIF-8 shell (Figure 4.1 c and d). The thick shell is about 200 ~ 300 nm thick whereas the thin shell is only 60 ~ 100 nm thick. Transvers cross-sectional views of both thick and thin ZIF-8 shells were obtained by ultramicrotomy and TEM (Figure 4.1 e and f). The thickness of thick and thin ZIF-8 rings are close to the measured thickness in core-shell characterizations. Energy Dispersive Spectroscopy (EDS) elemental mappings for both composites demonstrate homogeneous elemental distributions that superimpose to the rod-shaped composites in SEM images, indicating an integrated ZIF-8 coverage on bacteria.

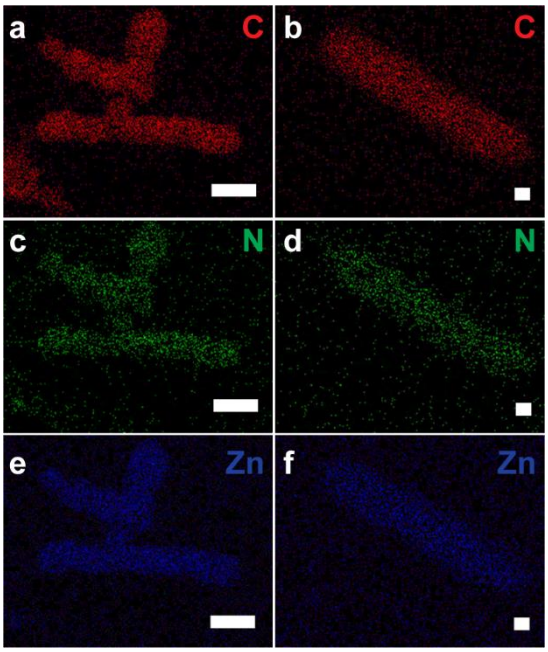

Figure 4.4. EDS mapping of carbon a) EZ-1600-1 and b) EZ-1600-2; nitrogen c) EZ-1600-1 and d) EZ-1600-2; and zinc e) EZ-1600-1 and f) EZ-1600-2.

Crystallinity and phase purity of the two prototypes was confirmed by powder X-ray diffraction (PXRD). All diffraction peaks aligned well with the simulated PXRD patterns of $Zn(MIM)_2$ with sod topology, indicating the shells in both cases are composed of pure ZIF-8 (Figure 4.5 a). Thermal stability of these composites was examined by thermogravimetric analysis (TGA) in air atmosphere (Figure 4.5 b). Comparing to pure ZIF-8, both of the composites gained a higher weight loss rate at 250–350 °C, reflecting the decomposition of biomolecular remnants of *E. coli*. A steep weight loss at about 450 °C appeared in all three samples, indicating the decomposition of ZIF-8. Surface area and porosity of the composites were investigated by N_2 sorption analysis at 77 K (Figure 4.5 c). Steep gas uptake at low relative pressure (< 0.03) was found in all the samples, revealing the presence of micropores (< 2 nm). Moreover, a H4 hysteresis loop appeared in both composites at relative pressure of 0.45 to 1.0. This is a typical indication of mesopores that causes capillary condensation of the adsorbate (N_2). BET surface area of pure ZIF-8 crystals, EZ-1600-1 and EZ-1600-2 were determined as 1842, 1655 and 1209 m^2/g. The gradually decreasing BET surface area correlates well with increasing content of low surface area bacterial template in the composites. Pore size distribution analysis (Figure 4.5 d) illustrates that both composites possess dominant micropores with a width of 10.8 Å, which is attributed to the intact ZIF-8 porous structure. However, short and broad peaks in mesopore (pore width in 2 – 50 nm) even macropore (> 50 nm) region were observed in both samples, especially in thin ZIF-8 shells (EZ-1600-2). Thus, we calculated the relative content of micro-, meso- and macropores in the composites, as shown in Table 4.1. For thick shell encapsulated EZ-1600-1, more than 98% of porosity is attributed to the intact ZIF-8 micropores, accompanied with 1.2% of mesopores and 0.3% of macropores, which account for surface defects and ZIF-8 encapsulation on broken bacteria.

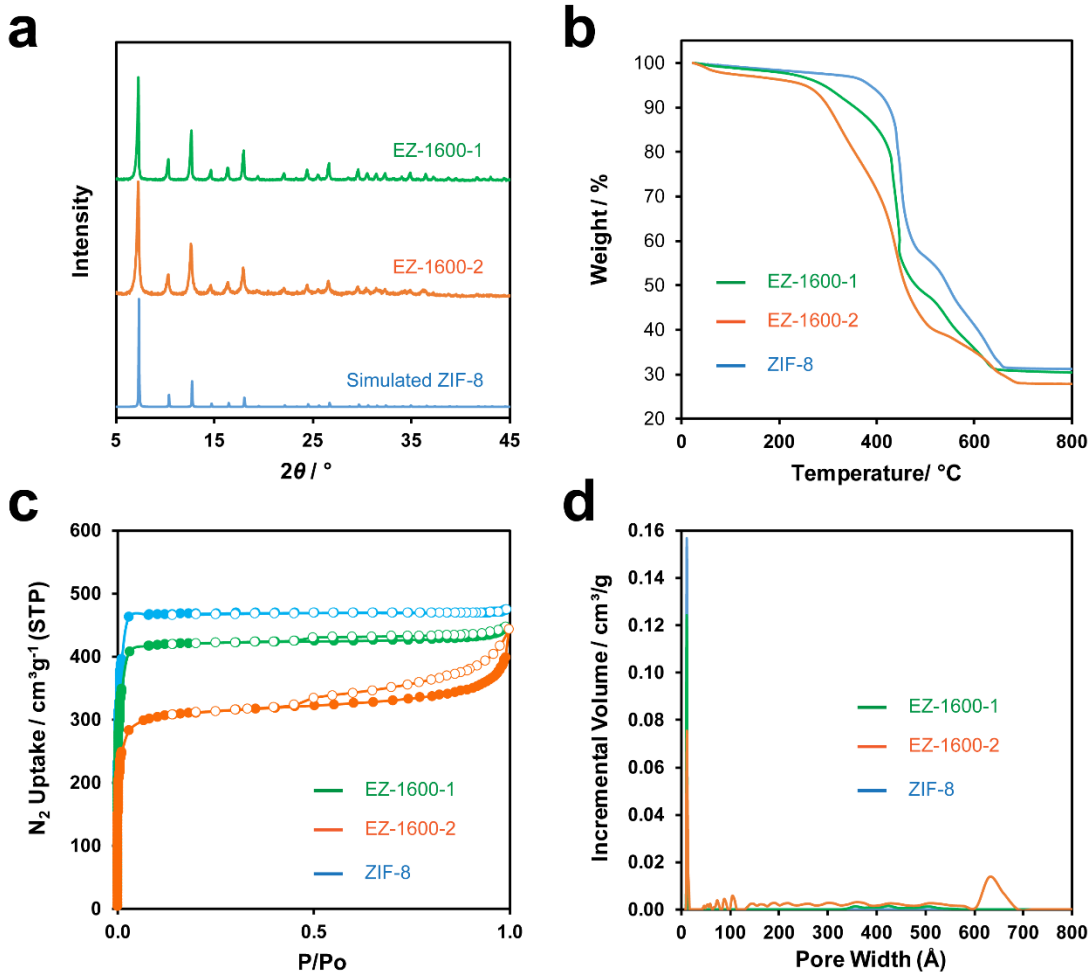

Figure 4.5. a) PXRD characterization of EZ-1600-1 and EZ-1600-2; b) TGA plot of ZIF-8, EZ-1600-1 and EZ-1600-2; c) N_2 adsorption-desorption isotherms of ZIF-8, EZ-1600-1 and EZ-1600-2; and d) pore size distribution plots that were accounted by incremental pore volume for ZIF-8, EZ-1600-1 and EZ-1600-2.

However, the composite with thinner ZIF-8 shell (EZ-1600-2) contains a much higher content of mesopores (> 17%) and macropores (>5%). This higher content of meso and macropores agrees with our initial assumption, as thin ZIF-8 shell is produced in a short period of reaction time that a perfect encapsulation is not permitted. Therefore, by controlling the reaction conditions, we can prepare nearly defect-free thick ZIF-8 shell and slightly defected thin ZIF-8 shell on the surface of

E. coli, while even the thin shell can be strong enough to retain integrity of the rod-shaped cell under high vacuum.

Table 4.1. Calculated percentage portions of each type of pores.

Type of Pore	Pore Volume%		
	ZIF-8	EZ-1600-1	EZ-1600-2
Mico	100.0	98.5	77.5
Meso	0.0	1.2	17.3
Macro	0.0	0.3	5.2
Total	100.0	100.0	100.0

To determine the viability of *E. coli* after ZIF-8 encapsulation, the composites were initially stained by fluorescein diacetate (FDA), which are hydrolyzed to green fluorescent compounds and retained in the living cells. However, we found ZIF-8 crystals could also produce green fluorescence with FDA (Figure 4.6 a).

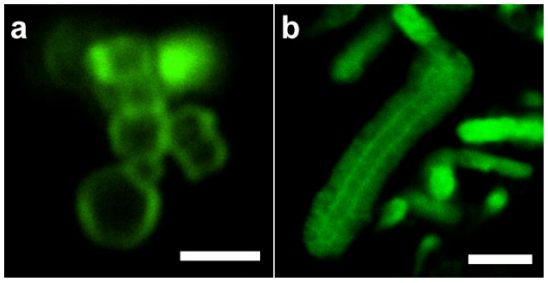

Figure 4.6. Green fluorescence images of FDA-stained a) ZIF-8 and b) EZ-1600-1 taken by confocal laser scanning microscope (CLSM).

We hypothesize that it was due to FDA being hydrolyzed on the surface of ZIF-8. A high magnification confocal microscopy image of EZ-1600-1 (Figure 4.6 b) also demonstrates that the entire surface of composites became fluorescent after FDA staining. Thus, we thought straight FDA staining on *E. coli*@ZIF-8 could result in misleading viability profiles.

To obtain reliable viability data, we decided to employ commercially available Live/Dead stain after exfoliation of ZIF-8 shells. The live/dead dyes stain differently on *E. coli* based on their

different abilities to penetrate the cell membrane. Cells with comprised membrane will be stained red, while the cell with intact membrane will show green under the microscope. Sodium acetate buffer (pH 5) was chosen for exfoliation due to it can efficiently dissolve ZIF-8 and does not show cytotoxicity to the living cells, comparing to a massive die-off caused by EDTA aqueous solution, which is another candidate for exfoliation (Figure 4.7 a – c).

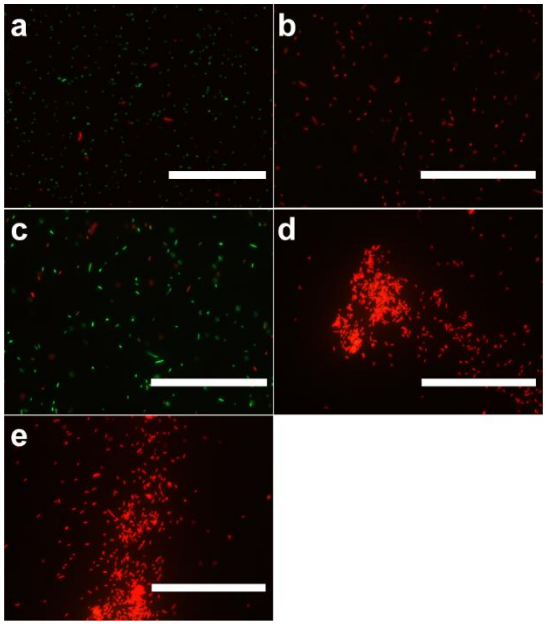

Figure 4.7. Merged green and red fluorescence images of a) native *E. coli*; b) *E. coli* after treated by 0.5 M EDTA Aq solution (pH 7); c) *E. coli* after treated by 1.0 M sodium acetate buffer (pH 5); d) EZ-1600-1 after exfoliated by sodium acetate buffer and e) EZ-1600-2 after exfoliated by sodium acetate buffer after stained by Live/Dead dyes.

The as-prepared composites were subjected to two cycles of exfoliation in sodium acetate buffer and two cycles of wash with ultrapure water, followed by Live/Dead stain. Unfortunately, both exfoliated composites showed strong red fluorescence under the microscope, indicating either massive death of bacteria or all the cell membranes were compromised (Figure 4.7 d and e).

In addition to Live/Dead staining, cell viability was also evaluated by monitoring cell division of exfoliated composites. The samples were incubated in fresh LB media supplemented with

ampicillin, followed by continuously shaking at 37 °C for 38 hours in a plate reader. OD_{600} were recorded with a 30-min interval. As shown in Figure 4.8a, both exfoliated composites recovered cell division and entered the log growth phase in about 4 h.

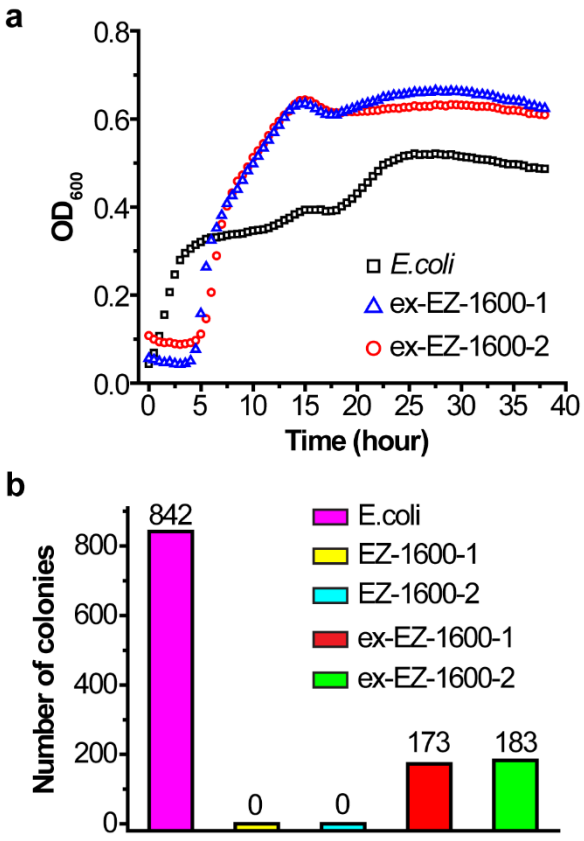

Figure 4.8. Cell viability evaluation based on a) bacteria growth measurement based on OD_{600} for native *E. coli*, exfoliated EZ-1600-1 and exfoliated EZ-1600-2; b) cell colony counting for native *E. coli*, EZ-1600-1, EZ-1600-2, exfoliated EZ-1600-1 and exfoliated EZ-1600-2.

In another experiment, intact composites, exfoliated composites, and native *E. coli* were separately plated on LB agar plates (supplemented with ampicillin). After incubation at 37 °C for 24 h, colonies on the plates were counted for each sample. As we expected, both exfoliated composites formed colonies on the LB agar plates while no colony was found in the plates that contain intact composites (Figure 4.8 b). This result indicates that proliferation of *E. coli* after exfoliation was

prohibited when encapsulated in rigid ZIF-8 shell, but could be recovered if shells were properly removed. Based on the seemingly contradictory viability results that were determined by Live/Dead stain or cell division tests, we hypothesized that our encapsulation methods may cause cell membrane damage, while cell contents remain well preserved such that the exfoliated bacteria are capable of performing cell division.

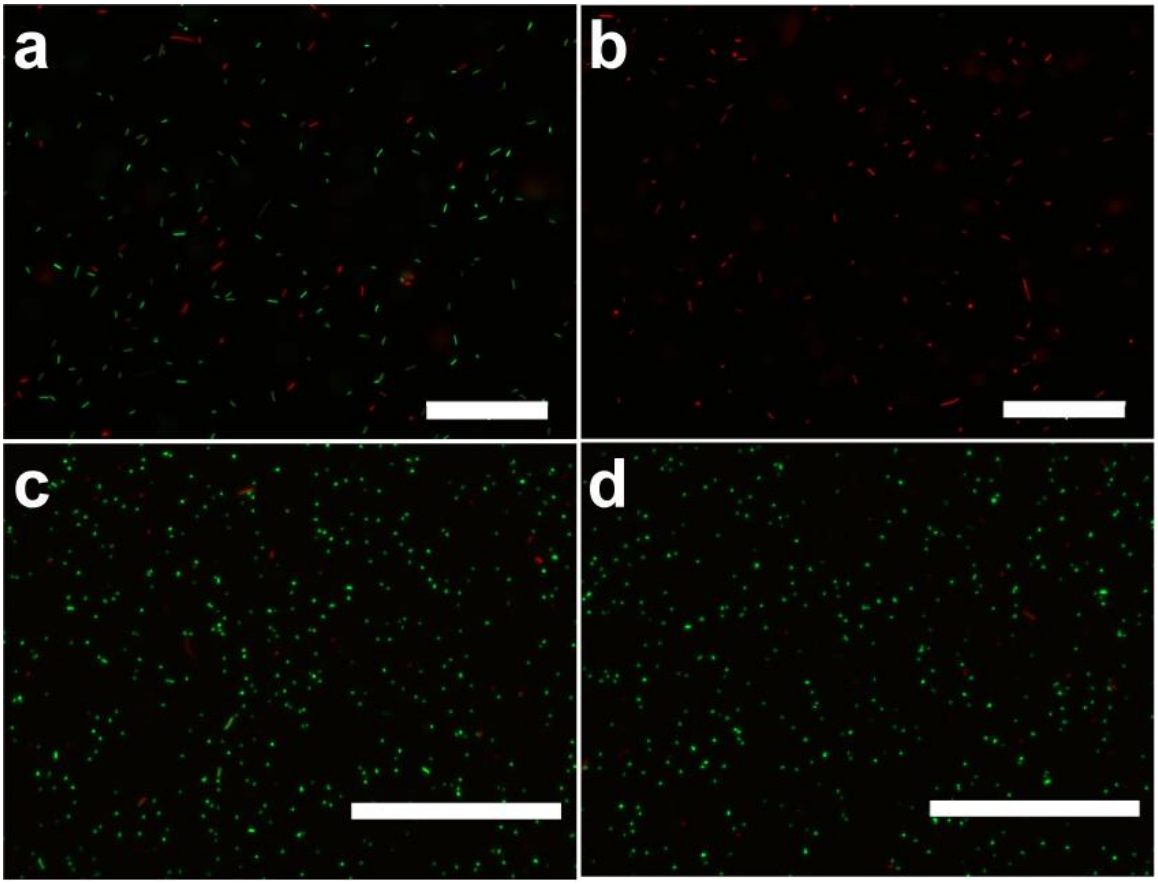

Figure 4.9. Merged green and red fluorescence images of a) *E. coli* after incubated with 20 mM zinc acetate Aq solution; b) *E. coli* after incubated with 1600 mM HMIM Aq solution; c) *E. coli* after incubated with 400 mM HMIM Aq solution; and d) *E. coli* after incubated with 160 mM HMIM Aq solution.

To find out the root cause of cell membrane damage, bacteria were incubated in zinc acetate (20 mM) and HMIM precursors (1600 mM) in separate vials for 30 min, followed by two wash cycles with ultrapure water and Live/Dead stain. The results revealed that zinc precursor drew negligible impact whereas HMIM precursor should be responsible for the cell membrane damage due to strong red fluorescence in HMIM-treated cells (Figure 4.9 a and b). We were thus urged to find appropriate HMIM concentration that would not lead to significant damage to cell membranes. HMIM concentrations of 400 mM and 160 mM were tested with *E. coli* followed by Live/Dead stain, as illustrated in Figure 4.9c and d. Bacteria showed strong green fluorescence in both cases. Preliminary optimized syntheses were conducted in the same fashion as previously described, except using lower HMIM concentration and shorter reaction times, denoted as EZ-400-2 and EZ-160-1. SEM characterization revealed that EZ-400-2 contains a incomplete encapsulation owing to a large amount of cavities that could be observed on the surfaces, and the composite appeared somehow flattened (Figure 4.10a). In the case of EZ-160-1 (Figure 4.10b), the products turned out to be even more flattened and aggregated, indicating very poor encapsulation. It is anticipated because the L/M ratio of EZ-160-1 precursors was only 4:1, which could hardly facilitate nucleation and crystallization of ZIF-8, even with presence of bacteria. PXRD results (Figure 4.11) confirmed EZ-400-2 contains poorly crystalline ZIF-8, whereas EZ-160-1 only contains an amorphous phase. Both composites were subjected to exfoliation and Live/Dead stain test to reveal cell viability. As illustrated in Figure 4.12, exfoliated EZ-400-2 showed all red fluorescence whereas EZ-160-1 contained nearly 1:1 red and green fluorescence. We suspected that 400 mM of HMIM could still be relatively harsh comparing to 160 mM. Thus, we targeted to optimize syntheses by using 160 mM HMIM precursor and relatively higher L/M ratios.

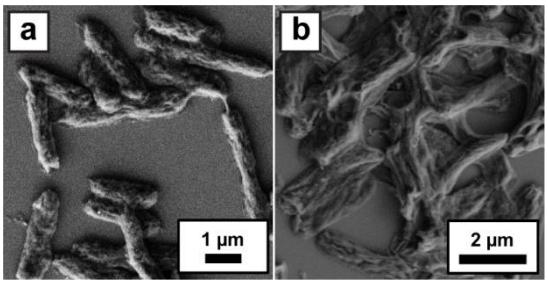

Figure 4.10. SEM micrographs of a) EZ-400-2 and b) EZ-160-1.

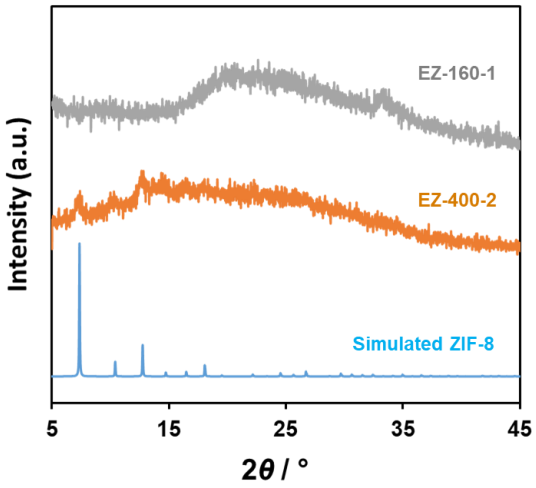

Figure 4.11. PXRD of EZ-400-2 and EZ-160-1.

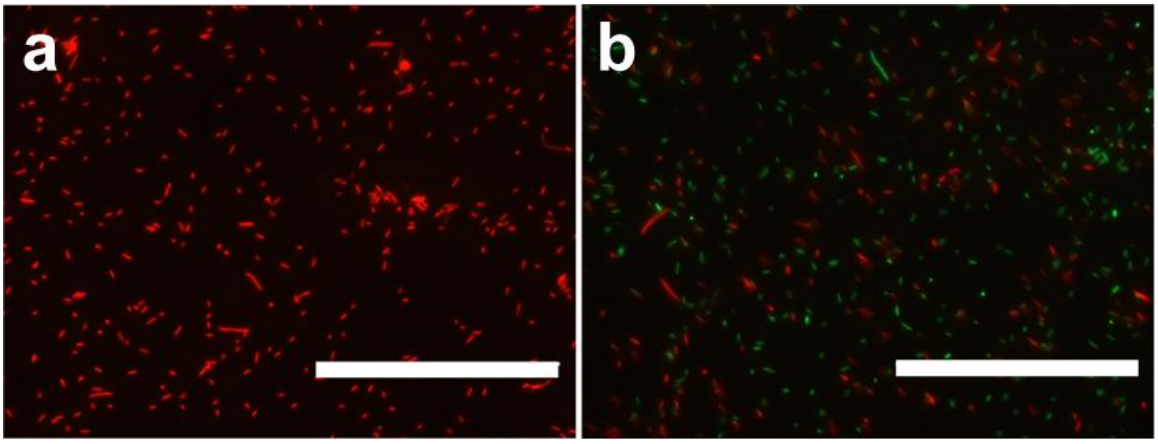

Figure 4.12. Merged green and red fluorescence images of a) exfoliated EZ-400-2 and b) exfoliated EZ-160-1.

Table 4.2. Synthetic parameters of modified EZ-160 series.

Sample #	E. coli	Zn(Oac)2 Aq			HMIM Aq			Reaction Time	L/M	Zn/E. coli	MIM/E. coli	Final C_{MIM}	Final $C_{E. coli}$
	mg	mM	µL	mmol	mM	µL	mmol		mmol/mmol	mmol/mg	mmol/mg	mM	mg/ml
EZ-160-2	1	20	500	0.01	160	500	0.08	30 min	8:1	0.01	0.08	80	0.98
EZ-160-3	1	20	500	0.01	160	1500	0.24	30 min	24:1	0.01	0.24	120	0.49
EZ-160-4	1	20	500	0.01	160	2500	0.40	30 min	40:1	0.01	0.40	133	0.33
EZ-160-5	1	10	1000	0.01	160	2000	0.32	30 min	32:1	0.01	0.32	107	0.33
EZ-160-6	1	5	2000	0.01	160	2000	0.32	30 min	32:1	0.01	0.32	80	0.25

Detailed synthetic conditions and parameters are listed in Table 4.2. The mass of bacteria and molar quantity of zinc precursor were fixed in order to reduce the number of variables. Higher L/M ratios were achieved by increasing the volume of HMIM precursors in the syntheses. Surprisingly, we were able to observe the improved encapsulation by simply increasing L/M ratio from 8:1 to 40:1 (EZ-160-2 to EZ-160-4, Table 4.2 and Figure 4.13 a – c). Besides the increased L/M ratios, we also realized that the final concentration of bacteria dropped significantly, from 0.98 to 0.33 mg/ml. We thought the decreased bacteria concentration would lead to lower surface density in the reaction system, allowing more efficient crystallization. This is consistent with our previous finding in making thick ZIF-8 shell on TMV.[22] Liang *et al*. also demonstrated poor MOF crystallization caused by increasing protein concentration.[15] Moreover, synthesis with lower zinc concentration and relatively higher L/M ratio (32:1), denoted as EZ-160-5 (Table 4.2), also yielded a smooth ZIF-8 shell (Figure 4.13 d). Live/Dead stain was performed for the well-encapsulated cells (EZ-160-3 to 5), as demonstrated in Figure 4.14. Green fluorescence could be captured in all three samples, which were never seen in previous well encapsulated composites (EZ-1600-1 and 2). We also noticed that the number of green fluorescent cells in EZ-160-5 slightly higher than EZ-160-3 and 4. We thought that it benefited from lower final HMIM concentration, which made it less toxic to the cells.

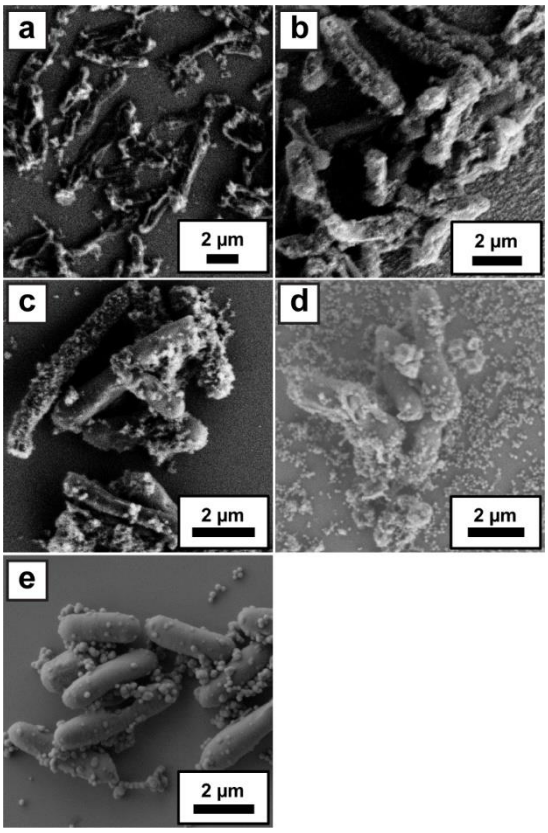

Figure 4.13. SEM micrographs of a) EZ-160-2; b) EZ-160-3; c) EZ-160-4; d) EZ-160-5 and e) EZ-160-6.

Finally, we further decreased the zinc concentration to 5 mM while keep L/M ratio to 32:1 (EZ-160-6, Table 4.2). In this case HMIM concentration of 160 mM and a L/M ratio of 32:1 are retained, while the final HMIM concentration is lowered to only 80 mM. The conditions produced a well-encapsulated morphology. Viability tests including Live/Dead stain, growth curve and colony counting will be performed to investigate the cell integrity and cell proliferation capability. Based on our learning and optimizations we are confident that this optimal synthesis could cause minimum cell damage that we can ever achieve.

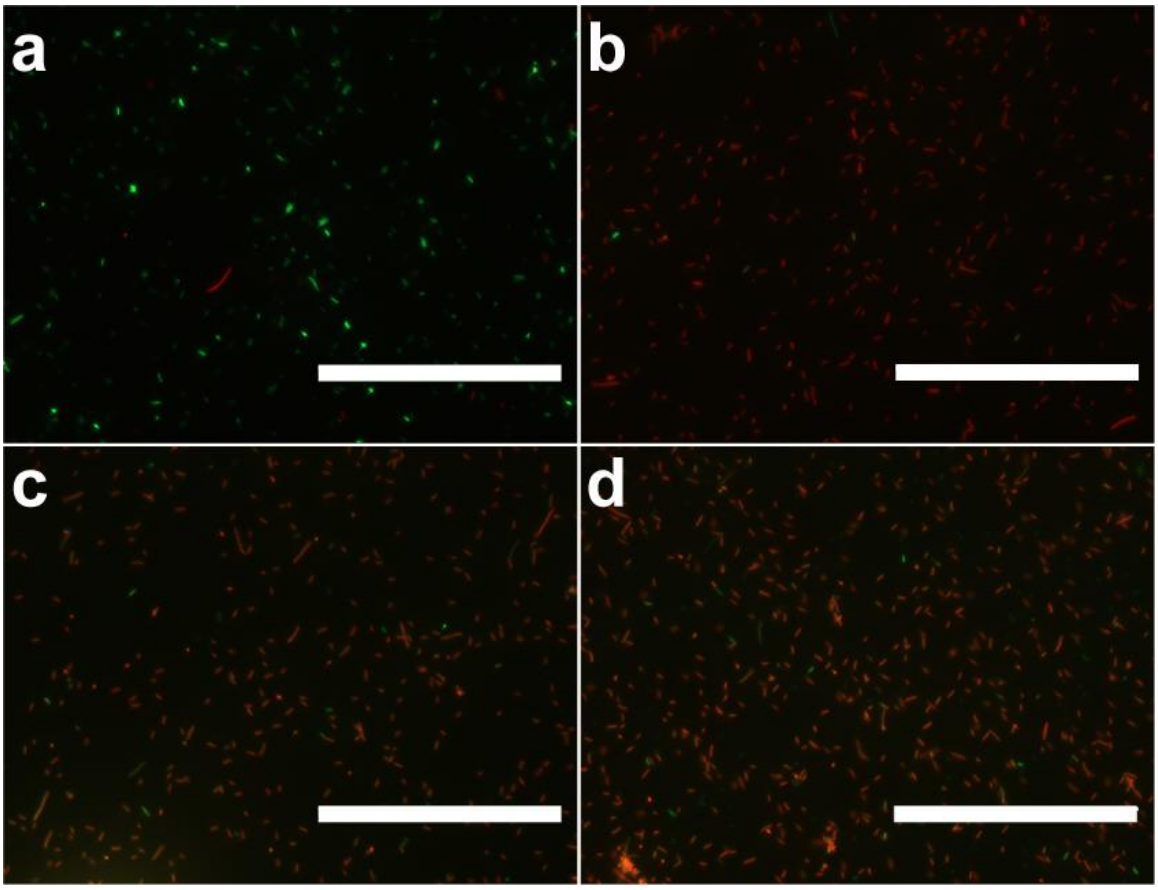

Figure 4.14. Merged green and red fluorescence images of a) native *E. coli*; b) exfoliated EZ-160-3; c) exfoliated EZ-160-4 and d) exfoliated EZ-160-5.

4.3 Conclusion

We explored various cell@MOF encapsulation strategies that could yield different type of morphologies and thicknesses. Nearly defect-free ZIF-8 shell could be constructed on the bacteria when we employed concentrated HMIM precursor and long period of reaction time. The impact of synthetic conditions on cell viability was also systemetically studied. We were able to unveil key parameters, such as L/M ratio, reaction time, HMIM concentration, and *E. coli* concentration after mixing, could essentially determine the morphology, crystallinity and cell viability of the

composites. Our study provides valuable guidance to biomimetic MOF mineralization on living cells.

4.4 References

1. Sakimoto, K. K.; Wong, A. B.; Yang, P. Self-photosensitization of nonphotosynthetic bacteria for solar-to-chemical production. *Science* **2016,** *351*, 74.

2. Li, W.; Liu, Z.; Liu, C.; Guan, Y.; Ren, J.; Qu, X. Manganese Dioxide Nanozymes as Responsive Cytoprotective Shells for Individual Living Cell Encapsulation. *Angew. Chem., Int. Ed.* **2017,** *56*, 13661-13665.

3. Karagiaridi, O.; Lalonde, M. B.; Bury, W.; Sarjeant, A. A.; Farha, O. K.; Hupp, J. T. Opening ZIF-8: A Catalytically Active Zeolitic Imidazolate Framework of Sodalite Topology with Unsubstituted Linkers. *J. Am. Chem. Soc.* **2012,** *134*, 18790-18796.

4. Gándara, F.; Furukawa, H.; Lee, S.; Yaghi, O. M. High Methane Storage Capacity in Aluminum Metal–Organic Frameworks. *J. Am. Chem. Soc.* **2014,** *136*, 5271-5274.

5. He, C.; Lu, K.; Lin, W. Nanoscale Metal–Organic Frameworks for Real-Time Intracellular pH Sensing in Live Cells. *J. Am. Chem. Soc.* **2014,** *136*, 12253-12256.

6. Kornienko, N.; Zhao, Y.; Kley, C. S.; Zhu, C.; Kim, D.; Lin, S.; Chang, C. J.; Yaghi, O. M.; Yang, P. Metal–Organic Frameworks for Electrocatalytic Reduction of Carbon Dioxide. *J. Am. Chem. Soc.* **2015,** *137*, 14129-14135.

7. Marshall, R. J.; Griffin, S. L.; Wilson, C.; Forgan, R. S. Single-Crystal to Single-Crystal Mechanical Contraction of Metal–Organic Frameworks through Stereoselective Postsynthetic Bromination. *J. Am. Chem. Soc.* **2015,** *137*, 9527-9530.

8. Mondloch, J. E.; Katz, M. J.; Isley Iii, W. C.; Ghosh, P.; Liao, P.; Bury, W.; Wagner, G. W.; Hall, M. G.; DeCoste, J. B.; Peterson, G. W.; Snurr, R. Q.; Cramer, C. J.; Hupp, J. T.; Farha, O. K. Destruction of chemical warfare agents using metal–organic frameworks. *Nat. Mater.* **2015,** *14*, 512.

9. Orellana-Tavra, C.; Marshall, R. J.; Baxter, E. F.; Lazaro, I. A.; Tao, A.; Cheetham, A. K.; Forgan, R. S.; Fairen-Jimenez, D. Drug delivery and controlled release from biocompatible metal-organic frameworks using mechanical amorphization. *J. Mater. Chem. B* **2016,** *4*, 7697-7707.

10. Abánades Lázaro, I.; Haddad, S.; Sacca, S.; Orellana-Tavra, C.; Fairen-Jimenez, D.; Forgan, R. S. Selective Surface PEGylation of UiO-66 Nanoparticles for Enhanced Stability, Cell Uptake, and pH-Responsive Drug Delivery. *Chem* **2017,** *2*, 561-578.

11. Lim, J.; Lee, E. J.; Choi, J. S.; Jeong, N. C. Diffusion Control in the in Situ Synthesis of Iconic Metal–Organic Frameworks within an Ionic Polymer Matrix. *ACS Appl. Mater. Interfaces* **2018,** *10*, 3793-3800.

12. Lykourinou, V.; Chen, Y.; Wang, X.-S.; Meng, L.; Hoang, T.; Ming, L.-J.; Musselman, R. L.; Ma, S. Immobilization of MP-11 into a Mesoporous Metal–Organic Framework, MP-11@mesoMOF: A New Platform for Enzymatic Catalysis. *J. Am. Chem. Soc.* **2011,** *133*, 10382-10385.

13. Lyu, F.; Zhang, Y.; Zare, R. N.; Ge, J.; Liu, Z. One-Pot Synthesis of Protein-Embedded Metal–Organic Frameworks with Enhanced Biological Activities. *Nano Lett.* **2014,** *14*, 5761-5765.

14. Chulkaivalsucharit, P.; Wu, X.; Ge, J. Synthesis of enzyme-embedded metal-organic framework nanocrystals in reverse micelles. *RSC Adv.* **2015,** *5*, 101293-101296.

15. Liang, K.; Ricco, R.; Doherty, C. M.; Styles, M. J.; Bell, S.; Kirby, N.; Mudie, S.; Haylock, D.; Hill, A. J.; Doonan, C. J.; Falcaro, P. Biomimetic mineralization of metal-organic frameworks as protective coatings for biomacromolecules. *Nat. Commun.* **2015,** *6*, 7240.

16. Shieh, F.-K.; Wang, S.-C.; Yen, C.-I.; Wu, C.-C.; Dutta, S.; Chou, L.-Y.; Morabito, J. V.; Hu, P.; Hsu, M.-H.; Wu, K. C. W.; Tsung, C.-K. Imparting Functionality to Biocatalysts via Embedding Enzymes into Nanoporous Materials by a de Novo Approach: Size-Selective Sheltering of Catalase in Metal–Organic Framework Microcrystals. *J. Am. Chem. Soc.* **2015,** *137*, 4276-4279.

17. Wu, X.; Ge, J.; Yang, C.; Hou, M.; Liu, Z. Facile synthesis of multiple enzyme-containing metal-organic frameworks in a biomolecule-friendly environment. *Chem. Commun.* **2015,** *51*, 13408-13411.

18. Wu, X.; Hou, M.; Ge, J. Metal-organic frameworks and inorganic nanoflowers: a type of emerging inorganic crystal nanocarrier for enzyme immobilization. *Catal. Sci. Technol.* **2015,** *5*, 5077-5085.

19. Wu, X.; Yang, C.; Ge, J.; Liu, Z. Polydopamine tethered enzyme/metal-organic framework composites with high stability and reusability. *Nanoscale* **2015,** *7*, 18883-18886.

20. Li, P.; Modica, Justin A.; Howarth, Ashlee J.; Vargas L, E.; Moghadam, Peyman Z.; Snurr, Randall Q.; Mrksich, M.; Hupp, Joseph T.; Farha, Omar K. Toward Design Rules for Enzyme Immobilization in Hierarchical Mesoporous Metal-Organic Frameworks. *Chem* **2016,** *1*, 154-169.

21. Li, P.; Moon, S.-Y.; Guelta, M. A.; Harvey, S. P.; Hupp, J. T.; Farha, O. K. Encapsulation of a Nerve Agent Detoxifying Enzyme by a Mesoporous Zirconium Metal–Organic

Framework Engenders Thermal and Long-Term Stability. *J. Am. Chem. Soc.* **2016,** *138*, 8052-8055.

22. Li, S.; Dharmarwardana, M.; Welch, R. P.; Ren, Y.; Thompson, C. M.; Smaldone, R. A.; Gassensmith, J. J. Template-Directed Synthesis of Porous and Protective Core–Shell Bionanoparticles. *Angew. Chem., Int.Ed.* **2016** , *55*, 10691 –10696.

23. Liang, K.; Coghlan, C. J.; Bell, S. G.; Doonan, C.; Falcaro, P. Enzyme encapsulation in zeolitic imidazolate frameworks: a comparison between controlled co-precipitation and biomimetic mineralisation. *Chem. Commun.* **2016,** *52*, 473-476.

24. Liang, K.; Richardson, J. J.; Cui, J.; Caruso, F.; Doonan, C. J.; Falcaro, P. Metal–Organic Framework Coatings as Cytoprotective Exoskeletons for Living Cells. *Adv. Mater.* **2016,** *28*, 7910-7914.

25. Cui, J.; Feng, Y.; Lin, T.; Tan, Z.; Zhong, C.; Jia, S. Mesoporous Metal–Organic Framework with Well-Defined Cruciate Flower-Like Morphology for Enzyme Immobilization. *ACS Appl. Mater. Interfaces* **2017,** *9*, 10587-10594.

26. Doonan, C.; Riccò, R.; Liang, K.; Bradshaw, D.; Falcaro, P. Metal–Organic Frameworks at the Biointerface: Synthetic Strategies and Applications. *Acc. Chem. Res.* **2017,** *50*, 1423-1432.

27. Hou, M.; Zhao, H.; Feng, Y.; Ge, J. Synthesis of patterned enzyme–metal–organic framework composites by ink-jet printing. *Bioresour Bioprocess.* **2017,** *4*, 40.

28. Lian, X.; Fang, Y.; Joseph, E.; Wang, Q.; Li, J.; Banerjee, S.; Lollar, C.; Wang, X.; Zhou, H.-C. Enzyme-MOF (metal-organic framework) composites. *Chem. Soc. Rev.* **2017,** *46*, 3386-3401.

29. Liang, K.; Richardson, J. J.; Doonan, C. J.; Mulet, X.; Ju, Y.; Cui, J.; Caruso, F.; Falcaro, P. An Enzyme-Coated Metal–Organic Framework Shell for Synthetically Adaptive Cell Survival. *Angew. Chem., Int. Ed.* **2017,** *56*, 8510-8515.

30. Majewski, M. B.; Howarth, A. J.; Li, P.; Wasielewski, M. R.; Hupp, J. T.; Farha, O. K. Enzyme encapsulation in metal-organic frameworks for applications in catalysis. *CrystEngComm* **2017,** *19*, 4082-4091.

31. Wu, X.; Yang, C.; Ge, J. Green synthesis of enzyme/metal-organic framework composites with high stability in protein denaturing solvents. *Bioresour Bioprocess.* **2017,** *4*, 24.

32. Zhang, C.; Wang, X.; Hou, M.; Li, X.; Wu, X.; Ge, J. Immobilization on Metal–Organic Framework Engenders High Sensitivity for Enzymatic Electrochemical Detection. *ACS Appl. Mater. Interfaces* **2017,** *9*, 13831-13836.

33. Li, S.; Dharmarwardana, M.; Welch, R. P.; Benjamin, C. E.; Shamir, A. M.; Nielsen, S. O.; Gassensmith, J. J. Investigation of Controlled Growth of Metal–Organic Frameworks on Anisotropic Virus Particles. *ACS Appl. Mater. Interfaces* **2018,** *10*, 18161-18169.

34. Liang, W.; Ricco, R.; Maddigan, N. K.; Dickinson, R. P.; Xu, H.; Li, Q.; Sumby, C. J.; Bell, S. G.; Falcaro, P.; Doonan, C. J. Control of Structure Topology and Spatial Distribution of Biomacromolecules in Protein@ZIF-8 Biocomposites. *Chem. Mater.* **2018,** *30*, 1069-1077.

35. Riccò, R.; Liang, W.; Li, S.; Gassensmith, J. J.; Caruso, F.; Doonan, C.; Falcaro, P. Metal–Organic Frameworks for Cell and Virus Biology: A Perspective. *ACS Nano* **2018,** *12*, 13-23.

36. Li, W.; Zhang, Y.; Xu, Z.; Meng, Q.; Fan, Z.; Ye, S.; Zhang, G. Assembly of MOF Microcapsules with Size-Selective Permeability on Cell Walls. *Angew. Chem., Int. Ed.* **2015,** *55*, 955-959.

37. Nair, B.; Pradeep, T. Coalescence of Nanoclusters and Formation of Submicron Crystallites Assisted by Lactobacillus Strains. *Cryst. Growth Des.* **2002,** *2*, 293-298.

38. Du, L.; Jiang, H.; Liu, X.; Wang, E. Biosynthesis of gold nanoparticles assisted by Escherichia coli DH5α and its application on direct electrochemistry of hemoglobin. *Electrochem. Commun.* **2007,** *9*, 1165-1170.

39. Liang, K.; Wang, R.; Boutter, M.; Doherty, C. M.; Mulet, X.; Richardson, J. J. Biomimetic mineralization of metal-organic frameworks around polysaccharides. *Chem. Commun.* **2017,** *53*, 1249-1252.

CHAPTER 5

SUMMARY & PERSPECTIVES

5.1 Summary

This dissertation has demonstrated feasible biomimetic mineralization strategies of MOFs on viral and bacterial substrates. The studies on prototypical TMV@ZIF-8 and *E. coli*@ZIF-8 composites generally focus on synthesizing thin ZIF-8 shells rather than bulky microcrystals that have been shown by other research groups. In addition, the integrity, robustness and permeability of the as-formed ZIF-8 shells have been examined.

Through Chapter 2 to Chapter 4, a few well-examined design-rules of preparing biology@MOF composites can be summarized as follows: i) concentration of precursors not only dictate morphology and crystallinity, but also influence cell viability, which is vital for cell encapsulation; ii) L/M ratios play the most important role under all scenarios that have been shown in this dissertation, to the success of ZIF-8 encapsulation on virus and bacteria; iii) reaction time has more impacts on synthetic conditions that use concentrated HMIM precursors, which result in faceted shells or even cuboid crystals. All these key factors will determine the efficiency of MOF encapsulation, the stability of as-formed core-shell composites, and even the cell viability, if living cells are employed.

5.2 Perspectives

The biomimetic mineralization of MOFs is still an emerging field. To date, only ZIF-8 has been proved to be the most promising candidate due to it can be readily prepared in aqueous system and possesses robust stability. New type of MOFs or novel synthetic strategies should be developed to

overcome the poor water solubility and minimize potential toxicity of the precursors. In addition, the mechanisms of MOF formation on proteinaceous surface are still not clear. Considering the complexity of biological specimens, one should not expect a universal rule that can be applied to all scenarios. I am confident that more core-shell MOF bio-nanocomposites will be prepared and studied in the pursuit of protection and functionalization on biological substrates. Hence, more biological specimens and MOF candidates will be precisely investigated, categorized and reviewed to enrich our understanding of this field.

The potential of core-shell MOF bio-nanocomposites is mostly based on stability and permeability of MOF shell. These unique characteristics might be more promising for *in vitro* applications, such as enzyme immobilization and biomass production. The MOF shell formation could essentially improve the versatility and complexity of bio-catalysis and biomass production. For example, tandem catalysts could be prepared by layer-by-layer MOF growth with multiple types of enzymes to be enclosed in different layers. The order and quantity of enzymes in each layer could be precisely controlled by synthetic strategies. An effective MOF encapsulation on living cells will bring longevity and protection against external stresses and infection, which can significantly reduce the cost in microbial industry.

BIOGRAPHICAL SKETCH

Shaobo was born in Beijing, China. He received his bachelor's degree in Applied Chemistry at Beijing University of Technology in 2011. Later he joined Procter & Gamble Technology (Beijing) Co., Ltd. as a researcher and started his career in the detergent industry. He went to UT Dallas in 2013 to pursue a PhD degree in chemistry under the supervision of Dr. Jeremiah Gassensmith.

CURRICULUM VITAE

Shaobo Li

Education

PhD in Chemistry, University of Texas at Dallas, Richardson, TX, USA — Anticipated 08/2018

BE in Applied Chemistry, Beijing University of Technology, Beijing, China — 07/2011

Research & Professional Experience

Department of Chemistry & Biochemistry, UT Dallas — 01/2014 – present

Advisor: Prof. Jeremiah J. Gassensmith — Graduate Research Assistant

- Established biomimetic mineralization of metal organic frameworks (MOFs) on virus, bacteria and micro-animal. Pioneered in fabrication and morphological control of MOF-encapsulated biological composite materials. Investigated growth mechanism of virus@MOF core-shell bionanoparticles.
- Conducted comprehensive material characterizations including but not limited to SEM, EDS, TEM, PXRD and TGA to investigate stability and permeability of core-shell-structured composite materials.
- Contributed 2 peer-reviewed journal articles and 1 review article in regard to the emerging MOF biomimetic mineralization field.
- Collaborated with electrochemist to explore the potential of pyrolyzed biological MOF composites as electrode material of electrochemical capacitor (supercapacitor).
- Mentored undergrad researchers for experimental design, data analysis and interpretation.
- Established tobacco plant farming and reapplied infection and isolation of tobacco mosaic virus (TMV) to propagate TMV for laboratory research.

Procter & Gamble Technology (Beijing) Co., Ltd, Beijing, China — 07/2011 – 05/2013

Strategic& Innovation Technology, Fabric Care — Researcher

- Employed instrumental characterization and mimic hand-wash tests to screen various surfactant and polymeric additives for optimal rinsing technology aimed on hand-wash dominated markets.
- Collaborated with scientists in North America technology sites to set up new experimental technique for anti-redeposition performance evaluation. Self-motivated to optimize test method to fit in local capabilities and improve test efficiency.
- Developed easy-to-rinse liquid detergent prototypes agilely to assist product research and marketing teams for urgent consumer tests.
- Involved partnership with New Hires and help them adapt to research communities and facilities.

Skills

- Proficiency in Scanning Electron Microscopy (SEM) and Transmission Electron Microscopy (TEM), including Energy-dispersive X-ray spectroscopy (EDS)
- Proficiency in Power X-ray Diffraction (PXRD) for crystalline nanomaterials/composites
- Proficiency in Thermogravimetric Analysis (TGA) for composite materials

- Experience in spectroscopy: UV-vis, Fluorescence and Raman
- Proficiency in Microsoft Word, Excel, PowerPoint
- Experience in Adobe Illustrator, Google SketchUp and UCSF Chimera

Publications

Peer-Reviewed Publications

1. **S. Li**, M. Dharmarwardana, R. P. Welch, C. E. Benjamin, A. M. Shamir, S. O. Nielsen, J. J. Gassensmith. "Investigation of Controlled Metal Organic Frameworks on Anisotropic Virus Particles." *ACS Appl. Mater. Interfaces*, **2018**, ASAP. DOI: 10.1021/acsami.8b01369 *Selected to be on the Cover *Selected as ACS Editors' Choice
2. R. Riccò, W. Liang, **S. Li**, J. J. Gassensmith, F. Caruso, C. Doonan, P. Falcaro. "Metal-Organic Frameworks for Cell and Virus Biology: A Perspective" *ACS Nano*, **2018**, *1*, 13–23. DOI: 10.1021/acsnano.7b08056
3. **S. Li**, M. Dharmarwardana, R. P. Welch, Y. Ren, C. M. Thompson, R. A. Smaldone, J. J. Gassensmith. "Template-Directed Synthesis of Porous and Protective Core–Shell Bionanoparticles." *Angew. Chem. Int. Ed.* **2016**, *55*, 10691–10696. DOI: 10.1002/anie.201604879
4. Z. Chen, N. Li, **S. Li**, M. Dharmarwardana, A. Schlimme, J. J. Gassensmith. "Viral Chemistry: The Chemical Functionalization of Viral Architectures to Create New Technology." *WIREs Nanomed. Nanobiotechnol.* **2016**, *8*, 512–534. DOI: 10.1002/wnan.1379 *Featured on Wiley's online *Chemistry Views* "Chemistry Goes Viral".

Peer-Reviewed Book Chapters

1. **S. Li** and J. J. Gassensmith: "Synthesis of Metal-Organic Frameworks on Tobacco Mosaic Virus Templates" Ed: Andrew K. Udit. *Methods in Molecular Biology.* New York: Springer. In Press **2018**.

Appearances in Scientific Media

1. Publication highlighted in the online *Atlas of Science*: "Virus chainmail: protective and porous metal-organic framework grown on a virus," *atlastofscience.com* **2017**.

Presentations

1. **S. Li**, M. Dharmarwardana, R. P. Welch, Y. Ren, C. M. Thompson, R. A. Smaldone, C. E. Benjamin, A. M. Shamir, S. O. Nielsen and J. J. Gassensmith. Contributed lecture on "Biomimetic Mineralization of ZIF-8 Templated by Anisotropic Virus Particles." ACS DFW Section 51st Annual Meeting-in-Miniature, Dallas, TX, USA. April 21, **2018**.
2. **S. Li**, M. Dharmarwardana, R. Welch, J. J. Gassensmith. Contributed lecture on "Synthesis and Characterization of Metal-Organic Frameworks Coated Virus Particle." ACS National Meeting, San Diego, CA, USA. March 13, **2016**.
3. **S. Li**, R. P. Welch, J. J. Gassensmith. Contributed Lecture "Construction of Heteroporous Polymer-MOF Hybrid Material." Texas Soft Matter Meeting, Rice University, Houston, TX, USA. August 21, **2015**.

Honors

PhD travel grant, University of Texas at Dallas 03/2016

Undergraduate Scholarship (top 8% students), Beijing University of Technology 10/2009